5-2018

INVESTIGATIONS OF NOVEL SOURCES OF SPIN-POLARIZED ELECTRONS

Evan Brunkow
University of Nebraska - Lincoln, ebrunkow@huskers.unl.edu

Brunkow, Evan, "INVESTIGATIONS OF NOVEL SOURCES OF SPIN-POLARIZED ELECTRONS" (2018). *Theses, Dissertations, and Student Research: Department of Physics and Astronomy*. 43.
http://digitalcommons.unl.edu/physicsdiss/43

INVESTIGATIONS OF NOVEL SOURCES OF SPIN-POLARIZED ELECTRONS

by

Evan Michael Brunkow

A DISSERTATION

Presented to the Faculty of

The Graduate College at the University of Nebraska

In Partial Fulfillment of Requirements

For the Degree of Doctor of Philosophy

Major: Physics and Astronomy

Under the Supervision of Professor Timothy J. Gay

Lincoln, Nebraska

May, 2018

INVESTIGATIONS OF NOVEL SOURCES OF SPIN-POLARIZED ELECTRONS

Evan Michael Brunkow, Ph.D.

University of Nebraska, 2018

Advisor: Timothy J. Gay

Using a pulsed laser, we investigated the spin-polarization of electrons emitted from bulk GaAs, Ti and Pd chiral nanostructures, and electro-chemically thinned GaAs. Standard sources of spin-polarized electrons from GaAs can have polarizations of approximately 30%, while state-of-the-art spin-polarized electron sources using GaAs cathodes can have as high as 85% spin polarization. Drawbacks for these sources are that they require constant upkeep, have strict vacuum requirements, and are very difficult to learn how to use. For these reasons, we investigated new methods through a different emission process and different materials to see if we could measure a spin-polarization from these electron sources.

For the bulk GaAs, we found that the amount of emission that is obtained for a laser pulse decreases due to an electron population in the conduction band state caused by an earlier laser pulse. We refer to this as subadditivity and developed a model that would describe the emission of the electrons and showed us that the emission of the electrons is fast, i.e. comparable to the duration of a

laser pulse. After measuring the spin-polarization of the electrons from bulk GaAs, we found that it is spin-polarized, so this may be the first fast, spin-polarized source of electrons with a polarization of approximately 13%.

Measurements of the other materials yielded no spin-polarization but brought up further questions that may be investigated in the future.

Photoemitted electrons from a chiral surface reconstruction of Si were also investigated to find out if there is a polarization of emitted electrons using the APE beamline at the Elettra Sincrotrone facility.

Dedication

This dissertation would not have been possible without the loving support of my beautiful wife, Julie, and my amazing son, Evan Michael Brunkow Jr, without either of whom, I wouldn’t have been able to do this.

Acknowledgements

I would like to thank my advisor, Prof. Tim Gay, for his help guiding me through my graduate career. Whether it was aiding with difficulties in my experiment or giving advice on potential future employment opportunities, he always had some useful advice. I must also express my appreciation to my committee members: Profs. Stephen Ducharme, Anthony Starace, Dennis Alexander and Herman Batelaan. This is especially true for Herman Batelaan as his group often worked closely with our group and genuinely wanted to help further my research since they were interested in the results of my research.

I must thank all the members of the machine shop and electronic shop for all the help they gave me over the years from building a new piece of equipment for me to fixing a power supply that I blew up. In particular, Les Marquart, Bob Rhynalds, Mike Thompson, Brian Farleigh, and Bob Kelty.

I would also like to thank all current and past members of the Gay group as well as in other groups that we have worked with closely. In particular, I would like to thank Nathan Clayburn, Keith Foreman, Karl Ahrendsen, Joan Dreiling, and Josh Beck; all of whom have been great sources of help, good conversations, and camaraderie.

Finally, I must give the biggest thanks to my wife for her constant support and encouragement. She has made all the highs and lows associated with graduate school seem better. I couldn’t have made it through without her while keeping my sanity. She gave me the best sources of motivation anyone could ask: her love and support and my beautiful son, Evan Jr. Anytime I doubted myself, I knew that I could count on my wife and son to help me through it.

Table of Contents

List of Figures

List of Tables

Chapter 1. Introduction

This dissertation describes investigations of potential novel sources of spin-polarized electrons. Other projects include the development of a Mott polarimeter as well as studies of emission from a chiral surface reconstruction of Si caused by a synchrotron light source. Three different materials were investigated to determine if they could produce a viable source of spin-polarized electrons that is at least comparable in terms of current and/or polarization to currently-used sources. The first material is bulk GaAs wafers that have been cut to have a sharp tip. The second is chiral nanostructures of Ti or Pd grown on a Si substrate. The third is also GaAs, that, through electro-chemical etching, has been thinned at the end. Motivation for this research will be explained, followed by the work of this dissertation with a discussion involving the apparatus, various properties of the samples, results of the experiments, and a comparison between these sources and current ones.

1.1 Polarization

One can always define a quantization axis for any given electron so that it has “spin-up” or “spin-down” along that axis. In a collection of unpolarized electrons, their spin directions are randomly oriented such that the number of spin-up electrons along any specific axis is equal to the number of spin-down electrons. If, however, there exists an axis for all the electrons such that there is an imbalance in the number of spin-up versus spin-down electrons, that collection of electrons is said to be polarized. The definition of polarization, P, along that axis is

$$P = \frac{N_{\uparrow} - N_{\downarrow}}{N_{\uparrow} + N_{\downarrow}}, \tag{1.1}$$

where $N_{\uparrow,\downarrow}$ is the number of electrons that are spin-up or –down respectively (1).

The reason for using spin-polarized electrons in an experiment is to check to see if there are any spin-dependent effects involved. If the electrons are unpolarized, any effects that happen due to the spin of the electron are averaged out of the results. In electron-atom scattering, for example, by measuring the polarization of both an incident and scattered electron beam, it becomes possible to determine if the incident electron exchanged with one of the electrons bound to the target or not. (This requires that a light target be used so that there is no spin flipping during the collision (2)). Without analysis of the polarization, it would be impossible to determine whether the incident or the target electron is the one that was scattered.

1.2 Sources of Spin-Polarized Electrons

Spin-polarized electrons have been used in a wide variety of disciplines, including atomic and molecular physics (1) (3), high energy nuclear physics (4) (5), and solid state physics (6) (7) (8). Current state-of-the-art spin-polarized electron sources use gallium arsenide (GaAs) photoemitters. For this reason, GaAs has been studied extensively to attempt to maximize the polarization of the emitted electrons. Many papers have been published that describe how to obtain spin-polarized electrons from GaAs (9) (10). The reason for using GaAs is that when you use circularly-polarized light of a given helicity with a near-band-gap energy (1.42 eV), the excitation probability for the $m_j = \pm 1/2$ states in the $^2s_{1/2}$ band (as seen in Fig. 1.1) is different. This leads to more electrons being in the $m_j = + 1/2$ state or the $m_j = - 1/2$ state depending on which helicity of circularly-polarized light is used. As can be seen from Fig. 1.1, for each handedness of the incident light, the transition from the $m_j = \pm 3/2$ in the $^2p_{3/2}$ band to the $m_j = \pm 1/2$ in the $^2s_{1/2}$ band is three times as likely as the transition from the $m_j = \pm 1/2$ in the $^2p_{3/2}$ band to the $m_j = \mp 1/2$ state in the $^2s_{1/2}$ band. For a given incident light helicity, this allows for an imbalance in the populations of the two different m_j states in the conduction band that corresponds to a theoretical maximum of 50% polarization (eqn. 1.1). Typically, for bulk GaAs, the polarization of the emitted electrons is 25%-30% due to various depolarizing processes involved in the electrons leaving the crystal. These spin-flip processes involve collisions with other atoms as they make their way from the bulk to the surface or by scattering from the surface (9). Another view of the band structure of GaAs is shown in Fig. 1.2a. In addition to its band-gap energy, GaAs also has an electron affinity (the amount of energy

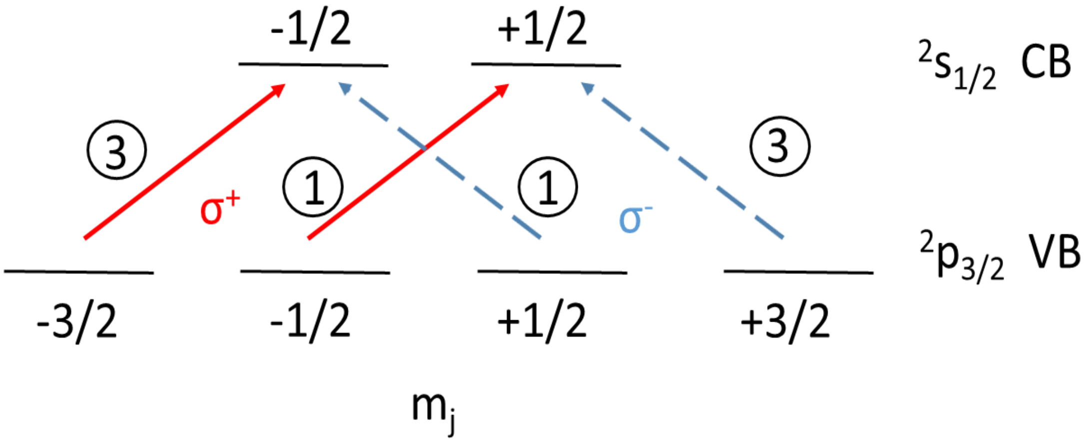

Figure 1.1. Energy-level diagram for GaAs at its Γ point. When either right- or left-handed circularly-polarized light (σ^+ or σ^- respectively) is used to illuminate the crystal, there is an imbalance in the excitation probabilities from the valence band (VB) to the conduction band (CB). If the opposite-handed light is used, the opposite polarization state has the higher probability of excitation. The values of the total angular momentum magnetic quantum number, m_j, are shown for their respective states. The numbers in circles represent the relative probability of electrons being excited from that state for the given polarization. Figure is adapted from ref. (9).

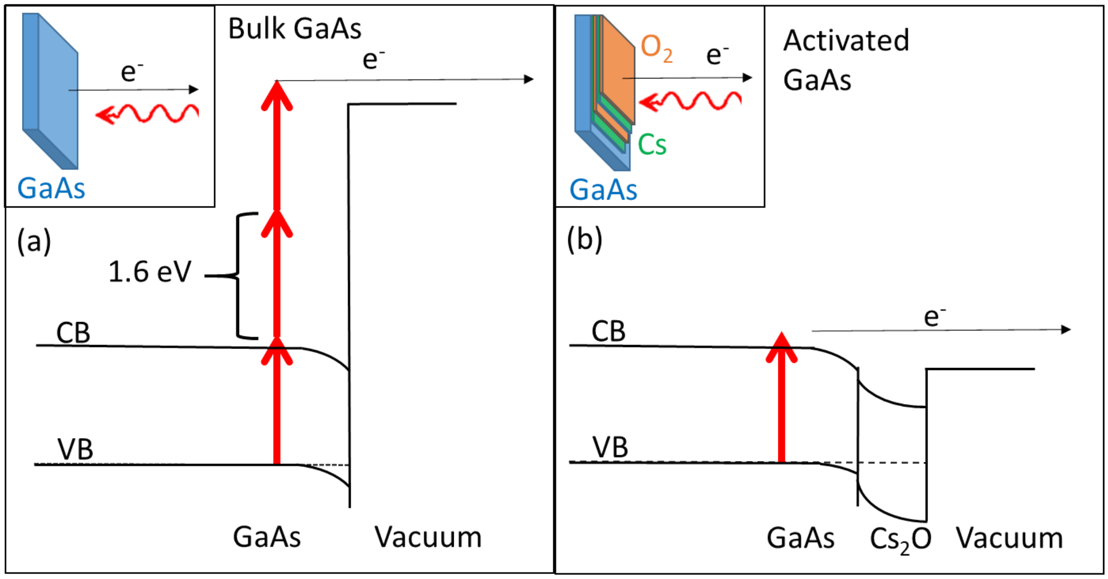

Figure 1.2. Simplified diagram of GaAs energy-level structure for (a) bulk GaAs and (b) negative electron affinity (NEA) surfaces. The band bending of both the valance band (VB) and conduction band (CB) at the surface of the GaAs is due to the usual p-dopant used for photoemission. (b) The vacuum energy is lowered due to the Cs and O_2 being deposited on the surface with a simple picture of the layering (inset) of Cs (green) and O_2 (orange) on the GaAs (blue). Single photon emission is also shown. Figure adapted from ref. (9).

needed to move an electron from the conduction band to the vacuum) of 4.07 eV.

When the electrons are excited by a laser with energy close to the bandgap energy, they are polarized in the excited state. Unfortunately, the electrons are still bound in the material since they don't have enough energy to surmount the materials' electron affinity. For this reason, a process described below is carried out to give the GaAs negative electron affinity (NEA). This allows the electrons that are excited to the conduction band to escape the material. A simplified view of what it means to have NEA can be seen in Fig. 1.2b. Once an NEA surface is present, an electron only needs to absorb a single photon to escape the crystal. Even though essentially all photons are absorbed, typical quantum efficiencies are < 1% (9) due to electrons being recaptured by the crystal before they can be emitted from the surface.

The process of creating an NEA surface is complicated and has many requirements to be successful. The entire process of preparing the crystal is called "activation". The most important factor is the pressure in the chamber. In order for this procedure to work, the vacuum pressure must be in the low 10^{-10} Torr range or below. These pressures are required because the crystal needs to remain atomically clean in order to maintain an NEA condition. In order to achieve these low pressures, baking the chamber to $>150^{0}$ C for several days is required. Every time the chamber is opened, as can happen often when one is learning to activate a photocathode, a new bake is required to return to the pressure needed. The baking/activation procedure can take weeks to carry out.

Once a sufficiently low base pressure is reached, the crystal itself needs to be heat cleaned. There are different ways to do this. One way is to resistively heat the crystal by passing a current through it and slowly increase the current until the GaAs wafer glows red-orange. Another is to heat the support on which the GaAs is mounted until the crystal heats up and glows the same red-orange. Whichever way is chosen, the crystal needs to be heated until it has a uniform red-orange color. This is a very crucial step because if the crystal is not heated up enough, it isn't clean enough to yield an NEA surface. If the temperature gets too high, the crystal will become frosted and is ruined. Frosting is caused by non-stoichiometric evaporation of gallium and arsenic from the crystal, which causes gallium droplets to form on the surface (10) (11) (12). This frosting results in a large decrease in quantum efficiency, effectively making the photocathode unusable (10). If this happens, a new photocathode will need to be put in the source and the entire process restarted. An attempt to quantify the color needed was done by other members of our group using a camera to determine the color of the crystal and from that, calculate the temperature of the crystal *in situ* (13). This is a good step towards making it easier to learn to use this type of source.

Once the crystal is properly heat cleaned, alternating layers of cesium and oxygen (10) or NF_3 (14) must be applied to create an NEA GaAs surface (Fig. 1.2b).

The NEA state is not permanent for a crystal. Even in ultra-high vacuum, contaminants depositing on the surface and bombardment from back streaming ions produced by collisions of photoelectrons with residual gas molecules will cause the NEA state to be degraded (15). If the activation is lost, the crystal will have to be heat cleaned again and new cesium and oxygen will need to be applied. Depending on the experimental setup and the partial pressures of various surface contaminants, a functional source can last anywhere from a few hours to days or even months depending on the rate of contamination. This limits the types of targets that are able to be used in an experiment. The amount and the type of contamination varies due to differences in vacuum systems and even in photocathode preparation, so even in the same system, different photocathodes will require slightly different procedures. Since only a general procedure can be established, obtaining a source in a new system can take many months to get a successful activation, and even a new photocathode can take several activation attempts (13).

This high level of difficulty and the long amount of time needed to learn the operation of conventional GaAs sources led us to investigate other possible sources of polarized electrons that didn’t have as many drawbacks and would potentially enable users to get closer to a turn-key system. An attempt to eliminate the NEA and pressure requirements of the current sources made us decide to investigate sources that would utilize a pulsed laser that could allow us to obtain emission from the samples by absorbing multiple photons from a single pulse (as seen in Fig. 1.2a), thereby eliminating the need of NEA altogether. This, in turn, would allow us to avoid strict vacuum pressure requirements. A further explanation of how multiphoton emission works will be given in Chapter 3.

1.3 Target Samples

The three samples mentioned earlier each were chosen as targets for different reasons. The first sample was bulk GaAs because we thought that it had a high likelihood of success given its band structure (Fig. 1.1). Multi-photon emission using a pulsed Ti: Sapphire oscillator at ~800 nm would allow us to utilize the excitation probabilities described earlier, subsequently enabling the electrons to absorb additional photons in order to emit them without lowering the vacuum level. It has been shown that for NEA sources, the polarization decreases dramatically as the photon energy increases much beyond the energy of the band gap (9). So, we must use multiphoton emission if we have any hopes of retaining the polarization properties of the excited state. The low requirements of sample preparation would be ideal for reducing the difficulty of starting a new source.

The second type of sample involved Ti and Pd chiral nanostructures. These are corkscrew-like structures that are grown on a Si substrate. These samples were chosen because we wanted to investigate if the chirality of the structures could cause a preferential spin of emitted electrons.

The last type of sample was also GaAs, but thinned through an electro-chemical process by the Flanders group located at Kansas State University. The reason for choosing these was that sharp tips, called field emission tips (FETs), can cause larger electron emission than bulk materials (16) (17), so we wanted to investigate if this thinning would enhance the emitted electron current.

Chapter 2. Experimental Apparatus

All the experiments discussed in the chapters to follow were completed with the same experimental setup unless otherwise noted. As seen in Fig. 2.1, the apparatus is comprised of two connected chambers. Both chambers are made of non-magnetic 304 stainless steel purchased from the Kurt J. Lesker Company. The first chamber contains the sample for emitting the electrons as well as optics to focus the laser and electrostatic optics to guide the emitted electrons toward the second chamber, which holds a Mott polarimeter.

2.1. Lasers and Optics

The entire assembly of lasers and optics can be seen in Fig. 2.2. The laser system (Fig. 2.2 and Fig. 2.3) we used was a Ti: Sapphire femtosecond pulse laser oscillator (18) that was pumped using a CW laser (19) that outputs a 532 nm beam of up to 12 W. The pump laser passes through a half-wave plate and a polarizing beam-splitting cube in order to allow the power to the Ti: Sapphire laser to be varied. This power variation was only used when alignment of the internal mechanics of the pulsed laser was needed and was otherwise left providing 10 W of power to the pulsed laser. It then passes through another half-wave plate to allow us to send the proper linear polarization into the pulsed laser. Two mirrors are then used to align the pump beam direction before it enters the pulsed laser

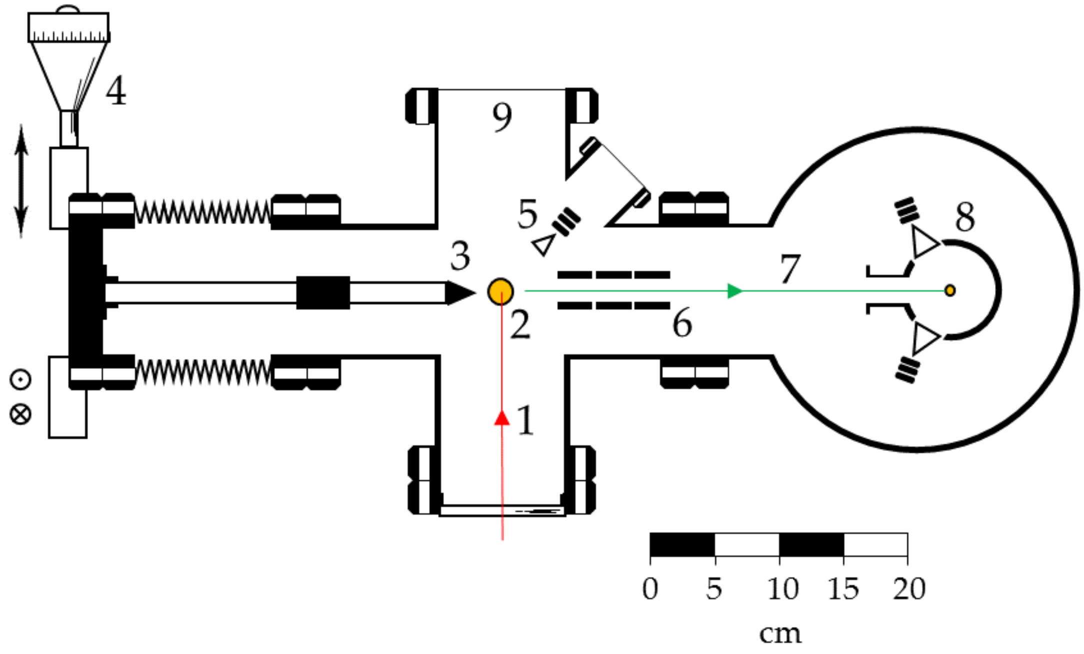

Figure 2.1. Schematic of the experimental setup. The fs pulsed laser (1) goes into the chamber and hits the focusing mirror (2) which focuses the beam onto the sample (3). The sample is mounted on an XYZ translator (4) to allow us to focus the laser at the desired location. A channel electron multiplier (CEM) (5) nearby can be used to detect total electron emission rates. Transport optics consisting of electrostatic lenses (6) are located on the major axis of the chamber to focus any emitted electrons (7) toward the Mott polarimeter (8), located in the adjoining chamber. A turbomolecular pump (9) is mounted to the side of the chamber to provide base pressures of 10^{-7} Torr.

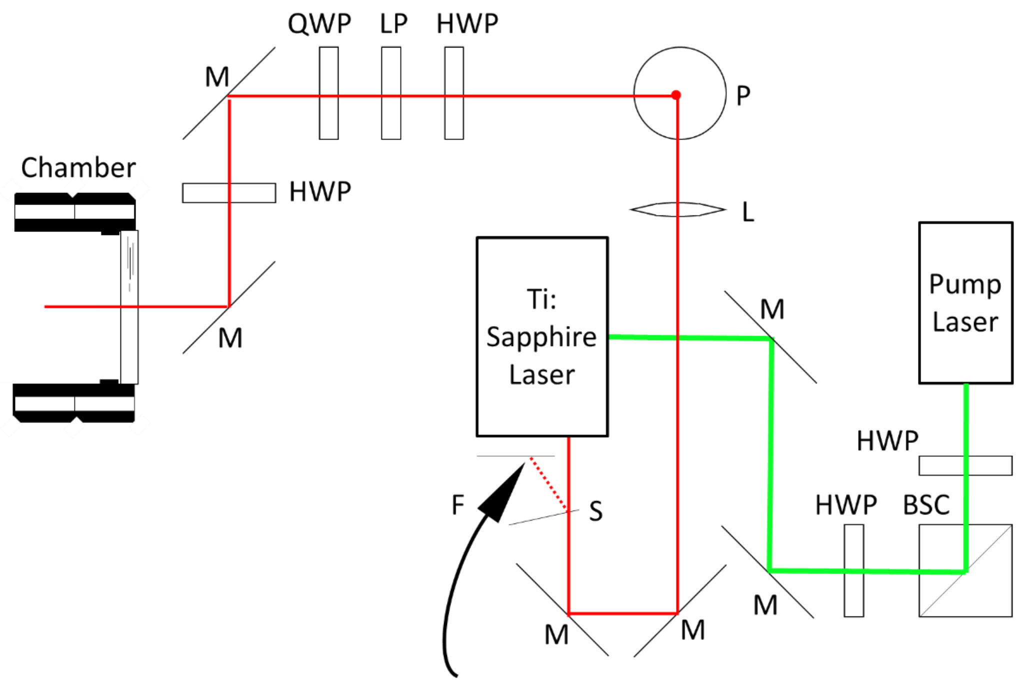

Figure 2.2 Laser and optics schematic. A 532 nm pump laser passes through half-wave plates (HWP) and a beam-splitting cube (BSC) to enable adjustments of the power and linear polarization. Mirrors (M) allow for proper alignment into the Ti: Sapphire laser oscillator. At the output of the Ti: Sapphire laser, a microscope slide (S) reflects ~10% of the beam to a piece of paper where the spectrometer analyzes the beam via a fiber (F) placed near the output. After reflecting from more mirrors and through a collimating lens (L), the beam goes through a periscope assembly (P) that adjusts the height of the beam. After P, the beam passes through more HWPs, a linear polarizer (LP) and a quarter-wave plate (QWP) to allow us to obtain either direction of circularly-polarized light or any direction of linear polarization before entering the target chamber (Fig 2.1).

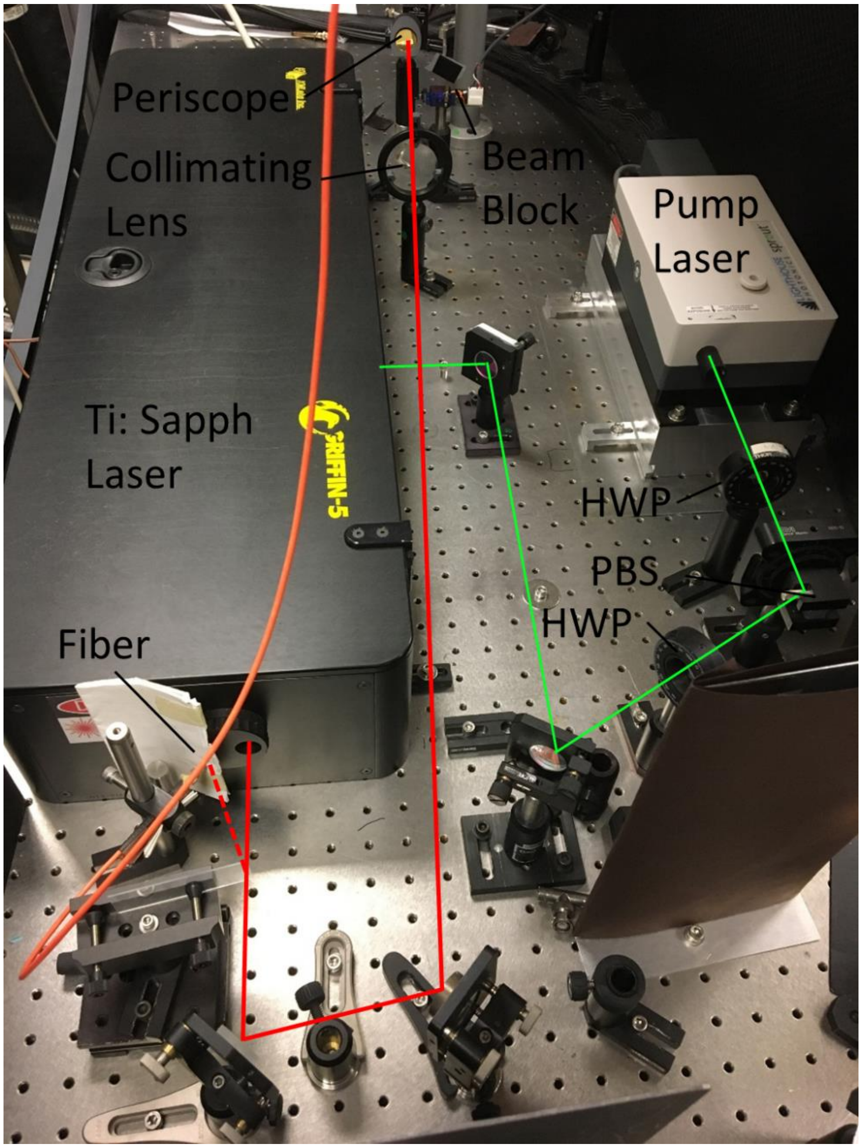

Figure 2.3. The optical setup for the pump and pulsed lasers. The pump laser passes through a half-wave plate (HWP) followed by a polarizing beam splitting cube (PBS) to enable power variation. It then passes through another HWP to adjust the polarization of the input to the pulsed laser. At the output of the Ti: Sapphire laser, a microscope slide is placed to allow a back-reflection to be analyzed by the spectrometer. The part of the beam not analyzed is then directed by two mirrors to a collimating lens and finally to a periscope system to raise the height of the beam to the chamber table. A computer-controlled beam block is located after the lens to block the beam during background measurements.

cavity. At the output of the pulsed laser, we had a microscope slide that could pick off about 10% of the beam near the output and send the reflection to a piece of paper. A fiber was placed by the paper to send the light to a spectrometer (20). This allowed us to monitor the output when trying to mode lock the laser. We want a spectrum with a wide FWHM, but it must also be stable over time. The spectrometer allowed us to see if the laser output was irregularly shaped or if it switched from mode-locked to CW mode. A sample spectrum can be seen in Fig. 2.4. This spectrometer was used to adjust the laser so that it had a center wavelength near 800 nm. At peak performance, the Ti: Sapphire laser is able to emit pulses as short as 15 fs in duration which can be measured using a frequency resolved optical gate (FROG). Alternately, the transform-limited pulse duration (the minimum pulse duration for a given FWHM) can be calculated using the FWHM and Heisenberg's uncertainty principle ($\Delta E\ \Delta t = \hbar$). A FWHM of about 60 nm corresponds to a pulse width of 15 fs.

The main beam would continue to two mirrors that direct it through a collimating lens and into a periscope assembly that enabled us to raise the height of the beam from the laser/optics table height to the chamber entrance height. Once past the periscope, the beam passes through another half-wave plate followed by a linear polarizer to allow us to adjust the power of the beam without changing the polarization (Figs. 2.2 and 2.5). The beam continues through a quarter-wave

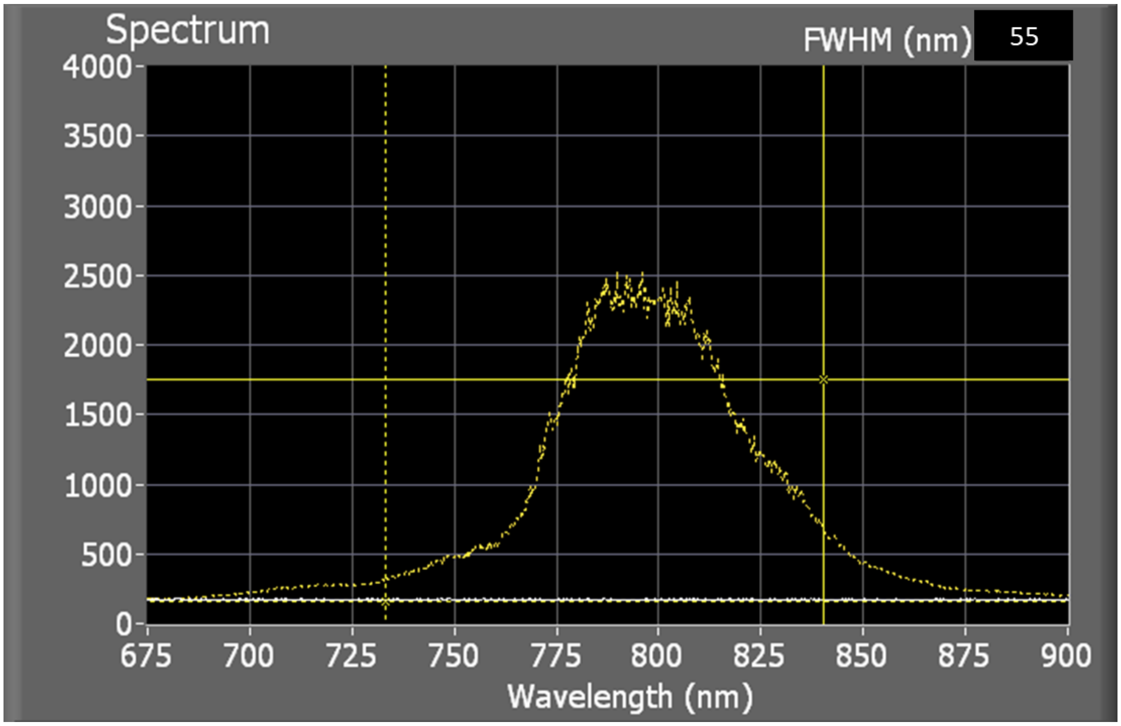

Figure 2.4. Laser spectrum. Typical spectrum obtained from the Ti:Saph laser when in pulsed mode. The ordinate has an arbitrary scale.

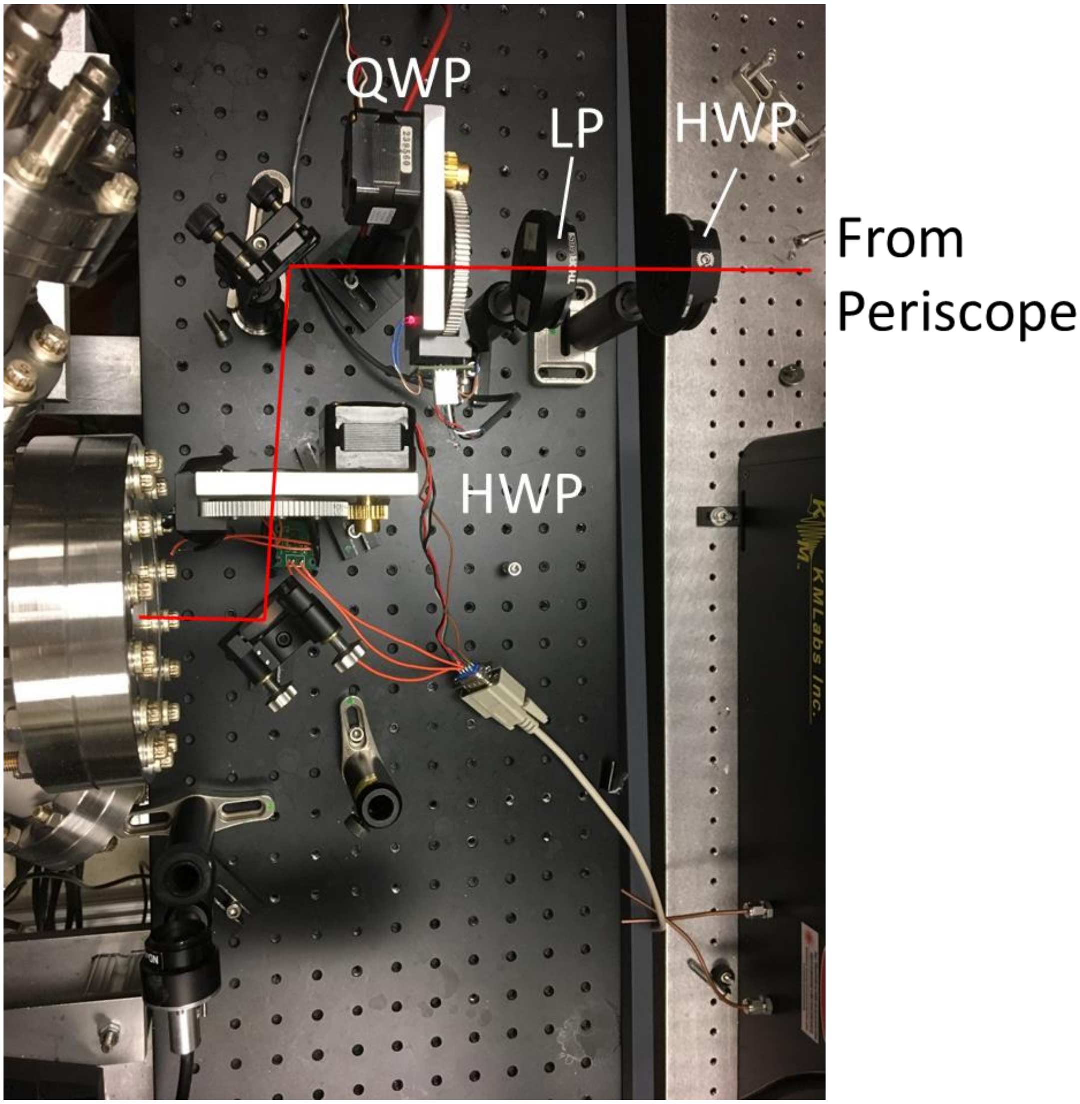

Figure 2.5. Optical setup at the chamber entrance. The pulsed laser beam comes from the periscope assembly in Fig. 2.3. It passes through a half-wave plate (HWP) and a linear polarizer (LP) to allow for adjusting the laser power entering the chamber. A computer-controlled quarter-wave plate (QWP) allows the laser to be circularly polarized or can be rotated to keep the laser linearly polarized if needed. A mirror then directs the beam through a computer-controlled HWP that allows us to adjust the angle of the linear polarization of the beam.

plate with computer-controlled angular position that is able to circularly polarize the beam or leave it linearly polarized depending on what measurements we wanted to take. A mirror redirects the beam to another half-wave plate to allow us to vary the linear polarization when we want to investigate the effects of linear polarization on photoemission rates or polarization. The half-wave plate merely flips the helicity of the beam when it is circularly polarized. A final mirror directs the beam into the source chamber. All mirrors used are either gold-coated first-surface mirrors or broadband dielectric mirrors (21). For the gold mirrors, since the first surface the laser encounters is the reflective part, there is negligible distortion to the beam's temporal structure since it doesn't travel through any material. The dielectric mirrors allow for reflection of a pulsed laser at our wavelengths without measurably distorting the shape of the beam or temporally broadening the pulses due to their high reflectance and similar reflectance of p- and s-polarization. Multiple types of mirrors were used solely due to availability of types of mirrors at the time the optics were aligned. Neither is significantly better than the other for the use we had for them.

This setup allows us to computer-control the polarization of the light without adding or removing any optics. We are able to obtain both helicities of circularly-polarized light as well as any direction of linearly-polarized light by rotating the half- and quarter-wave plates via the stepper motors that control the rotation. The rotators were equipped with a homing circuit that consists of an LED and a light sensor on opposite sides of the rotator. A small hole through the rotator allows for the LED light to be picked up by the sensor only when the rotator is at a specific angle. This allows us to reproducibly rotate back to the same position by monitoring the output of the sensor. We found all the positions for the circular polarization and linear polarization as a function of the number of steps from the home position. Fig. 2.6 shows the orientation for producing left-handed circularly polarized light.

The positions for the quarter-wave plate to produce light of a given polarization are shown in Table 2.1. Note that the handedness of the light listed for the quarter-wave plate is the handedness that the retarder produces. Since our setup includes another half-wave plate after the quarter-wave plate, the handedness of the light that enters the chamber is opposite that of what the quarter-wave plate produces. The positions for the two directions of linearly-polarized light that we used are also listed in Table 2.1.

One thing that worried us was that the beam position could move as we rotate the various wave plates. To check if this was happening, we set up a position-sensitive detector (PSD) (22) to monitor the position of the beam as we rotated the wave plates. The PSD consists of a square piece of GaAs with a side length of 10 mm. In both the vertical and horizontal direction, a voltage can be

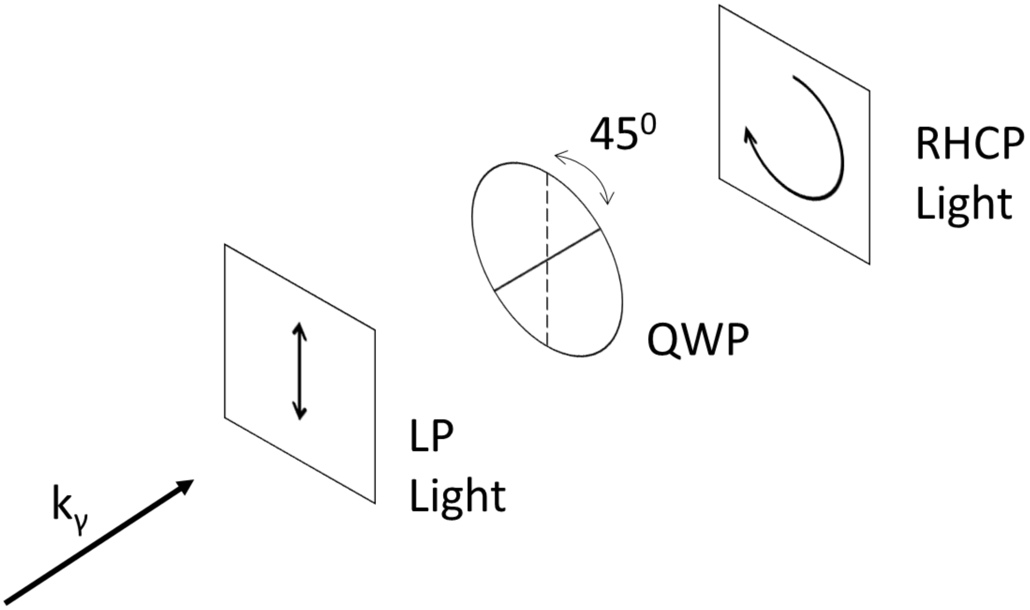

Figure 2.6. Circularly-polarized light production. Vertically-polarized light passes through a quarter-wave plate (QWP) that has a fast axis rotated 45^0 clockwise from the axis of linear polarization. This produces light that is right-hand circularly polarized. On the QWP, the dotted line depicts the direction of the linearly-polarized light and the solid line shows the fast axis of the retarder. The light's direction is also indicated.

Quarter-Wave Plate		
Polarization	**Steps From Home**	**Angle From Home**
RHCP	46	44.7
LP	91	88.5
LHCP	133	129.3
Half-Wave Plate		
Polarization	**Steps From Home**	**Angle From Home**
Vertical	0	0
Horizontal	41	39.9

Table 2.1. Stepper motor positions for light polarizations. List of the number of steps and the corresponding angle that the fast axis is from the home position for each rotator in order to produce the desired polarization for experiments.

measured when a laser is incident on the detector. These two voltages correspond to the (x,y) coordinates of the position of the maximum intensity of the beam spot on the detector. Each voltage output is between ± 10 V, and the device has a spatial resolution of 10 μm. By attaching these two outputs to an oscilloscope, we could check the amount of change the beam has as we rotate any of the optics. Within 10 μm, we could see no drift of the position of the maximum intensity of the beam for any of our wave plate orientations.

Setting up a GRENOUILLE (23) (a type of frequency resolved optical gate), we could measure the pulse duration of the beam just before it enters the source chamber. This measurement was done after all the optics other than the vacuum window so that we could measure the value of pulse duration closest to what would be incident on the sample. We measured the pulses to have a duration of 75 fs when it reached the chamber window. We believe this to be reasonable as the laser is capable of producing 15 fs pulses and we have no dispersion compensation optics. In an attempt to estimate the effect of the window on the pulse duration, we used data (shown later in Chapter 3) to estimate that the window doesn't appreciably change the duration of the pulse (< 10% change in pulse duration).

2.2 Source Chamber

Inside the chamber, the laser hits an off-axis parabolic mirror that serves to both change the direction of the beam from horizontal to vertical and focus the beam. The focal length of this mirror is 30 mm (Fig. 2.7 and Fig. 2.8).

The sample is mounted on a long rod that is attached to an XYZ translator that allows us to move any part of the sample into the focus of the laser. The two directions perpendicular to the axis of the electron optics are controlled by micrometer drives, each with a placement accuracy of 2 μm. The other dimension is less accurate (10 μm) due to it being controlled by a gear assembly with a digital output having a numerical resolution of only 0.01 mm. We wanted the sample to be electrically isolated from ground, so the end of the rod is a nonconducting

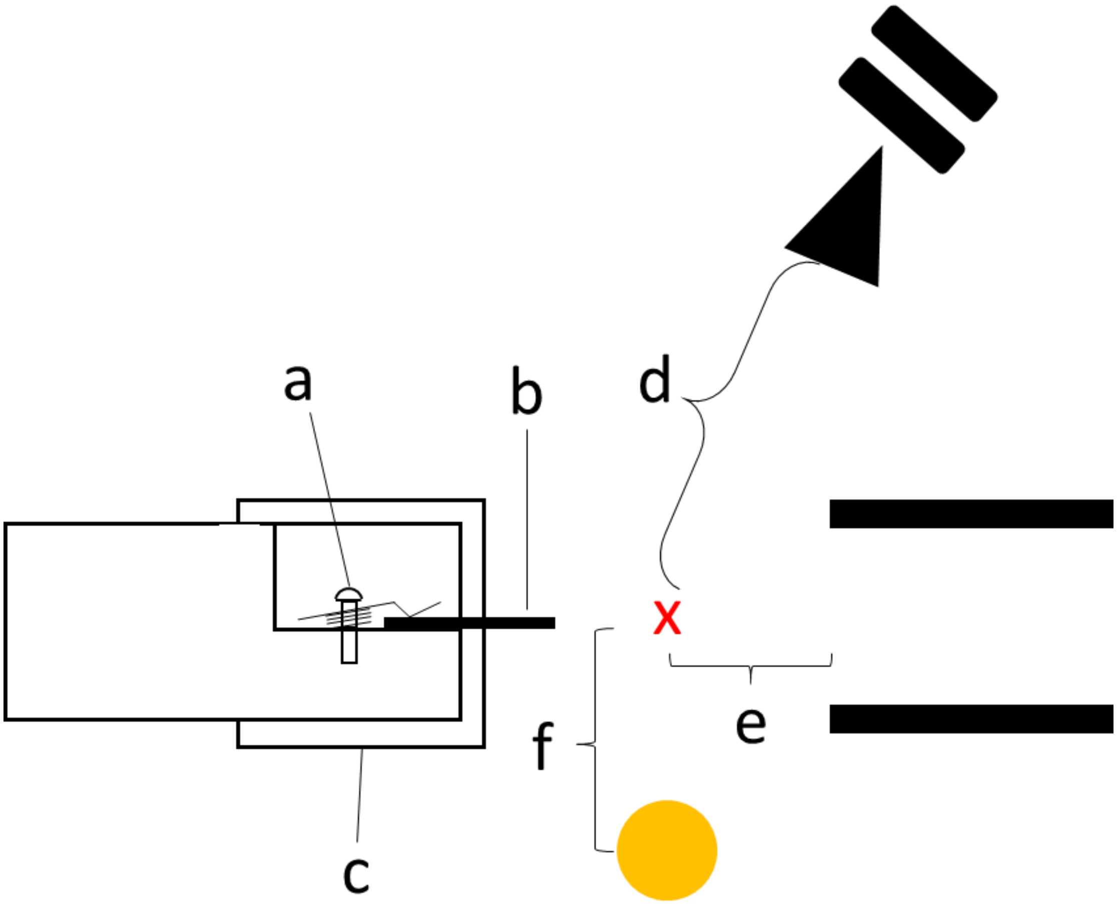

Figure 2.7. Detail (to scale) of the sample region. The sample holder can be seen on the left where a screw going through a spring (a) holds a bent piece of copper to apply pressure to the sample (b). A cylindrical cap (c) is fitted over the end with a small slot for the sample to stick through to give as flat a surface as possible around the sample's shank. A CEM is located a distance d = 5 cm away. The electron optics are at e = 2 cm to the right of the focus of the laser. The off-axis parabolic mirror has a focal length f = 30 mm.

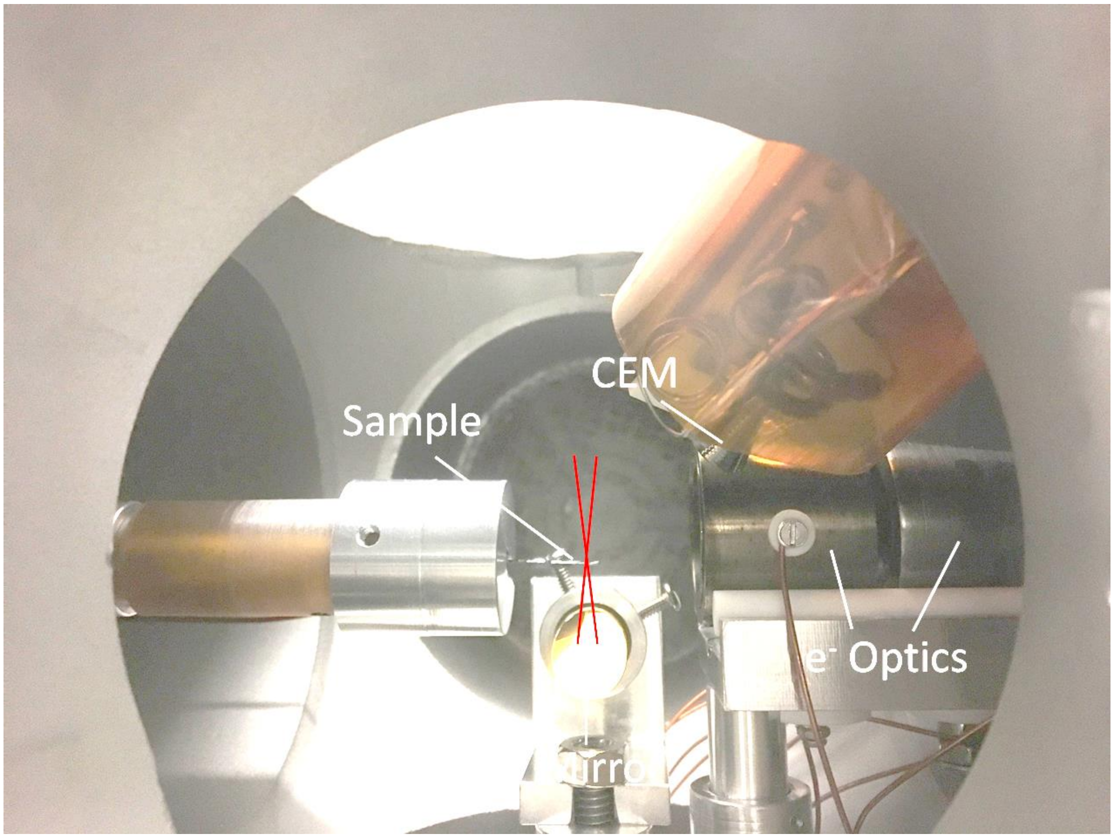

Figure 2.8. Photograph of the inside of the source chamber. The laser enters into the page and hits the mirror to be reflected up to its focal point. The sample is positioned inside the focus of the laser (red lines depict the outer edge of a beam that is focused on the sample). A channel electron multiplier (CEM) is nearby to collect total emission data, or electron optics can direct electrons toward the polarimetry chamber.

mount made from Ultem. The sample is held to the Ultem using a piece of copper that can be tightened with a screw to clamp the sample on the mount. A cap then goes over the end of the mount with a small slot for the sample to stick through and with a flat face. Voltage can be applied to this cap to push any emitted electrons toward the transport optics. Off to the side, located approximately five centimeters from the sample, is a CEM which allows us to determine the total emission from the sample.

Between the sample and the polarimeter chamber is an Einzel lens setup that consists of three electrostatic lenses made of molybdenum. The first and last of these are perpendicular pairs of electrostatic dipoles that allow us to move the beam vertically and horizontally. Fig. 2.9 shows an end view of the perpendicular dipoles. For each pair of dipoles, there are 3 voltages that we control. The first is the median voltage of the pair of dipoles, which is set by a power supply. The other two are the separation voltages of the top/bottom pair and the left/right pair. We set a voltage on a separate power supply that determines the maximum voltage between them, then use dual potentiometers (two potentiometers controlled by the same dial) to make the voltages for each pair symmetric about the median voltage. The electrical circuit that allows us to do this is also shown in Fig. 2.9. This three-lens setup allows us to adjust the path of the electron beam as well as focus the electrons without affecting their spins.

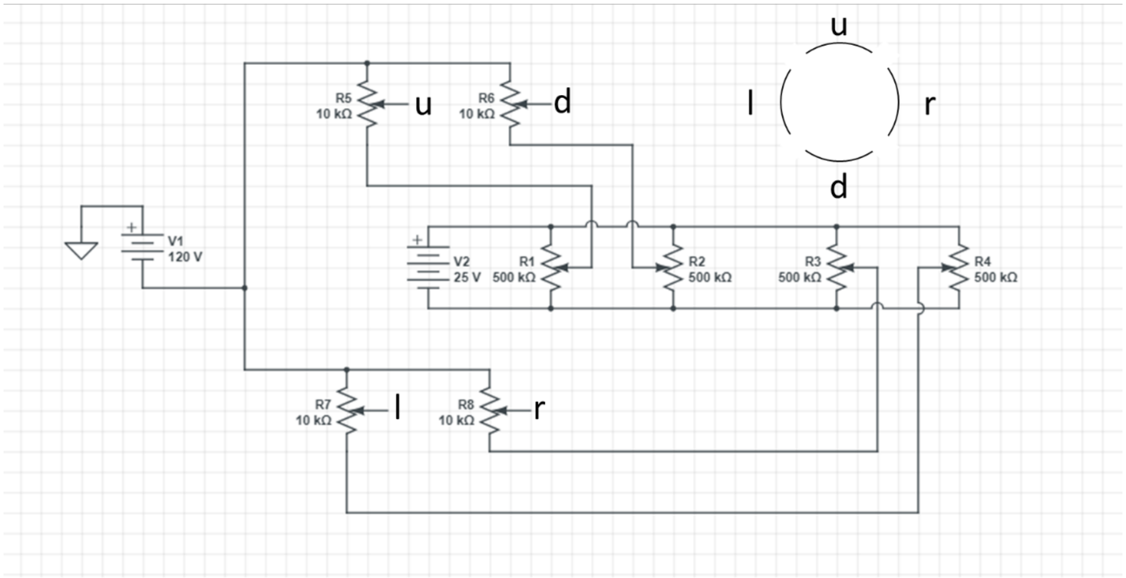

Figure 2.9. The electrical circuit used to control the pairs of dipoles for each element of the Einzel lens. The "up" and "down" elements u and d were connected to the same dual potentiometer so that they maintain the median voltage set by V1. The "left" and "right" elements l and d were similarly connected via a dual potentiometer.

Computer simulations (24) were conducted to determine if the Einzel lens alone was sufficient to direct electrons toward the entrance of the Mott polarimeter. While we only used a small circle to model the source in these simulations (as opposed to a sharp tip), the distances used between elements in the simulation are approximately equivalent to our actual dimensions (Fig. 2.10). We were unable to model the pairs of dipoles, so we treated them as a cylinder with a constant voltage on the entire surface. The simulation showed us that there is a reasonable expectation to collect most of the electrons emitted from the sample on the Mott polarimeter target.

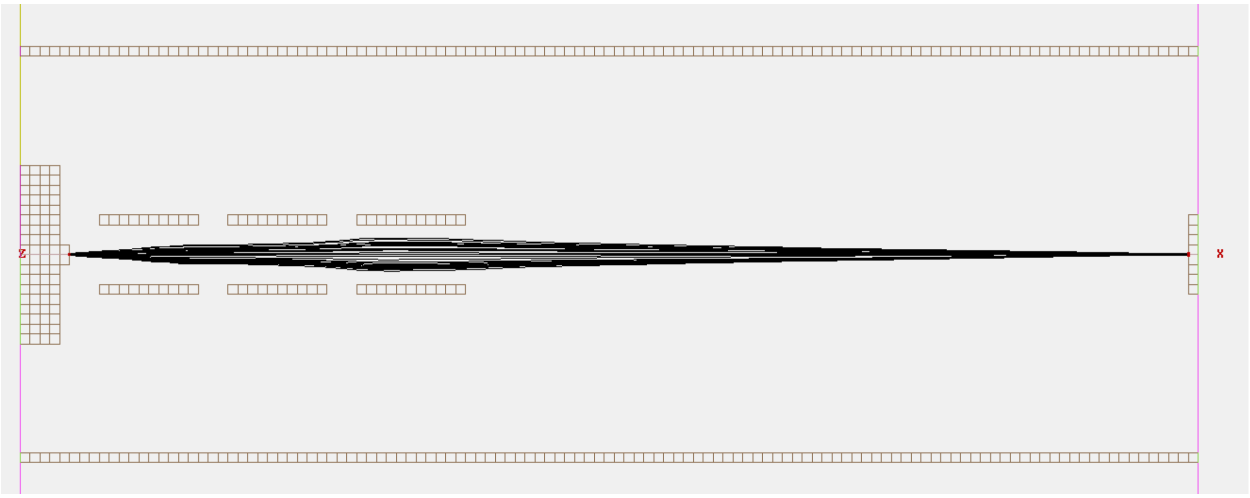

Figure 2.10. SIMION simulation; the electron trajectories originate at the sample surface on the left, passing through the three elements of the Einzel lens and hitting the Mott polarimeter entrance on the far right.

With the sample biased at -100 V, focusing conditions for the beam were relatively insensitive to individual voltages as long as two of the sections had approximately equal voltages and no voltage was more negative than the sample bias. The element with a different voltage was able to change the spread of the distribution of electrons at the target, yet still showed a very robust range of values to still get all of the electrons to the target. When keeping the voltages on the first two elements equal in the simulation, the range of voltages on the last element that still kept most electrons on target was anywhere from -100 V to +600 V. The optimal simulated values seemed to be between +100 V and +150 V with the first and second element at 0 V.

A scale drawing of the electron lens stack is shown in Fig. 2.11. The lens elements are supported by an aluminum channel with small Macor rods in the channel that keep the elements electrically isolated from ground and from each other. The voltages on each element are given in Table 2.2. Finding these voltages consisted of using an electron gun placed where the sample normally is and adjusting the voltages until the current on the target was maximized. Once these voltages were found, we never needed to change them again as this gave a maximum number of electrons on target for the sample bias we used and any variation we tried yielded no extra electrons on target.

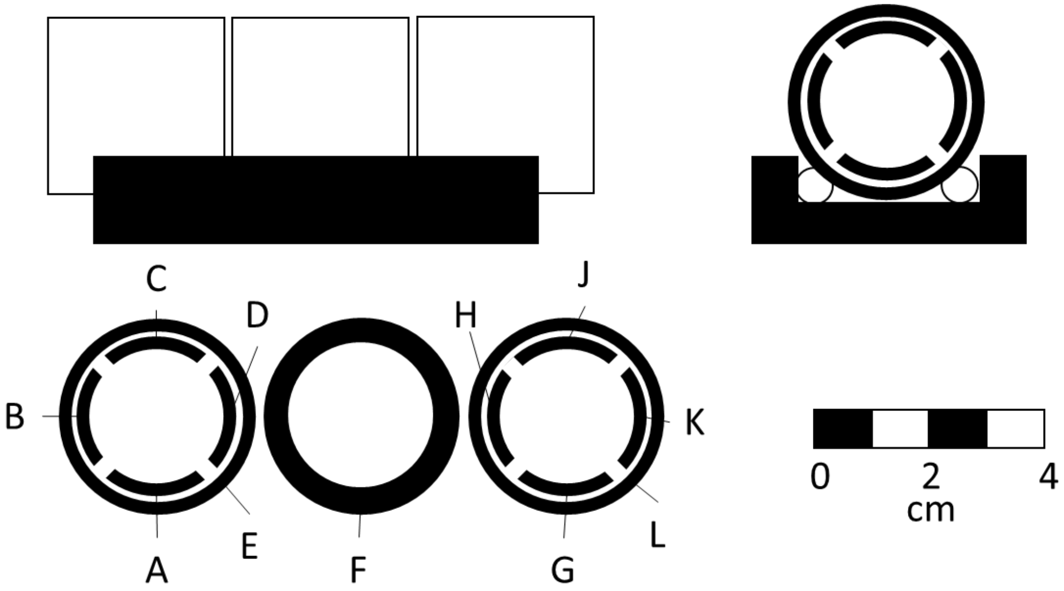

Figure 2.11. The electron transport lens stack. Scale side view (top left) and an end view (top right) of the electron lens on the rail. The small circles on the end view represent ceramic (Macor) rods that keep the electrostatic elements electrically isolated. A cross section of each piece is shown on the bottom with labels that correspond to the element labels with voltages in Table 2.2.

As is usually true, the optimal values for the simulation didn’t completely match up to the voltages we used for the elements. Table 2.2 shows that the first pair of dipoles were centered around 28 V as was the middle element in the lens stack. The last set of dipoles were centered around 108 V. When these values were entered into the simulation, the electrons were still on target, but not as well focused, but the simulation doesn’t take into account any external fields that our working voltages may have been countering.

A	26.4	**F**	28.5	**G**	108.1
B	27.1			**H**	108.2
C	30.1			**J**	108.1
D	29.4			**K**	108.2
E	28.2			**L**	108.2

Table 2.2. Operating voltages for each element of the electron lens stack. The letters correspond to the labeled elements in Fig. 2.11. Once these voltages were found, they were not adjusted again.

2.3. Target Chamber/ Mott Polarimeter

The target chamber contains our Mott polarimeter. For our experiments, we used a modification of a Mott polarimeter that makes it more compact than a standard version (25). A full analysis of the new polarimeter is carried out in (25), but a synopsis will be given here.

The Mott polarimeter is only sensitive to the component of polarization along a vertical axis (parallel to the axis of our polarimeter) which is perpendicular to the incident beam's momentum. The polarimeter consists of a high-Z target (typically gold) from which the electrons can scatter and two CEM detectors that are located symmetrically to either side of the incident beam path. Due to spin-orbit interactions, there is a left-right asymmetry of the scattered electron signal measured at an azimuthal angle of $\pm 90^0$ that can be used to calculate a polarization.

At a given polar scattering angle and electron energy E, we define the Mott scattering asymmetry (26) as

$$A(\theta, E) = \frac{N_L - N_R}{N_L + N_R}, \tag{2.1}$$

where $N_{L,R}$ are the electron counts for a given data acquisition period in the left and right detectors respectively. If there is no instrumental asymmetry, then *A(θ,E)* is proportional to the polarization of the beam, i.e.

$$A(\theta, E) = PS_{eff}(\theta, E), \tag{2.2}$$

where the analyzing power for the scattering, $S_{eff}(\theta, E)$, is called the "effective" Sherman function. The value of S_{eff} depends on several factors such as target material, polar scattering angle, incident electron energy, and energy loss of the detected electrons. We defined energy loss, ΔE, as the maximum amount of energy an electron can lose as it scatters from the gold target and still be detected (26).

2.3.1 Mott Polarimeter Design

"Retarding field" polarimeters decelerate scattered electrons with the same field used to accelerate the incident electrons to the target. They most often consist of a pair of electrodes that have either cylindrical (27) or quasi-hemispherical (15) symmetry. Due to the retarding field for scattered electrons, inelastically scattered electrons can be electrostatically rejected, which eliminates the need for energy analysis by the electron detectors themselves (28). In previous retarding field designs, the high-Z target was contained inside the inner electrode and would be biased slightly negatively compared to the inner electrode. This slight potential difference would prevent any positive ions that are sputtered from the target surface from being accelerated into the detectors (28). The detectors are placed just outside the outer electrode and are held at or near the potential of the outer electrode.

Simpler and more compact polarimeter designs are easier and less expensive to make, and they are much easier to place and move around in a chamber. They also tend to have a higher "figure of merit", $\eta = S_{eff}^2 \frac{I}{I_0}$, where I_0 is the incident particle current and I is the detector count rate. The figure of merit is inversely proportional to the square of the time required to make a polarization measurement to a given statistical precision (1). Retarding field polarimeters are well suited to size reduction. These so-called "micro-Motts" of compact quasi-hemispherical or conical design have been highly refined (29) (15) (30) (31), but to my knowledge, compact *cylindrical* retarding field designs have not been realized previously.

We have designed a simple, compact Mott polarimeter with cylindrical symmetry. Although it is almost double the size of the smallest retarding field “micro-Mott” devices with a spherical geometry (30), it is significantly simpler, using a monolithic target structure and simple detectors without entrance optics. Our design does not use a double inner electrode structure like conventional retarding field polarimeters, but instead uses a single inner electrode that also serves as the target.

The reason this design had not been developed before was based on at least two serious (perceived) problems that it was thought to have. The first was that, unlike polarimeters with a planar target inside the inner electrode, it was assumed that a small misalignment of the beam would result in large fluctuations in the detected asymmetry (26). The second was that it was assumed that positive ions sputtered from the target would reach the detectors and cause spurious background counts. These concerns were investigated and found to be negligible when operation occurred above a certain energy loss window, ΔE.

A simplified view of our polarimeter is shown in Fig. 2.12. Its simple design makes it much easier to construct without the use of highly specialized tools and could even be made in a student workshop if sufficient care is taken. Our CEMs are mounted at polar angles of $\pm 120^0$ from the incident electron momentum direction. The CEMs have a 2.5 cm diameter opening (32). This corresponds to approximately a 20^0 polar scattering angle that can be accepted into the detectors. When operating, the gold rod is held at a voltage around +20 kV. A comparison of the operating parameters of our Mott polarimeter to those of other designs is given in Table 2.3.

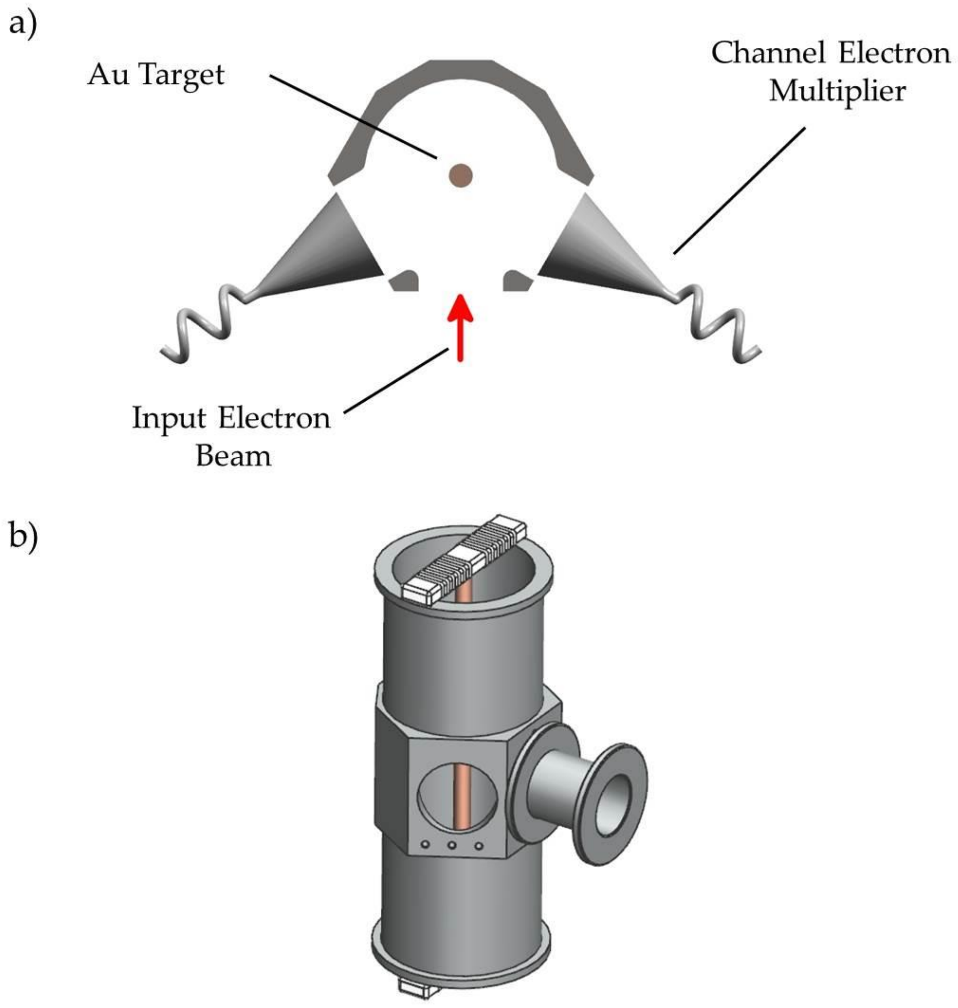

Figure 2.12. Schematic top sectional (a) and isometric (b) views of the polarimeter. The channel electron multiplier detectors are not shown in (b). The incident electron direction is indicated in (a). The electrons enter in (b) through the spool-like opening on the right side. This spool is able to be floated in order to adjust the focusing of the incident electrons. The white, crenelated bars on the top and bottom are ceramic pieces designed to electrically isolate the target rod from the rest of the polarimeter and reduce the likelihood of unintended charging and/or arcing. Image from (25).

Ref.	Laboratory	Max. Seff (%)	ΔE (eV)	Max. η (10^-5)	ΔE (eV)	Seff at max. η (%)	Notes
(30)	Rice	23	400	13	400	23	a
(33)	Rice	21	300	12	700	15	b
(26)	Rice	11	1300	2.4	1300	11	
(31)	Rice	11	1300	2.7	1300	11	
(34)	Irvine	20	500	1.4	1000	14	c
(35)	Taiwan	13	700	~2			d
(36)	Tokyo	13	600	18	1200	10	
(37)	St. Petersburg			4.5			e
(38)	Edinburgh	9	1300				
(29)	JLab	20	0	1	268	14	
This work	Lincoln	24	500	1.1	1100	18	
This work Th adj.	Lincoln	29	500	1.7	1100	21	

a) Th Target 25 keV, max η occurs over range of ΔE from 400 to 1000 eV

b) Th target

c) U target

d) 23 keV

e) 30 keV; Ref (30), (33), indicate little change in η between 20 and 25 keV at 1300 eV

Table 2.3. Comparison of various "micro-Mott" designs at 20 kV with Au, Th and U targets. To facilitate comparison between our Au target polarimeter and devices that used Th targets we have scaled S_{eff} , I/I_o and η of our polarimeter using the method described in (29). The adjusted values are presented in the last row of the table. Table adapted from (25).

2.3.2 Scattering Asymmetry

As mentioned earlier, when the electrons scatter from the Au target, there will be an asymmetry in the count rate of the two detectors if the electrons have a polarization parallel to the axis of the Mott polarimeter (1) (26). The asymmetry will be proportional to the polarization of the beam as shown in eqn. 2.2. The circuit that was used for each CEM is shown in Fig. 2.13. For any detectors, even if both are the same model, there will be differences in efficiency and overall detection rate due to electronic and geometric differences. The fronts of the CEM and the outer electrode are held at +500 V. The backs of the CEMs were held at different voltages in an attempt to balance the two detector's efficiencies. One was initially held at +3000 V and the other was held at +3500 V. Slight differences don't affect measurements we make systematically due to the data analysis methods which will be described next. Over time, the voltages were increased to maintain as best we could the detection efficiencies of each CEM. After approximately 1.5 years of use for experiments, the voltages had been increased to +3500 V and +3800 V.

If we use detectors of different efficiencies and calculate an asymmetry using eqn. 2.1, then all our results would have an offset. For example, if there is an unpolarized beam incident on the polarimeter, and we had equally efficient

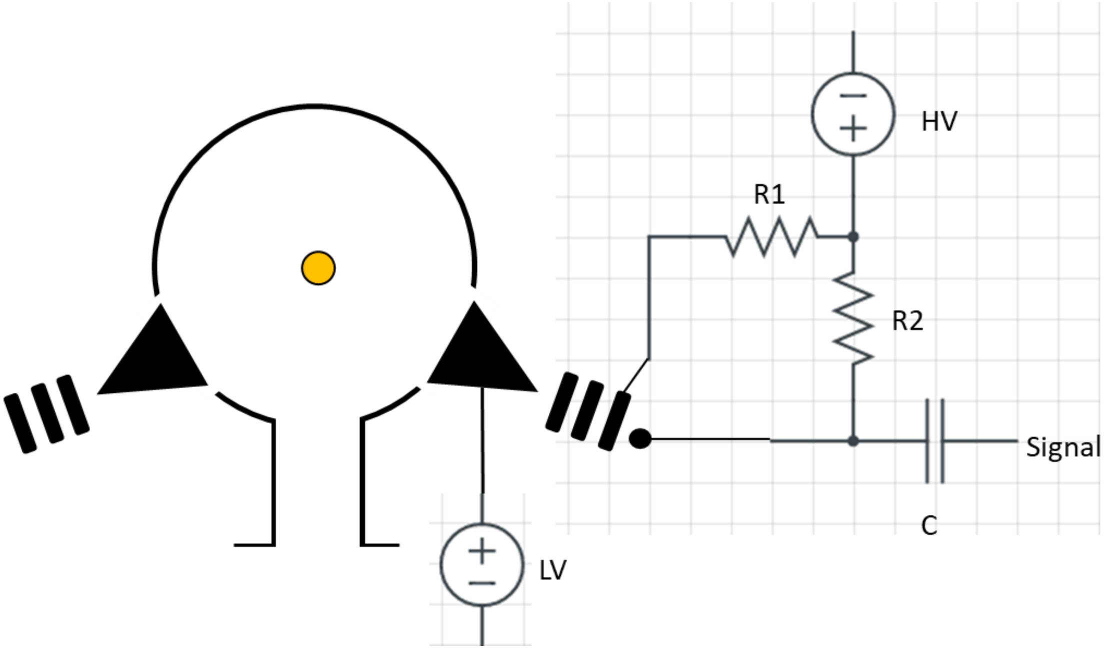

Figure 2.13. Mott polarimeter with electrical circuit. Simplified top view of the Mott polarimeter as well as the electrical circuit used to apply voltages to the CEMs. Each CEM has a separate circuit. Values for the different circuit elements are R1 = 1 MΩ, R2 = 10 MΩ, and C = 250 pF. The low voltage (LV) on the front was +500 V and the high voltage (HV) on the backs of the two detectors were originally +3000 V and +3500 V.

detectors, we would obtain the same count rates for each detector and correctly measure the polarization to be $\frac{1-1}{1+1} = 0\%$. However, if one detector is only 50% as efficient as the other, using the same equation, we would measure a polarization of $\frac{1-0.5}{1+0.5} = 33\%$. For this reason, we cannot calculate the asymmetry by using eqn. 2.1, but must calculate the asymmetry in such a way to eliminate any effects of detector efficiencies (26):

$$A = PS_{eff} = \frac{X-1}{X+1}, \tag{2.3}$$

where

$$X = \sqrt{\frac{R_L R'_R}{R_R R'_L}}, \tag{2.4}$$

and the detector count rates *R* have subscripts indicating if they are the detector to the "right" or "left" of the incident electron beam. The prime indicates the rates when the spins of the incident electrons have been flipped, e.g., optically.

One concern of ours was that small changes in the incident electron beam's position would cause a change in the effective Sherman function or cause an offset to the polarization calculations. This turned out not to be a problem due to the large electrostatic focusing caused by the electric field between the target rod and the outer electrode. Even large movements of the input beam to the side (as long as the electrons still made it into the polarimeter) caused by electric dipoles upstream from the polarimeter didn't cause any significant change in the device's analyzing power.

2.3.3 Sherman Function Calculation

We used a GaAs electron source to calibrate our Mott polarimeter's effective Sherman function. The polarization of the electron source was separately measured by an optical polarimeter during a separate experiment (39). This allowed us to confirm the polarization of the source using two independent methods. As shown in eqn. 2.2, the Sherman function depends on the difference in energy from the source to the detectors of the electrons being detected. In order to properly characterize the polarimeter, we measured the Sherman function at different values of this difference in electron energy. To do this, we had the front entrances of the CEMs and the outer cylinder of the polarimeter at the same potential. Our source photocathode was held at a constant potential of -1000 V, so the potential difference was varied by changing the potential of the outer electrode and the detectors. This allowed us to measure the dependence of the Sherman function on ΔE, the maximum amount of energy an electron can lose during scattering and still be detected. A ΔE of 0 eV would correspond to detecting only electrons that were elastically scattered. The maximum value that we calculated for our effective Sherman function is 0.24. However, we also needed to look at the figure of merit, η. When looking at the dependence of these values on ΔE (Fig.

2.14), we want to operate at a ΔE such that we have both a high Sherman function as well as a high figure of merit so that we obtain precise data in a reasonable amount of time. For this reason, we chose to operate at ΔE = 600 V, since the figure of merit doesn’t increase appreciably at higher values of ΔE, and the Sherman function is still near its maximum value. When at these settings, our effective Sherman function is 0.23.

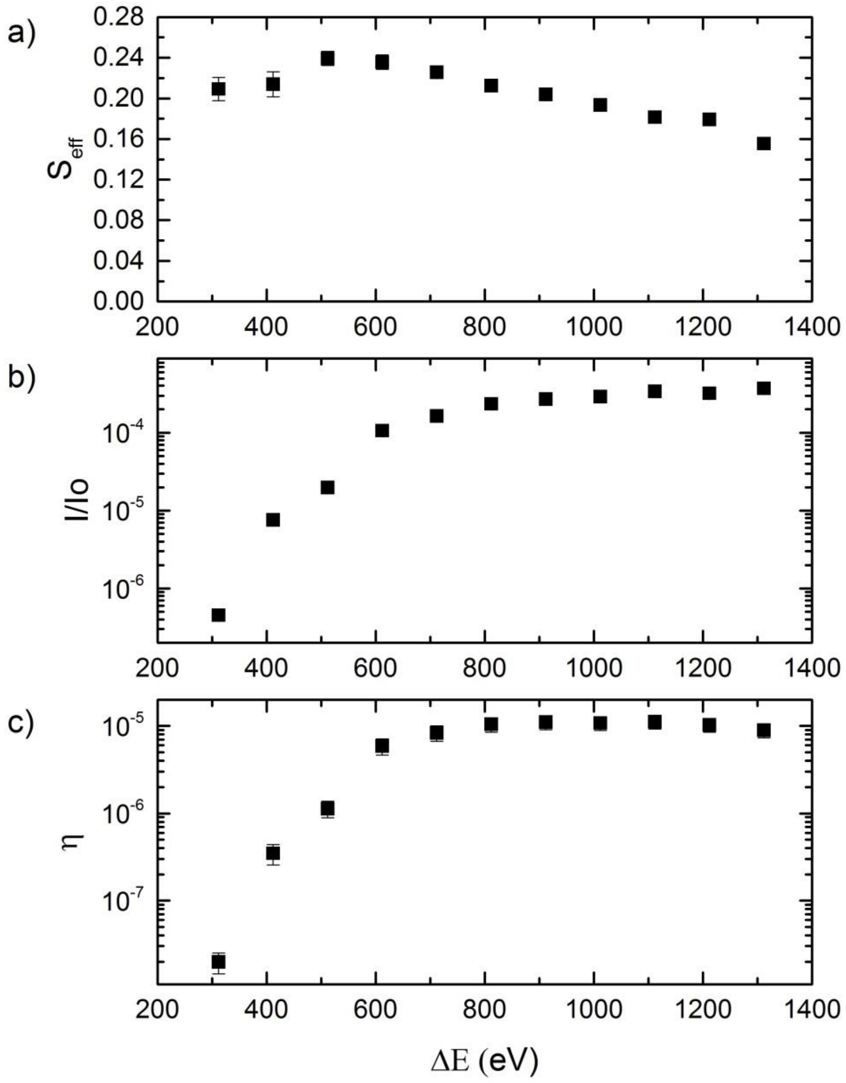

Figure 2.14. Parameters of the polarimeter. Variation as a function of ΔE of (a) the effective Sherman function, S_{eff}; (b) efficiency, I/I_o; and (c) the figure of merit, η. The incident electron energy was 200 eV with a target bias of 20 kV. Figure from (25).

Chapter 3. Bulk GaAs

For this dissertation, three different samples were investigated to determine if they could potentially be used as a viable source for polarized electrons. Each sample was chosen to investigate if their various characteristics would cause the emitted electrons to be spin-polarized. In the following chapters, we will explain our motivations for choosing each sample, describe preliminary investigations into each of them, and discuss the results for each sample.

3.1 GaAs Introduction

The first sample we chose was GaAs as it is the same material that is used in the current state-of-the-art sources. As stated in Chapter 1, we wish to create a source that foregoes the use of an NEA surface. We also wished to find a way to benefit from the selection rules for excitation of the conduction band from the valence band that leads to polarization in the standard NEA bulk GaAs source (9). Using the Ti: Sapphire pulsed laser (18), we obtain very intense pulses of light that can cause the electrons in the GaAs to absorb multiple photons (Fig. 1.2a). This process is akin to resonantly enhanced multi-photon ionization (REMPI) because we are using a wavelength that matches the band-gap of the GaAs.

3.1.1 Multiphoton Emission

Multiphoton emission is an extension of the photoelectric effect, in which an electron absorbs a single photon that has an energy greater than or equal to the work function of the material being investigated in order to be emitted. Multiphoton emission occurs when a light source is so intense that more than one photon can be absorbed by the same electron so that the combined energy of all the photons absorbed are more than the work function (40). Normally an electron can't absorb a photon unless the photon energy is equal to the energy difference between two states in the material. For multiphoton absorption, you can instead picture the electrons temporarily being excited to a virtual state at an energy equal to the photon's energy above the initial state. Fig. 3.1 illustrates the idea of such virtual states. The lifetime of these virtual states is governed by the uncertainty principle, $\Delta E\ \Delta t \geq \hbar$, where ΔE is how far from a real state the virtual state is (40). This gives virtual states a lifetime that depends upon the material used and wavelength of light used, but for our materials and laser, it is approximately 0.5 fs. So, for low intensities of light, an electron will have decayed back to a real state before another photon is absorbed.

A full analysis of this process is given in (40), but a simplified explanation will be given here. We start by describing the rate of a one photon absorption process as

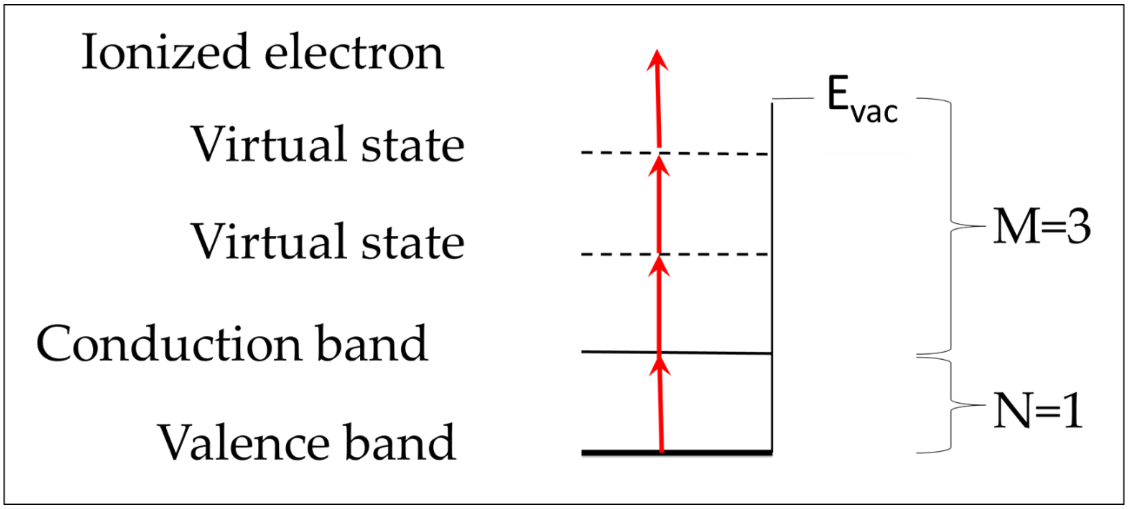

Figure 3.1. Multiphoton emission diagram. A simplified view of multiphoton emission from a material with an excited state (typically the conduction band). The process can be viewed as an N-photon process plus an M-photon process. In the M-photon process, as long as another photon is absorbed before the electron has decayed from the virtual state, it will be able to be excited to the second virtual state and then to the vacuum if a third photon is absorbed before it decays.

$$\omega = \sigma I, \tag{3.1}$$

where σ is the absorption cross section with units of cm^2, and I is the intensity of the laser with units of $photons/cm^2 \cdot s$. In a two-photon process, the first photon will follow eqn. 3.1, and we include a multiplicative factor to describe a second photon being absorbed while the electron is in a virtual state of lifetime τ:

$$\omega_2 = (\sigma_1 I \tau)\, \sigma_1 I = \sigma_2 I^2, \tag{3.2}$$

where $\sigma_2 \equiv \sigma_1^2 \tau$. This equation can be generalized for an N-photon process as:

$$\omega_N = (\sigma_1 I \tau)^{N-1}\, \sigma_1 I = \sigma_N I^N, \tag{3.3}$$

where $\sigma_N \equiv \sigma_1^N \tau^{N-1}$.

Eqn 3.3 describes an N-photon process with no resonant state. If the material contains an excited state that the electron passes through, it becomes a process that has two steps, namely, an N-photon process followed by an M-photon process (Fig. 3.1). If this is the case, it becomes easier to look at the probability of N photons being absorbed to see how often we should expect an electron to be emitted.

To investigate this probability, we describe the intensity of the laser as $I_0 = f(t)g(\boldsymbol{r})I$, where I is the maximum intensity of the laser pulse, f(t) is a function that describes the temporal properties of the pulse, and g(**r**) is a function that describes the spatial properties of the pulse. We define it in this way so that f(t) and g(**r**) have maximum values of one. We also constrain f(t) by saying that

$\tau = \int_{-\infty}^{+\infty} f(t)dt$, where τ is the pulse duration. The function g(**r**) is defined by $V = \int g(\boldsymbol{r})dr$, where V is the volume of material with which the beam interacts. For our analysis, we use g(**r**) = 1 to give a "best case" value. When combining all of these, we get that the probability of exciting a single electron is (40)

$$P = 1\text{-}\exp(-\int_{-\infty}^{\infty} dt\ f^N(t)g^N(\mathbf{r})\sigma_N I^N) = 1 - e\text{^}(-\sigma_N I^N \tau), \qquad (3.4)$$

where τ is the lifetime of the virtual state or the pulse duration, whichever is shorter. This is because we want the electron to absorb another photon while the laser is still hitting it and while it is in the virtual state, so whichever has the shorter duration will be the limiting factor.

For a non-resonant process, eqn. 3.4 gives the probability of exciting an electron. If there is a real state that the electrons pass through (Fig. 3.1), we must calculate the probability of the N-photon process and the M-photon process both happening. This leads us to a total probability

$$P = P_{\text{excitation}} \times P_{\text{ionization}}; \qquad (3.5)$$

$$P = (1 - e\text{^}(-\sigma_N I^N \tau_1))(1 - e\text{^}(-\sigma_M I^M \tau_2)). \qquad (3.6)$$

The value of σ_1 will depend on the material, but from (41), we obtain values for the absorption coefficient, α, for GaAs and can use the relation $\alpha = \sigma N$, where N is the concentration of atoms. GaAs has eight atoms per unit cell, which allows us to calculate that GaAs has $\sigma_1 = 4.509 \times 10^{-19}$ cm^2. Using this equation and the properties of our laser, we calculate a theoretical emission rate. Using the 10 nJ/pulse energy of our laser and a center wavelength of 800 nm and a pulse duration of 75 fs along with a focal spot radius of 25 μm gives us that $I \approx 3 \times 10^{28}$ photons/cm^2·s. Then, using the pulse duration for τ_1 and the lifetime of the virtual state for τ_2, as those are the limiting factors for each transition, we calculate a probability of a single pulse emitting an electron from an atom to be on the order of 10^{-19}. We can then multiply this by the repetition rate of the laser (100 MHz) and the number of atoms that are in the illuminated volume to find our theoretical emission rate. Using the density of atoms in GaAs and multiplying that by the volume of a cylinder with a base area equal to the area of our focal spot and a height equal to the penetration depth defined as $\delta = 1/\alpha$, we can calculate a "best-case" value of about 2 kHz. Our calculation assumes equal intensity over the entire volume, which we know to be untrue, but this was merely to find a rough estimate for emission rates. We then set up an experiment to emit electrons from GaAs.

3.2 Emission from GaAs

Our first task was to investigate if it was even possible to obtain emission from GaAs using multiphoton absorption. To do this, we set up a simple chamber (Fig. 3.2) that uses linearly-polarized light to emit electrons. We could adjust the power of the beam and the direction of the linear polarization using two half-wave plates with a linear polarizer between them. For the GaAs, bulk crystals purchased from Crystal Specialists were used. They are approximately 0.3 mm thick, Zn-doped p-type wafers (<100> orientation) with a dopant carrier concentration of

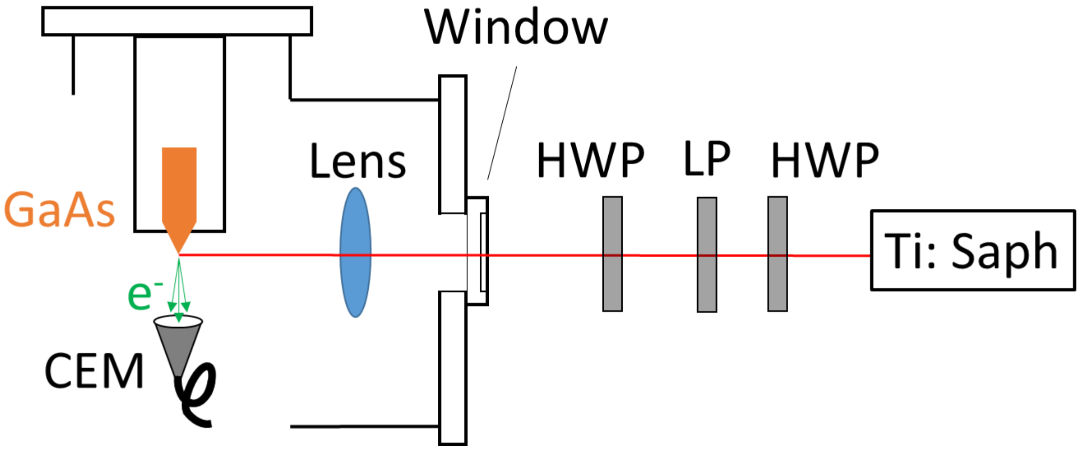

Figure 3.2. Schematic of my first experimental chamber. The Ti: Saph laser passes through a half-wave plate (HWP) followed by a linear polarizer (LP) in order to adjust the power transmitted. That is followed by another HWP to be able to rotate the linear polarization. Inside the chamber is a lens that focuses the laser onto the GaAs. Emitted electrons are collected by the channel electron multiplier (CEM).

~2 x 10^{19} cm^{-3}. The main effect of this very heavy doping (0.06% by weight) is to cause significant band bending near the bulk surface, as shown in Fig. 1.2.

We first had the laser incident on the bulk GaAs near the center of the sample. We quickly realized that it was difficult to get any emission. There would be occasional "hot spots" that would emit up to 20 Hz, but it appeared that these spots were not in any specific part of the crystal and we believe that they were due to surface irregularities. Away from these "hot spots", we saw little or no emission (< 3 Hz). While exploring the surface of the GaAs, we moved the sample so that the beam was focused on an edge and saw that the GaAs would emit around 10 Hz anywhere along the edge. We then moved to a corner and saw a further increase in emission. Fig. 3.3 shows that by moving to a tip, we could increase our emission by several orders of magnitude. So, for the rest of the experiments involving bulk GaAs, we used sharp pieces (as determined by an optical microscope) to obtain emitted electrons. When using a piece that we checked optically for sharpness, we obtained maximum emission currents on the order of 4 nA (~10^{10} Hz).

Having established that we could observe significant emission currents from GaAs, we started preliminary investigations into the emission properties. The first was to measure the emission rate as a function of the laser power. By assuming a simple non-linear, multi-photon emission picture and fitting the data

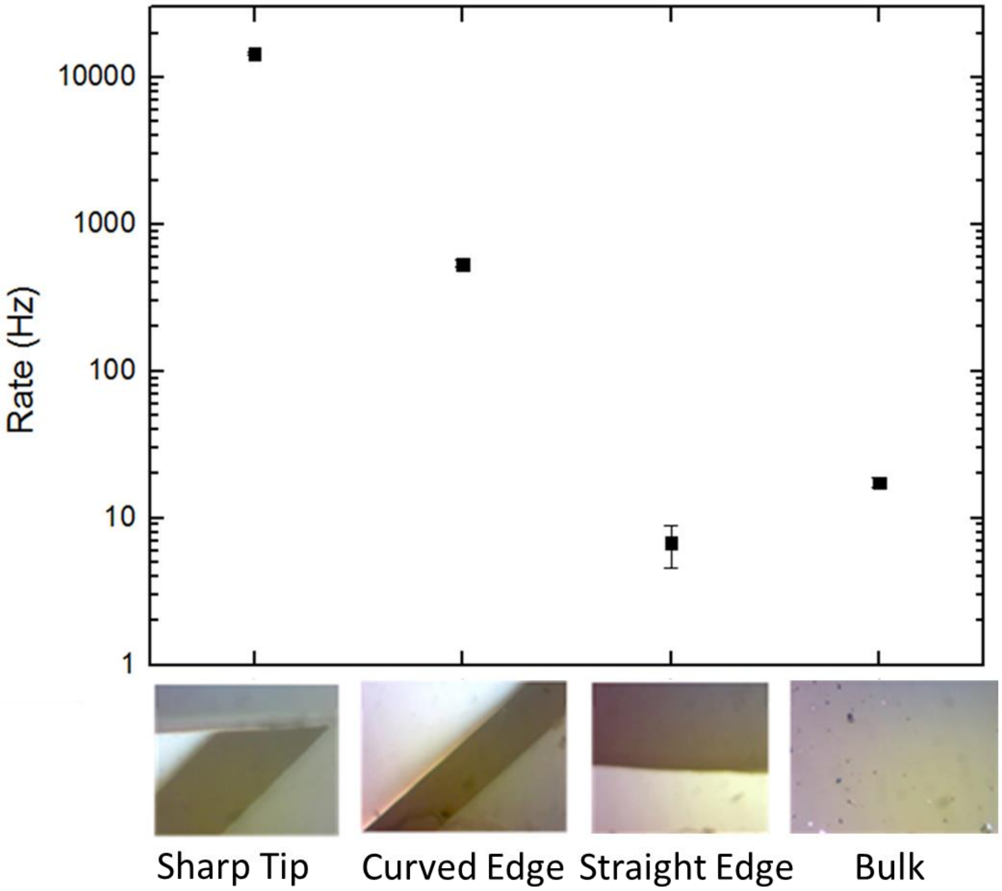

Figure 3.3. Emission rates for various positions of laser incidence on the bulk GaAs crystals. Tips gave the most emission whereas the bulk and a straight edge gave the least. Laser power was approximately 90 mW with pulse durations of no more than 75 fs. The Ti: Sapphire laser operated at 100 MHz rep rate.

to an equation R = A*P^N (coming from eqn. 3.3), where R is the rate of emission and P is the laser power with A and N being the fitting parameters, we find a value for N, the number of photons needed to emit an electron. While this fit doesn't take into account the two different transitions needed to emit an electron, it gets us a good fit for the data while simultaneously giving a value of N that is similar to the number of photons needed for emission. For a complete equation, one would need to Taylor-expand eqn. 3.6 which ends up being a Bessel function and is overly complicated for us to calculate for every graph we made. Typical sets of data are best fit using A*P^N with values of N that range from 3 to 5 depending on various parameters such as the sharpness of the tip and the intensity of the laser. The sharpness of the tip changes N since even a small change in voltage on a sharp tip can dramatically change the field allowing for electrons to be emitted with fewer photons. The value of N is also dependent upon laser intensity since larger intensities will saturate the transition from the valence band to the conduction band and cause the value of N to decrease. An example of this data is shown in Fig. 3.4 that gives us a value of N = 4.15 ± 0.07. The value is not expected to be an integer because this value represents an averaging over all the mechanisms of emission (e.g. multiphoton emission, tunneling emission, and thermal emission) (17), so integer values for N are rare and not considered the norm.

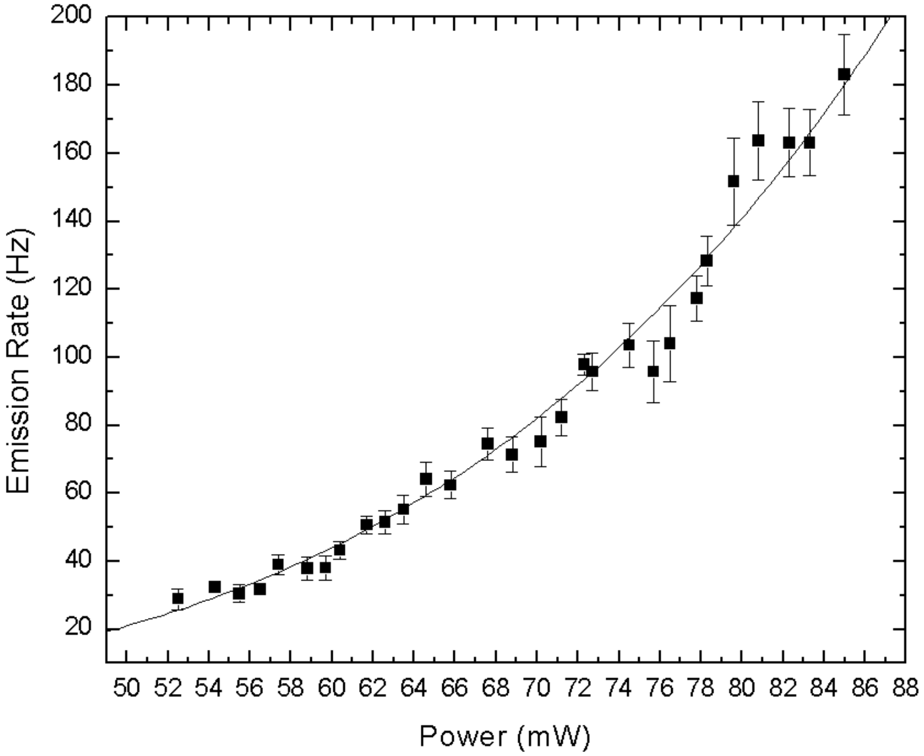

Figure 3.4. Emission rate as a function of laser power. A best fit of the form $R = A*P^N$, with $N = 4.15(7)$ and $A = 7.38(9) \times 10^{-6}$ is shown. The GaAs emitter for this data had a tip with radius of curvature on the order of 1 μm.

Investigations into possible causes of the changing value of N from trial to trial were conducted and found N to depend primarily on whether there were local laser hot spots (parts of the laser spot that are more intense than a Gaussian beam would be), overlap of the laser with crystal regions of differing sharpness (with the value of N being an average value for the N of each region), and slight changes in beam spot position from run to run. The value of N was also sample dependent, presumably because of differing tip sharpness, as has been observed previously with tungsten tips (17) due to field emission effects. The larger the bias voltage placed on these tips, the lower the value of N is so that at some voltage, the tip starts emitting without a laser present. So, while Fig. 1.2a shows a three-photon process, many different variables can slightly increase or decrease the number of photons needed for emission.

3.3 Sub-additivity in Electron Emission from GaAs

After establishing that it was possible to emit significant electron currents using multiphoton absorption, we decided to investigate whether the emission process of GaAs was fast or slow. To do this, an autocorrelator is used to split a single incident pulse from the oscillator into two temporally-separated pulses (Fig. 3.5). The laser pulses pass through an autocorrelator that splits the beam into two

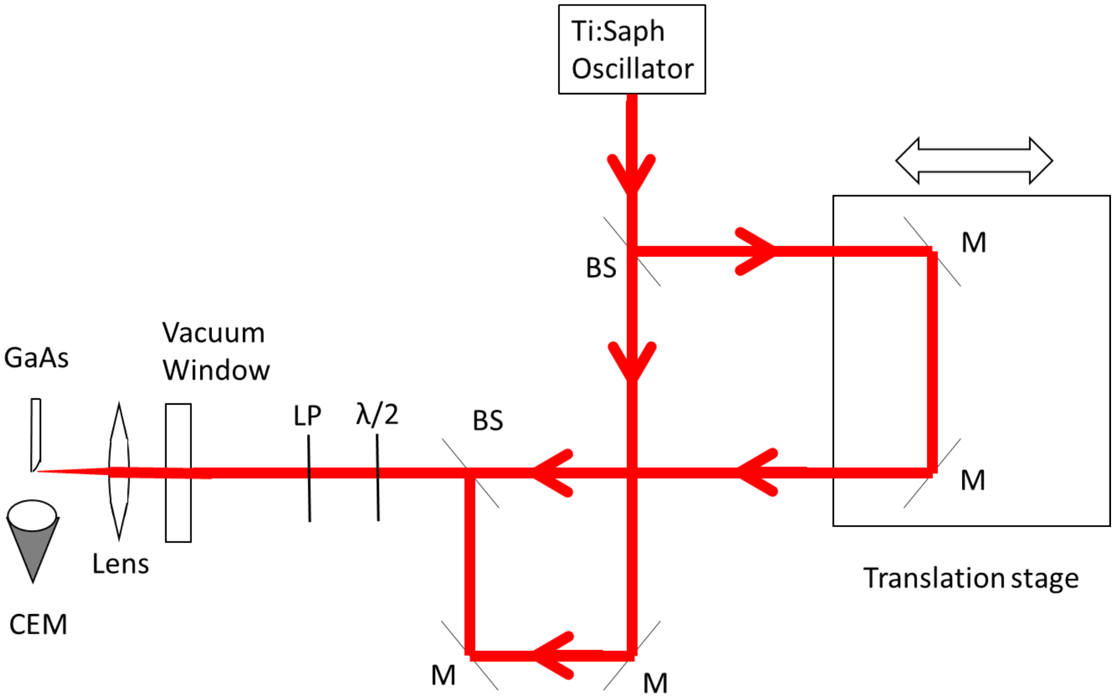

Figure 3.5. Optical setup with autocorrelator. A beamsplitter (BS) splits the beam into two that travel along different paths and are then recombined at a second BS. One path has a fixed length while the other has a variable length so that the delay between pulses can be varied. The autocorrelator allows for delays between the two beams of < 1 fs up to ~2.5 ns.

beams with equal average intensity of 50 to 100 mW. The two beams are then sent along different paths before they are recombined collinearly. One of the paths contains a piezoelectric translation stage, which allows us to make small (< 1 fs up to 70 fs with a resolution of 0.5 fs) adjustments to the delay, and a micrometer for larger (up to 300 ps) delays. The translation stage is mounted on a rail that can provide very large delays (> 1 ns). Both pulses were then overlapped spatially on the GaAs.

During these experiments, it became apparent that for time delays < 150 fs, the two beams together could emit more electrons than would be obtained from summing the output of the two individual pulses separated by long (> 1 ns) delays. This is due to the constructive interference between the two light pulses with the shape of the envelope being determined by the non-linearity of the emission process. When the pulses are overlapped temporally, their E-fields add vectorially. However, the emission is dependent upon the intensity, which is proportional to the square of the E-field, so doubling the E-field causes a quadrupling of the intensity. Since the emission depends nonlinearly (with an exponent greater than one) on intensity, if, for example, the intensity doubles, the emission rate more than doubles. This nonlinearity is due to the multiphoton absorption needed to emit an electron as discussed earlier.

For delays greater than 0.2 ps and less than 1 ns, however, it was observed that the two pulses combined produced fewer electrons than the sum of the emissions from each beam individually. We refer to this phenomenon as "sub-additivity" and show, as a central result of the work reported here, that it indicates the emission process to be fast, i.e. comparable to the laser pulse duration. It will also be shown that sub-additivity is caused by the electrons interacting with the conduction band of GaAs. Earlier experiments, using scanning tunneling microscope (STM) tips to monitor photo-induced currents, have measured a decrease in the photo-induced current in GaAs (42) (43), but no further investigations were conducted to analyze that discovery. They found that the photo-induced current was sub-additive when two temporally-delayed pulses of equal power were incident on the GaAs. A similar effect has also been seen in silicon (44), where they used a pump beam that wouldn't emit electrons by itself in conjunction with a probe that was of sufficient energy and intensity to emit electrons. They saw that when the pump beam was on, there was a decrease in probe-induced electron emission.

3.3.1. Experimental Procedures

As stated before, the GaAs sample was mounted on a three-dimensional translation stage so that we could move it into and out of the focus. How close a sample is to the focus can be determined by looking at the beam after it traverses the chamber and exits through another window. The GaAs tip will partially block the beam, and how close it is to the focus can be determined by the shadow that it casts in the beam spot (Fig 3.6a-d). When in the focus, interference fringes caused by the crystal can be seen (Fig. 3.6e, f). The lens we used could focus the laser down to approximately a 100 μm diameter spot size. Using the equation $r = \frac{4\lambda f}{\pi D}$, where λ is the wavelength of the laser, f is the focal length of the lens, and D is the diameter of the beam, we can calculate the diffraction limit of the laser for our lens. Using a focal length of 5 cm for the lens and a beam diameter of 1 mm, we calculate a diffraction limit for the beam of r = 48 μm, so our beam was very near the diffraction limit for this lens. Electrons could then be collected in the CEM adjacent to the sample (Fig. 3.5).

Asymmetry measurements involved having both beams hit the target and counting electrons for one to ten seconds depending on the desired statistical uncertainty. Then, the first beam was blocked, and electrons emitted by the second beam were counted for the same amount of time. Lastly, data was taken with the second beam blocked and the first unblocked. This process was repeated five times for each delay. Background count rates were checked on the first and last cycle by blocking both beams. To minimize the effect of long-term drift in the count rates, a computer switched between these laser pulse configurations after each electron counting interval. This was accomplished by two stepper motors with beam blocks

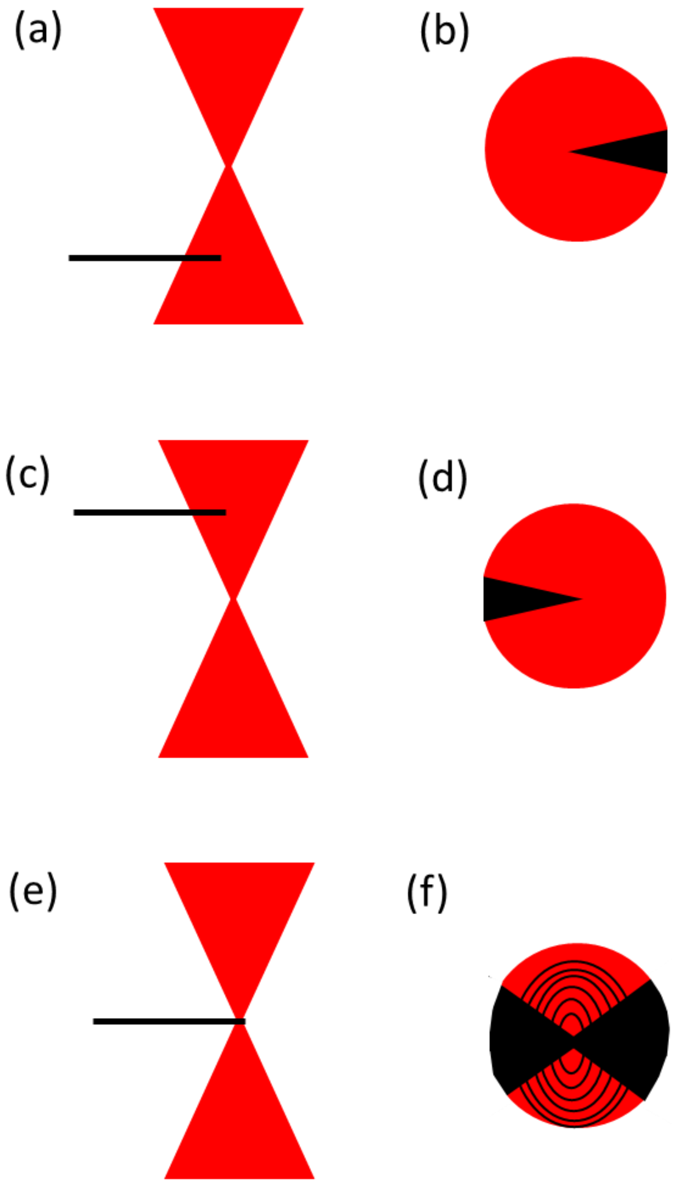

Figure 3.6. Images for determining sample position in a focused laser using the shadow of the sample. The left column shows a side view of the sample (black) in the beam path (red). The right column shows the laser and shadow at a screen after the beam has been focused (see text).

attached to them that could be rotated in and out of the two beam paths in the autocorrelator.

When we saw this sub-additivity in our results, a second experimental setup in a different lab was used to run multiple investigations into the cause of the sub-additivity. This second setup consisted of a similar Ti: Sapphire laser (45), that had virtually identical beam specifications to our laser including repetition rate, pulse duration, and beam power. In this setup, an 800 nm CW laser was made collinear with the pulsed laser before entering the chamber (See Fig. 3.7). Inside the chamber was an off-axis parabolic mirror that would focus the laser down to a 5 μm spot size. The focal length of this mirror was much shorter than for our lens, so we were able to obtain a much tighter focal spot for the laser. The emitted electrons were also collected in a CEM and counted.

3.3.2. Results

The emission behavior can be characterized with an asymmetry parameter A. The number of detected photoemitted electrons would vary due to changes in laser power or slight changes in the position of the laser beam spot from day to day on the GaAs crystal. For this reason, A is an intensity-normalized quantity:

$$A \equiv \frac{R_B - R_1 - R_2}{R_1 + R_2}, \tag{3.7}$$

where R_B, R_1, and R_2 are the rates at which electrons are detected when both laser

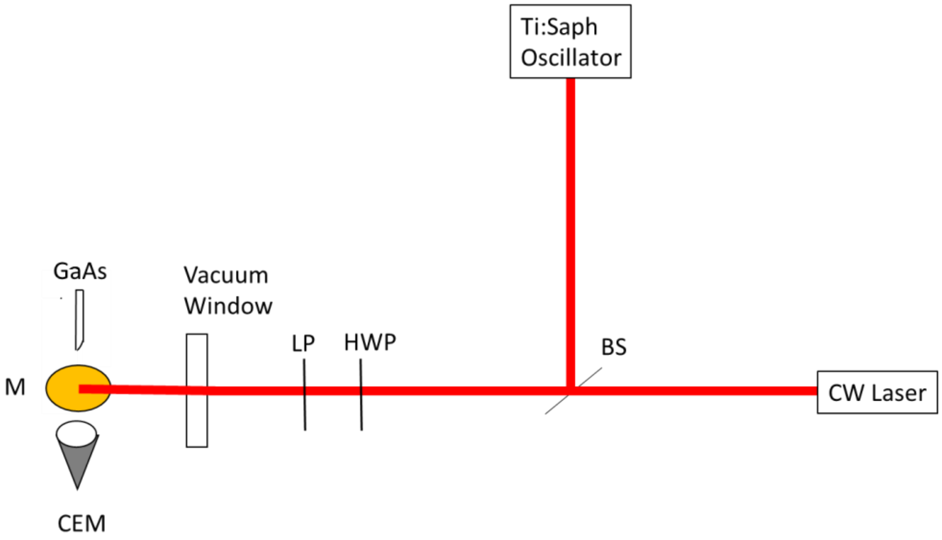

Figure 3.7. Secondary setup to investigate sub-additivity in GaAs. An 800 nm CW laser is combined collinearly with the pulsed laser using a beam splitter (BS). The beams are then sent through a half-wave plate (HWP) and a linear polarizer (LP) before entering the chamber. An off-axis parabolic mirror (M) reflects and focuses the beam upward to focus on the GaAs sample.

beams, only the first beam, and only the second beam, respectively, are incident on the crystal.

The delay between the two pulses varied from about -30 fs (corresponding to a reversal of which pulse comes first) to 900 ps. Fig. 3.8 shows *A* for small (< 100 fs) delays for which the two beams are largely overlapped in time. In this case, a rapidly oscillating electron count rate is observed corresponding to alternating constructive and destructive interference as the delay between pulses changes. When the beams destructively interfere, the rates drop to nearly zero and *A* approaches -1. For constructive interference, *A* becomes very large because the electron emission process requires an absorption of multiple photons to escape. As stated, the emission rate is proportional to I^N, which yields super-additivity at time delays where the two pulses constructively interfere. The data of Fig. 3.8 seems consistent with N = 3, since maximum constructive interference when the beams are temporally and spatially overlapped doubles the electric field amplitude, which quadruples the intensity. Assuming that the electron emission rate is proportional to I^3, that the separate beams have equal average power, and using eqn. 3.7, we obtain a maximum theoretical value for *A* of 31. As we increase the delay between pulses, they are no longer temporally overlapped, so the interference ceases and *A* approaches zero. This was expected and tells us nothing about the speed of the process, merely that the emission process is nonlinear. The

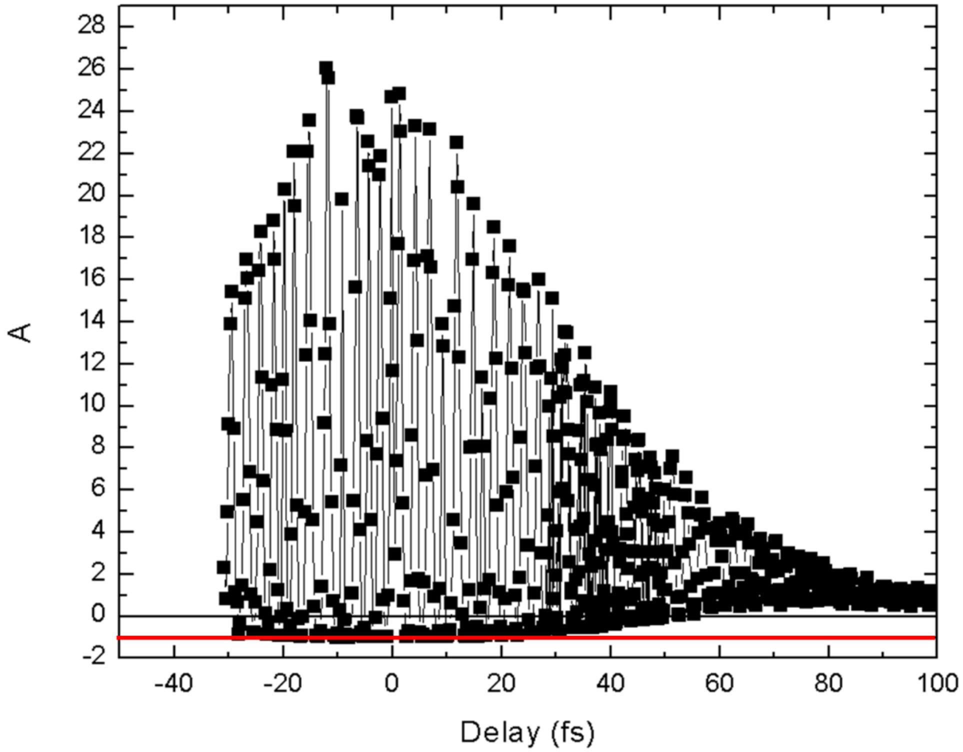

Figure 3.8. Data for A at relatively short delays when the incident beams are overlapped in time. The value of A, within counting statistics, is symmetric about the zero-delay point. The red line shown at A = -1 indicates total destructive interference between the two beams (eq. 3.7).

shape of this portion of the graph doesn't show us the speed of the emission since our detectors don't detect any temporal characteristics of the emission, just the total emission, so whether the process is slow or fast, the emission would have this periodic increase and decrease solely due to the constructive and destructive interference between the two beams.

It was expected that A would reach zero after the beams were no longer temporally overlapped and would remain zero for all delays larger than approximately 200 fs. As can be seen in Fig. 3.9, this is not the case. The value of A decreases below zero and remains there until about 1 ns. Another measurement was done using the translational stage's mechanical rail to obtain a delay of approximately 2.5 ns and yielded $A = -0.01 \pm 0.02$. So, it appears that once A increases to 0, it remains there.

As this was an unexpected result and there was very little literature on anything similar, we conducted several experiments to attempt to manipulate the sub-additivity and try to find the cause of it. Using the setup in Fig. 3.7, we alternated between having a CW laser collinear with a pulsed laser incident on the GaAs and just the pulsed beam. The pulsed beam was always incident on the crystal. Now consider

$$A_{CW} = \frac{R_{On} - R_{Off}}{R_{Off}}, \tag{3.8}$$

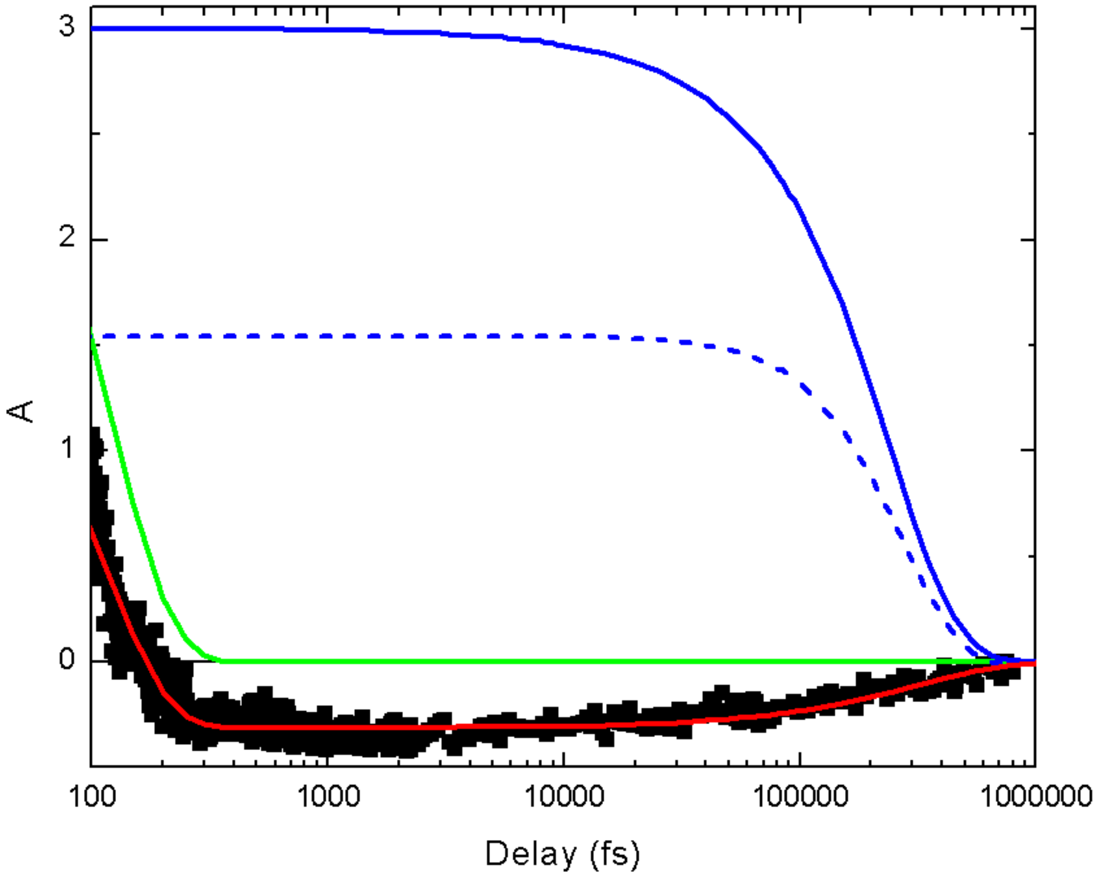

Figure 3.9. Data for A at long delays. Black squares indicate sub-additivity measurements for long delays. At about 200 fs, the value of A drops below zero, and continues to drop until approximately 2 ps. It then slowly increases until it reaches zero at ~900 ps. This is approximately the GaAs electron-hole recombination lifetime. Blue solid line denotes our model results for a slow emission process with no excited state, blue dashed line denotes a slow emission process with an excited state, green denotes a fast emission with no excited state, and red denotes a fast emission with an inhibition due to a conduction band population (see text).

where R_{On} and R_{Off} are the detected rates with the CW beam on and off respectively. As the intensity of the CW beam was not high enough to cause electron emission by itself, and it had a wavelength of 800 nm, the only effect it had was to excite electrons in the GaAs to the conduction band.

As can be seen in Fig. 3.10, A_{cw} depends linearly on the power of the CW laser as we vary its power from 0 to almost 50 mW. This implies that the sub-additivity depends linearly on conduction band population, since excitation from the valence band to the conduction band by the CW laser must be a one-photon process.

Using the setup in Fig. 3.5, the average power of the two pulsed beams was varied from 10 to 36 mW to see how A changed. To do this, the half-wave plate upstream of the linear polarizer was rotated, which kept the polarization on target constant while the incident power changed. The delay was fixed at 200 fs since that is approximately where A crosses from positive to negative values (Fig. 3.9). Fig. 3.11 shows that as the power decreases, and hence fewer electrons are excited to the conduction band by the first pulse, A can switch signs and achieve positive values.

Since it appeared that sub-additivity was dependent upon the population in the excited state, a final experiment checked for sub-additivity in a material

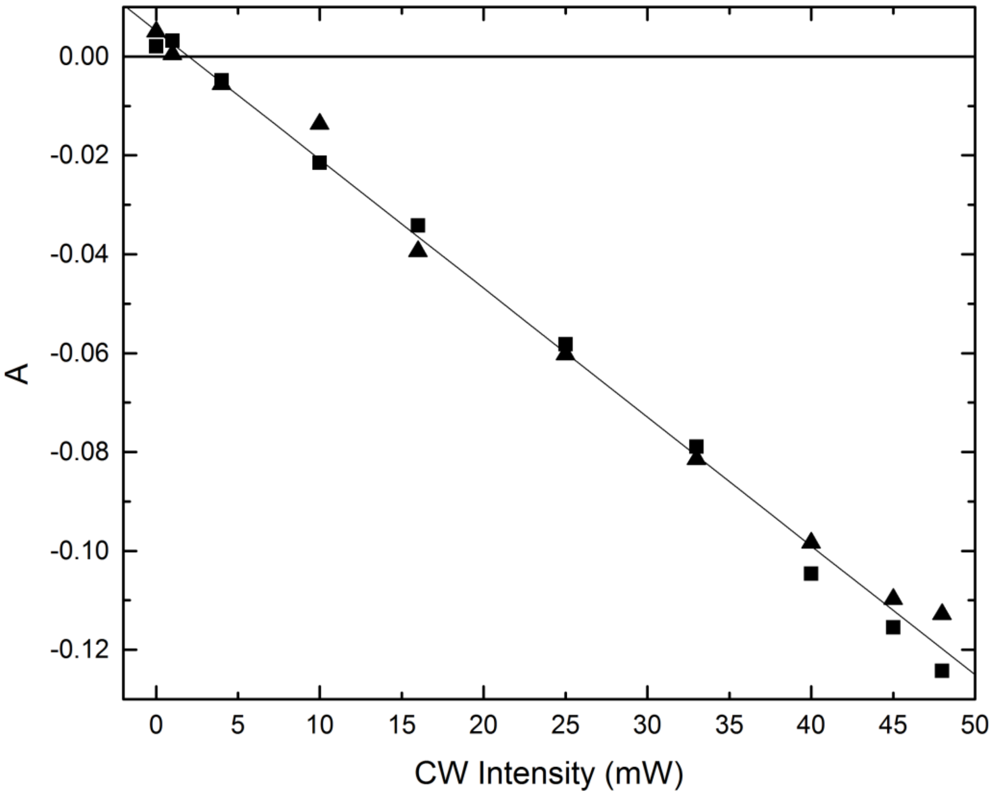

Figure 3.10. Asymmetry, A_{cw}, vs. CW laser power. Triangles and squares denote separate trials.

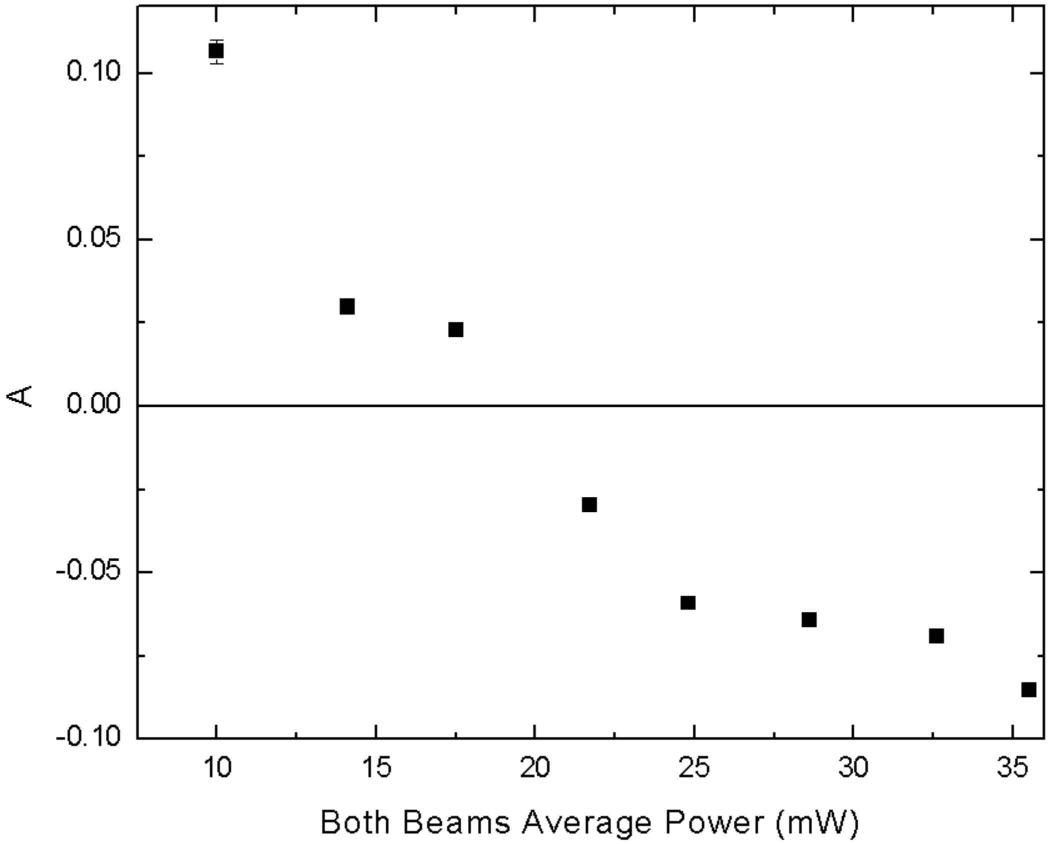

Figure 3.11. Asymmetry as a function of the summed average power when both pulsed beams are incident on the crystal. Data taken at a delay of 200 fs.

without a vacant conduction band. To do this, tungsten field emission tips (FETs) were used. Tungsten has a work function of 4.3 to 6.0 eV (depending upon which crystal orientation the tungsten has), which would mean that it needs 3 or 4 photons at 800 nm to emit an electron through a multiphoton process. This makes it similar to GaAs in this regard, which has a work function of 5.57 eV. A typical FET is shown in Fig. 3.12. Several other experiments have been done to characterize the emission behavior of W FETs (16) (17). Although the W tips in these experiments were much sharper than our GaAs samples (with the W tips having radii of curvature of order 10 nm and our GaAs tips being 20 times that or more), none of our results or those referenced showed any evidence of sub-additivity at any value of pulse-to-pulse delay up to 20 ps. In our experiments, several different positions of the laser focal point were checked on various parts of the W tip.

When we used a 5 μm focal spot size with GaAs tips, it was found that the sub-additivity effect goes away with the focus at the very end of the tip. If the focus was moved several microns back from the tip toward the bulk however, the sub-additivity returns. It is speculated that this is due to the changing nature of the band structure of the GaAs near a tip, as compared with that of the bulk.

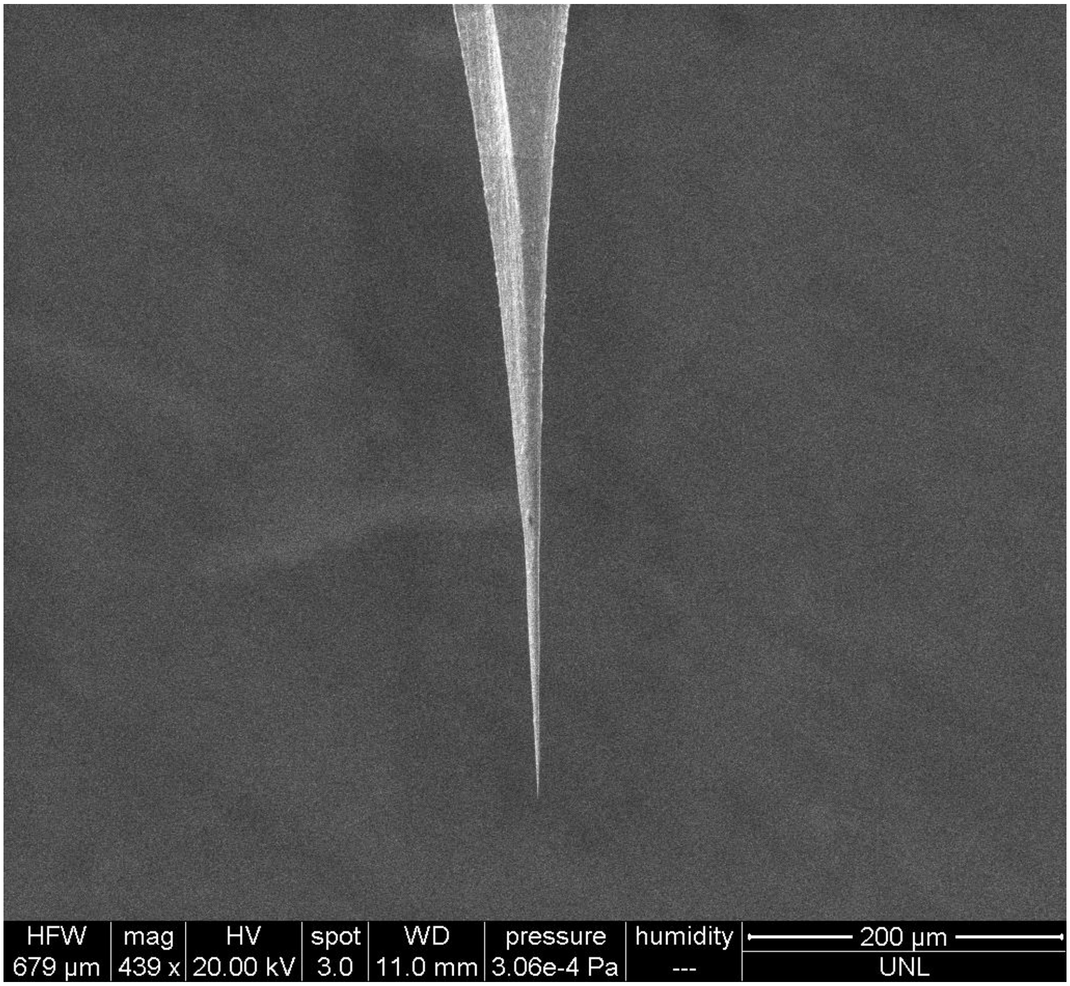

Figure 3.12. A typical field emission tip made by chemically etching a tungsten wire. Typical radii of curvature are between 10 and 100 nm. SEM image obtained from the Batelaan group at UNL.

3.3.3. Fast Emission

We now consider a mathematical description of the emission process to determine its time scale and to model the sub-additive nature of the emission process for two delayed laser pulses. When discussing the "speed" associated with laser-pulse-induced electron emission, there are two time scales to consider. The first is the delay between when the laser pulse hits the material and when electrons begin to emerge from its surface. This we refer to as the "promptness" of the emission. The second time scale, which indicates how "fast" the emission is, refers to the duration of the emission from the surface, compared with the limiting case of the laser pulse's temporal width. (It is assumed, barring an extremely non-linear response of the emission mechanism to the laser's instantaneous intensity, that the duration of the electron emission cannot be significantly shorter than that of the laser pulse itself.) Thus, an electron emission process could be fast but not prompt, and *vice versa*, although fastness and promptness generally go hand in hand since the less prompt the electron pulse is, the more it tends to spread out.

A central claim of this work is that our observation of sub-additivity shows that the emission of the electrons is fast. To support this idea, a description of the emission from GaAs that is dependent upon the speed of the emission process is considered, and we show how it would depend on the population of the conduction band. The model allows the adjustment of a "fastness" parameter to determine if the emission is slow (e.g. thermal), or fast. A graphical representation of electron emission caused by different emission processes is seen in Fig. 3.13.

Consider two transform-limited (temporally Gaussian with FWHM σ) equal-intensity laser pulses, the first having its maximum intensity occur at t = 0 s, and with delay-time d (Fig. 3.13a). The electron emission due to a single laser pulse is assumed to be described by a combination of another Gaussian of width B and a Heaviside function, H, both centered at a time f, corresponding to the promptness of the emission. The Heaviside function is added to the description to allow for the electron emission process to be temporally asymmetric due to, e.g., diffusion of excited electrons to the surface. We note that while B and f might be reasonably expected to be correlated with each other, the results of our model will not be sensitive to f due to an integration over all time, so we leave it as an independent parameter. The convolution of the separate laser pulses with their respective electron emission "amplitudes" are given by

$$\xi_1(t) = \int_{-\infty}^{\infty} e^{-2\varphi^2/\sigma^2} H(\varphi) e^{-(t-\varphi-f)^2/(B)^2}\, d\varphi \tag{3.9}$$

and

$$\xi_2(t) = \int_{-\infty}^{\infty} e^{-2(\varphi-d)^2/\sigma^2} H(\varphi-d) e^{-(t-\varphi-d-f)^2/(B)^2}\, d\varphi. \tag{3.10}$$

By taking either $\xi_1(t)$ or $\xi_2(t)$ and raising it to the third power (since our data in Fig. 3.8 implied N=3 for this set), then integrating them over time, a value

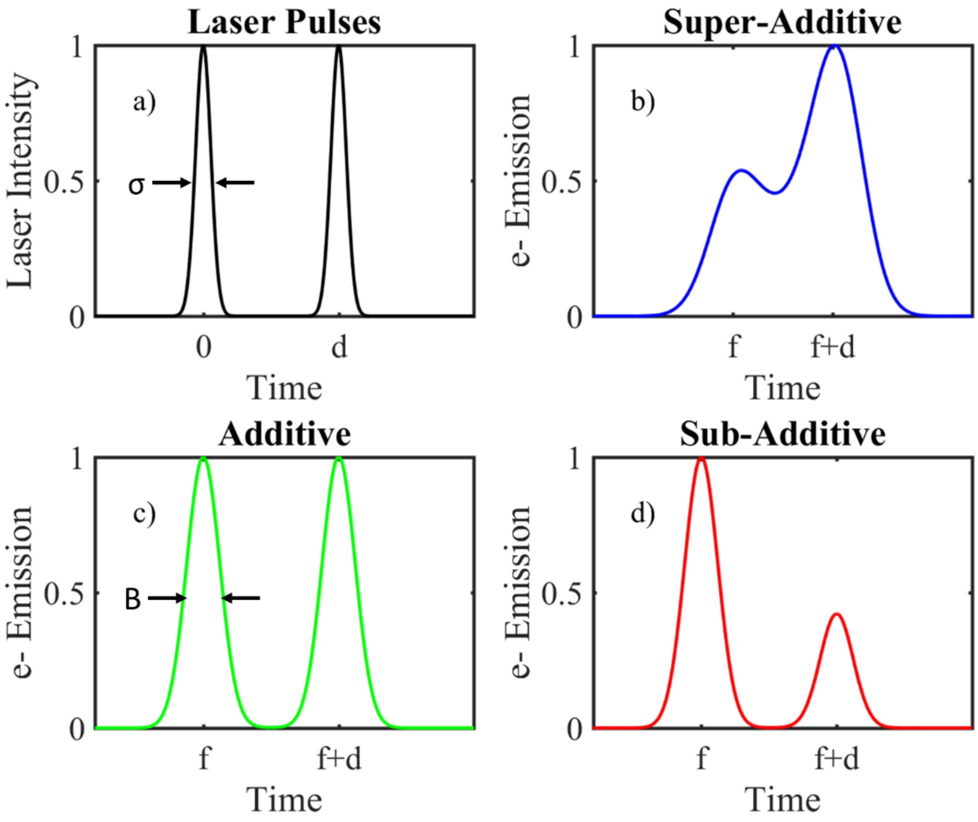

Figure 3.13. Comparison of different types of additivity. a) An example of the two laser pulses as a function of time, and what the electron emission would look like for b) super-additivity of a slow process, c) additivity of a fast process, and d) sub-additivity of a fast process. Colors coincide with the models in Fig. 3.9. Parameters corresponding to the discussion in the text are shown.

proportional to the emission of that pulse is found.

To get the emission for both pulses, a model with a mechanism to cause a decrease in emission of the second pulse is used. This emission should depend on parameters associated with the excited state, since we have seen (Fig. 3.10) that electrons in the excited state cause this subadditivity. We consider a "suppression" factor

$$g \equiv 1 - \alpha e^{-d/\tau}, \tag{3.11}$$

where α is a measure of the degree to which the population of the excited state diminishes the emission of the second pulse and τ is the lifetime of the conduction band against decay by recombination. We choose to define g this way so that α is a constant and the explicit dependence upon the delay between the beams is taken care of by the exponential term. Thus, the total emission is proportional to a quantity E(t) when both pulses are incident on the GaAs, where

$$E(t) = \int_{-\infty}^{\infty} (\xi_1(t) + g\,\xi_2(t))^3 dt. \tag{3.12}$$

If the emission process is fast, the cross terms of Eqn. 3.12 will be zero and what remains is the individual emission amplitudes each raised to the third power. If the process is slow, the cross terms will be non-zero and will account for the long-lasting interactions between the two pulses.

Examples of several mathematical models that consider qualitatively different emission physics are shown in Fig. 3.9. The first model (blue line) shows an emission process that is slow and with no excited state ($\alpha = 0$). We set B = 750 ps which would be comparable to a thermal process or some other type of slow emission process. As can be seen, the value of A is greater than zero for all values. Using eqn. 3.7 and eqn. 3.12, the model fits the expected value for g = 0. Since both $\xi_i = 1$, eqn. 3.1 becomes $((1+1)^3-(1+1))/(1+1) = 3$ until the pulses are separated by enough time that even a slow process ends before the second pulse arrives. Another model (green line) shows a fast emission process (B = 300 fs), with no involvement of an excited state. We see that A decreases to 0 and stays there for all larger delays.

The best fit to the data (red line) is obtained with B = 300(50) fs and the involvement of an excited state having a lifetime of τ = 250(100) ps and a "diminishment" constant $\alpha = 0.28(3)$. Finally, we consider a slow process (yellow line) with B = 750 ps, but this time taking into account the excited state (τ = 250 ps, $\alpha = 0.28$). The value for A is also always positive, but less positive than when $\alpha = 0$.

The fitting parameters we obtain that best reproduce the data and its sub-additivity indicate that (a) the emission process is fast, (b) it is crucially dependent on the existence of a transient excited state, and (c) the presence of electrons in the excited state must act to inhibit emission caused by the second laser pulse. The lifetime of the excited state depends on the dopant concentration of the GaAs (46). The larger the dopant concentration, the shorter the lifetime. Our dopant concentration is 2 x 10^{19} cm^{-3}, so a conservative estimate for the maximum lifetime of the excited state is 370 ps (as this is the lifetime for a 1.6 x 10^{19} cm^{-3} concentration given in (46)). For a first-order approximation of the emission process, the model matches well.

3.3.4. Possible Mechanism

One possible explanation for the non-zero diminishment factor, α, that leads to the sub-additivity observed is exciton screening (47). In this model, the excited electron-hole pairs form a plasma with a plasma frequency, ω_p, that screens valence-band electrons with low kinetic energy from being excited by the electromagnetic pulse. When the first pulse hits the GaAs, electrons are emitted. However, some electrons only absorb one photon and are excited to the conduction band. These electrons create a plasma with a plasma frequency (47)

$$\omega_p = \sqrt{\frac{ne^2}{m^*\varepsilon_o}}, \tag{3.13}$$

where n is the density of electrons and m* is their effective mass in the conduction band. To calculate the density of excited electrons, the density of valence electrons in the ground state was multiplied by the probability, P, of exciting those electrons with a laser pulse. To calculate P, we used eq. (2.3) from (40):

$$P = 1 - e^{-\sigma\tau' I}, \tag{3.14}$$

where σ is the excitational cross-sectional area of GaAs, I is the intensity of the laser pulse, and τ' is the FWHM of the pulse. For the intensity, the typical average power of our laser of 65 mW and a beam focal spot radius of 50 microns was used. The FWHM was 75 fs and σ was calculated to be 3.8×10^{-23} m^2 for our laser wavelength. This yields $P = 1.18 \times 10^{-5}$. In GaAs, there are three electrons in the valence band per As atom and one per Ga atom. Since GaAs has a diamond crystalline structure, there are 4 of each atom per unit cell of the crystal. This gives 16 valence electrons per unit cell. From this and eqns. 3.13 and 3.14, the density of excited electrons calculated is 1.055×10^{24} e$^-$/m^3, yielding $\omega_P = 2.308 \times 10^{14}$ Hz. Since the band gap of GaAs is 1.42 eV, this corresponds to an electron needing to absorb a photon with an energy of 1.572 eV or more in order to not be screened. This plasma frequency would cause screening of electrons that absorb a photon of wavelengths greater than 788 nm. This is close to the center wavelength of our laser pulse, so our *ansatz* is plausible.

We initially thought that the sub-additivity we observed was caused by an increase in GaAs surface reflectivity, R, induced by the first laser pulse. An experiment was set up to have a lens focus the pulsed laser onto a rectangular piece of GaAs on a translation stage, to be able to finely adjust its position in the focus. The GaAs was at an angle so that the specularly-reflected light could be sent into a photodiode. We looked at various delays between laser pulses and calculated the change in reflectivity for those delays. The reflectivity change, $\Delta R/R$, was measured to be 0.013 ± 0.013 and $-.011 \pm .018$ for the delays with the best overlap (i.e. the largest amount of destructive interference when looked at on a photodetector). Other studies of this type have been done, using lasers similar to ours (48), which measure the pulse-to-pulse reflectivity change of GaAs. They found that $\Delta R/R_0 \approx 1.2 \times 10^{-4}$ for delays above 250 fs through several picoseconds. So, our results were both consistent with zero and with the non-zero results others had seen, which means our error is too large and the value is too small for us to accurately measure. However, using our equations, this change in reflectivity is not enough to significantly change our value for A.

The exciton screening model would predict that there is less absorption of the second laser pulse, and would thus correspond to an increase in the bulk transmissivity, T. Our GaAs samples are too thick to measure this directly, which means that the laser is just being absorbed deeper in the crystal where the electrons are not able to be emitted before being recaptured by the crystal lattice. Thus, the screening model may actually cause emission inhibition both by direct screening and through increasing the average depth in the GaAs at which electrons are produced.

3.3.5. Preliminary Experiment Conclusions

NEA GaAs can be used to produce photoemitted spin-polarized electrons when it is illuminated by CW circularly-polarized light with ~800 nm wavelength (9) (10) as we have discussed. This is due to the differences in excitation probabilities to the excited state sublevels. It has been shown in these experiments that the emission process is affected by an interaction between the laser pulse and electrons in the conduction band. This means that even in a multiphoton emission process, it is not unreasonable to expect that the resonant interaction of this state with the photoemitted electrons may yield some degree of spin polarization up to the theoretical limit of 50% for bulk GaAs (9).

It has also been shown that the sub-additivity found is evidence of electrons being excited to the conduction band in the photoemission process. Our heuristic model implies that the emission is fast, on a timescale of less than 300 fs. Next, we will discuss electron polarization measurements, made in the hope of demonstrating a fast source of spin polarized electrons.

To summarize our results to this point, the sub-additivity that we observe, described well in our model, may be qualitatively understood in terms of an exciton screening picture, which yields much larger changes in valence band excitation for the second of the two laser pulses than could be explained by reflectivity changes alone. According to our model, sub-additivity is now another way to determine that the emission from a material is fast, just as a material with a value of A reaching zero quickly has been shown to indicate a fast process. We note that the sub-additivity effect is apparently much more pronounced than the pulse-to-pulse optical changes in R or T observed by previous investigators (47). As such, photoemission sub-additivity may be able to serve as a very sensitive probe of electron dynamics in semiconductors in the future.

3.4. GaAs Polarization Measurements

Since we now know that there is an interaction with the conduction band when GaAs electrons absorb multiple photons, and using the full setup shown in Fig. 2.1, we are able to make polarization measurements for the emitted electrons using sharp pieces of GaAs. We can position the sample so that we have either the tip in the focus, or an area behind the tip in the focus, which we refer to as the shank of the crystal. Fig. 3.14 shows approximately the two positions on the crystal tip that we investigated.

The data-taking procedure for each position was the same, so the only thing that needed to change between runs was the position of the crystal. Using eqns. 2.3 and 2.4 allows us to calculate a polarization for the detected electrons. To calculate an average polarization, we would run through each configuration of

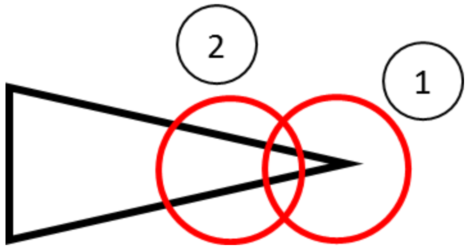

Figure 3.14. Laser positions on GaAs. Approximate positions of the laser focus on the shard when measuring the polarization of electrons emitted from the tip (1) and the shank (2) of the GaAs. The laser spot size is approximately 20 μm.

laser polarization (right-handed circularly-polarized (RHCP), left-handed circularly-polarized (LHCP), horizontal linearly-polarized (LP), and vertical LP light), counting for ten seconds in each configuration. We would repeat that for as many cycles as we desired running a background check every ten cycles by blocking the beam, so that no laser induced emission occurred. Once the data set was complete, we would calculate a value for polarization for each cycle of data and then use each of those polarization values to calculate an error-weighted average of the polarization. We would then repeat this but switch the order of the laser polarization while still calculating the polarization in the same way. This should give the same magnitude of polarization but with the opposite sign. We then take an error weighted average of the absolute value of these two polarization values to report the polarization of that sample.

When we first started taking polarization data, we put a -80 V bias on the GaAs by using a battery box attached to an ammeter thinking that we would be able to simultaneously measure the emitted sample current and count rate detected by the CEMs of the Mott polarimeter. Unfortunately, this caused our polarization data to fluctuate significantly from data set to data set. Fig. 3.15 shows a sample of data for several consecutive runs. The error bars show the statistical uncertainty merely due to counting statistics, but the fact that the data jumps around at factors many times this statistical uncertainty shows that there is

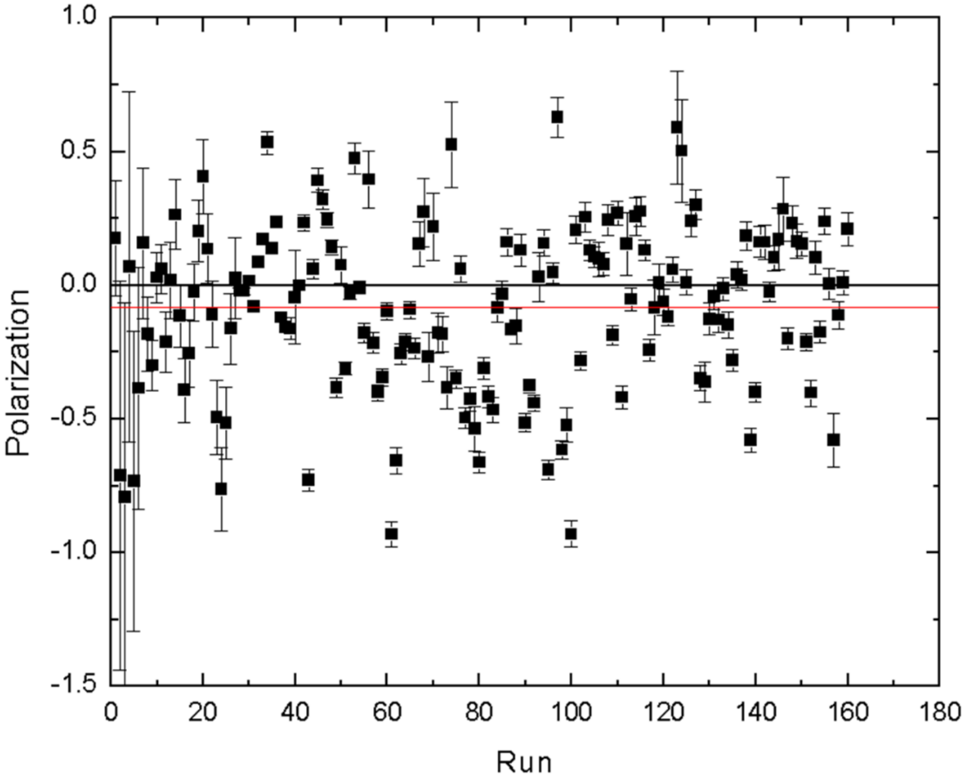

Fig. 3.15. A sample data set for many consecutive runs. The polarization calculations fluctuate wildly. Error bars shown are purely statistical error due to counting statistics. The time required for each run was 1 minute. The time required for all 160 runs was almost 3 hours. The average (red line) of all 160 runs is -0.08 with a standard deviation of the mean of 0.03 and a reduced χ^2 of 40.7.

something else contributing to the error. This indicated there was either something wrong with the system, or something wrong with the computer program taking the data.

After trying many different things, we discovered that it was the crystal bias that caused this behavior, either due to the ammeter or battery box itself. Whatever the reason, we switched the bias to a conventional power supply and the fluctuations ceased. Fig. 3.16 shows a typical sample set after switching to the power supply.

As can be seen from the data in Fig. 3.16, it appears as if the size of the statistical error doesn't impact the distribution of the data points since the runs with larger errors are similarly distributed to those with the smallest errors. For this reason, to calculate the error in our data, we would assume that all the data has approximately equal error and calculate the error needed in order for the reduced χ^2 to have a 50% probability of being either larger or smaller than the value used (49).

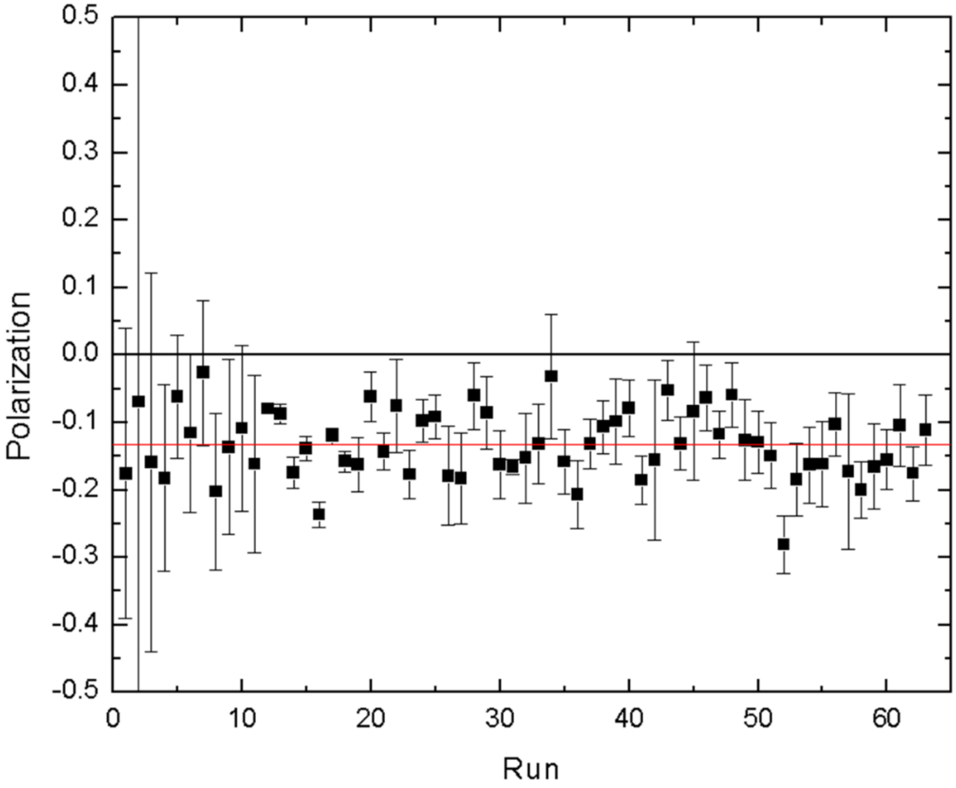

Fig. 3.16. Several consecutive sets of data after switching the bias on the crystal to a conventional power supply with sample 2 in the system. The average (red line) of all 63 runs is -.133 with a standard deviation of the mean of .006 and a reduced χ^2 of 2.5 (corresponding to a polarization of 13.3%).

3.4.1 GaAs Polarization Results

Table 3.1 shows the results for three separate samples of GaAs shards. When the tip is in the focus and circularly polarized light is used, we measure polarizations of ~13% for two of the samples and ~10% for the other. Linearly-polarized light yielded polarizations consistent with zero. When the laser was focused on the shank of the crystal, the polarization also drops to zero. Sample 1 broke before we could finish measurements, but we were able to take SEM images of samples 2 and 3 to see if there was anything structurally that could account for a difference in polarizations. Looking at Fig. 3.17, we see that on sample 2, there are several small "pointy" parts located in the laser focus. Sample 3 was much smoother. This seemed to imply that sharper features yielded a higher polarization of emitted electrons. This led us to use the GaAs wedges that will be discussed in Chapter 5.

It remains unclear if the difference in polarization between the tip and the shank is due to a change in the electronic structure of the crystal bulk or if it is due to electrons emitted from the shank traveling through more material before being emitted from the tip and thus becoming depolarized through interactions within the material.

We have established (as shown earlier) that by using an autocorrelator, the

GaAs Tip	**Incident Light Polarization**		
Sample 1		Polarization (%)	Dichroism (%)
	Circular	13.0(7.2)	
	Linear		
Sample 2		Polarization (%)	Dichroism (%)
	Circular	13.3(0.6)	4.7(0.3)
	Linear	0.2(0.4)	41.2(0.3)
Sample 3		Polarization (%)	Dichroism (%)
	Circular	9.9(4.3)	1.0(3.5)
	Linear	2.5(2.4)	18.2(5.6)
GaAs Shank			
Sample 1		Polarization (%)	Dichroism (%)
	Circular	1.2(1.6)	6.7(1.3)
	Linear	1.0(1.0)	23.7(3.7)
Sample 2		Polarization (%)	Dichroism (%)
	Circular	3.4(3.0)	
	Linear	5.2(4.9)	

Table 3.1 Polarization and dichroism results for circularly- and linearly-polarized light incident on either the tip or the shank of three different samples. The polarization column reports the measured polarization of the emitted electrons while the dichroism column reports the asymmetry of the total emission of electrons.

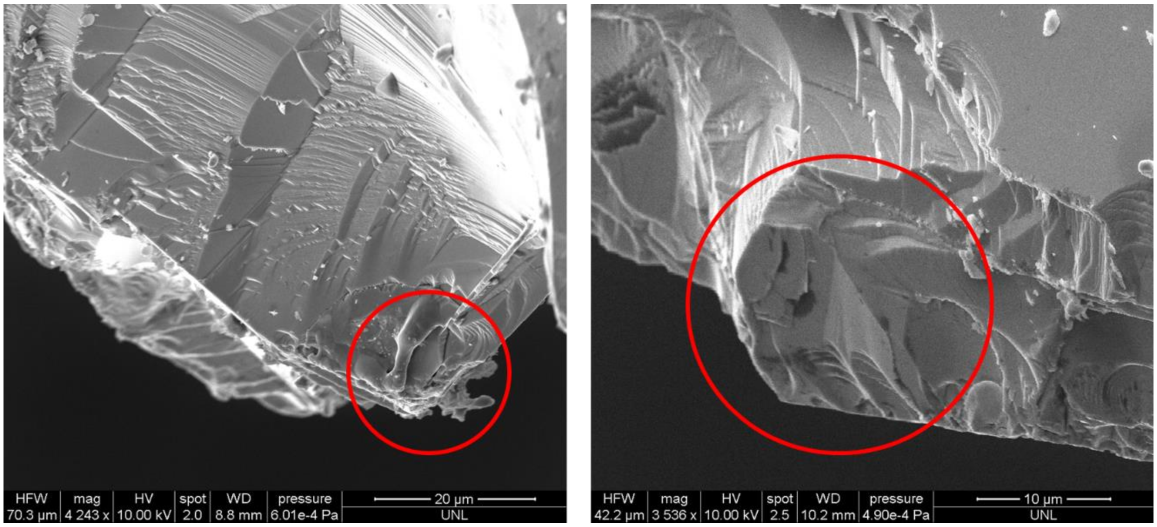

Figure 3.17 SEM images of GaAs samples 2 (left) and 3 (right). The red circles indicate approximate locations of the laser spot. The differences in sizes is due to different magnifications.

emission from the tip using delayed pulses results in sub-additivity when the pulses are more than 200 fs apart temporally. This means that by using GaAs tips, one can have a fast-pulsed source of spin-polarized electrons. This opens the door for fast, time-resolved, spin-dependent effect measurements.

3.5. Dichroism of GaAs Emission

In addition to the spin polarization of electrons emitted using circularly polarized light, we also checked to see if the orientation of linearly-polarized light relative to the sample geometry or the handedness of circularly-polarized light would have an effect on the number of the electrons emitted from the sample. Since it is well-known that the number of electrons emitted from a FET will change when switching the linear polarization from parallel to perpendicular to the tip (17), we checked to see if the same was true for GaAs. We used the CEM near the sample to monitor the emission rate from the crystal, and determine the value of the circular or linear dichroism, *D*:

$$D = \frac{R_1 - R_2}{R_1 + R_2}, \tag{3.15}$$

where $R_{1,2}$ indicates the count rates for left- and right-handed circularly polarized light when calculating the circular dichroism and indicates linear polarization parallel or perpendicular to the tip when calculating linear dichroism. The power of the LHCP and RHCP light are not measurably different. However, the linearly polarized light had slightly different powers depending on the direction of polarization. The horizontal polarization had ~3% less power than the vertical polarization. For the polarimetry data, this is irrelevant due to the method we use to calculate the polarization, but it does affect the total emission measurements and therefore must be accounted for when calculating a dichroism. In order to compare the data for the total emission, we had to normalize the emission to the power. Unfortunately, the emission is not linear in power, as we have discussed above. Using a typical value of N=3, we normalized the emission for the two different directions of linear polarization. This means that we can calculate linear dichroism based on the power difference of the two linear light polarizations using

$$D = \frac{R_V - x^N R_H}{R_V + x^N R_H}, \tag{3.16}$$

where $R_{V,H}$ is the emission rate for the vertical or horizontal directions and x is I_V/I_H, the ratio of the intensities of the two different LP directions that accounts for the non-linear emission increase with higher laser power. To check the effect that N has on the final calculation of the normalized linear dichroism, we looked at how it changed when we varied N for 3 to 6 (the lowest and highest values of N we have seen). The values reported in Table 3.1 use N = 3. There is a difference of about 3.5 percent for D calculated when N = 3 and N = 6 with the latter being larger. So, the difference is not negligible, but it doesn't change the final D-values significantly. As can be seen in the far-right column of Table 3.1, switching the direction of the circularly polarized light made very little difference in the total emission. This was to be expected as circularly polarized light can be thought of as two perpendicular directions of linearly polarized light that are out of phase. Also as expected, the linearly polarized light showed that more electrons are emitted when the linear polarization is parallel to the tip. The values of the linear dichroism shown mean that we emitted double the number of electrons or more when the linear polarization was aligned with the tip as opposed to perpendicular to the tip. This confirmed our assumptions that the GaAs tips are acting in a similar manner to the FETs that have been studied before.

While similar, FETs are generally much sharper than our GaAs was and for that reason, they obtain values for electron emission linear dichroism up to 90% when carefully aligned (17). This large value of dichroism is caused by the alignment of the electric field of the laser with the axis of the tip. When the electric field is parallel to the axis of the tip, electrons are much more easily emitted than when the electric field is perpendicular to the axis of the tip.

3.6 Comparison with Other Sources

Current state-of-the-art CW NEA GaAs polarized electron sources are able to a much higher of polarization than our source. A bulk GaAs source can achieve polarizations of up to 40% (9). Other sources also exist that utilize GaAs that has been grown on a strained lattice. This eliminates the light hole/heavy hole (m_j = ±1/2 and m_j = ±3/2 in Fig. 1.1 respectively) degeneracy and allows for an even larger asymmetry in the excitation to the excited states. These sources are able to produce > 80% polarized electron beams (50). The tradeoff is that the quantum efficiency of these sources drops significantly, meaning that the emission current for a given amount of laser power is much lower than that for the bulk GaAs sources. Our work appears to be the first demonstration of a source that can produce fast pulses of spin-polarized electrons that is based on GaAs without requiring NEA activation.

The best way to compare these sources is to use a "figure of merit"

$$\eta = P^2 I\,, \tag{3.17}$$

where P is the polarization and I is the current the source can produce. As with the figure of merit of a Mott polarimeter as described in Chapter 2, the figure of merit is inversely proportional to the square of the amount of time it takes to collect data to a desired statistical precision. Table 3.2 shows a summary of η for our source, a bulk NEA source, and a strained NEA source. As can be seen, our source currently has a significantly lower η, mostly due to the amount of current that we have obtained with it. We typically had up to 4 nA from the crystal whereas the other sources get around 100 μA. Maximizing the current was not the focus of this work but would be a very good next step so that this source becomes much more practicable as an actual source.

Source	**η (Amps)**
This work	7×10^{-11}
NEA Bulk (51)	6×10^{-5}
NEA Strained (50)	1×10^{-5}

Table 3.2. Comparison of the figure of merit, η, for the different GaAs sources of polarized electrons discussed in this work.

Chapter 4. Chiral Nanostructures

4.1 Introduction

The second type of target that we investigated were arrays of metallic chiral nanostructures grown on silicon substrates. These samples were grown by Eva Schubert's group in UNL's Department of Electrical and Computer Engineering. They have been investigating different optical properties of these materials, so collaboration with them was mutually beneficial since we could investigate some of the electron emission properties in parallel to their optical measurements. These structures were grown using a variation of the technique called glancing angle deposition (GLAD) as described in ref. (52). The GLAD technique uses an evaporative source of the material from which the nanostructures are to be made that is located below the substrate on which they are to be grown (Fig. 4.1). The normal of the substrate is angled at 85^0 to the normal of the evaporative source. The substrate can be rotated during the deposition. The rate and angle of rotation allow the user to choose the shape (pitch and diameter) of structure they want. Having no rotation creates angled rods on the substrate, while a steady constant rotation makes corkscrew-like structures (Fig. 4.2a, b).

The variation for our samples was to use the GLAD technique along with ion-beam-assisted deposition of the material (53). The ion beam is directed at the

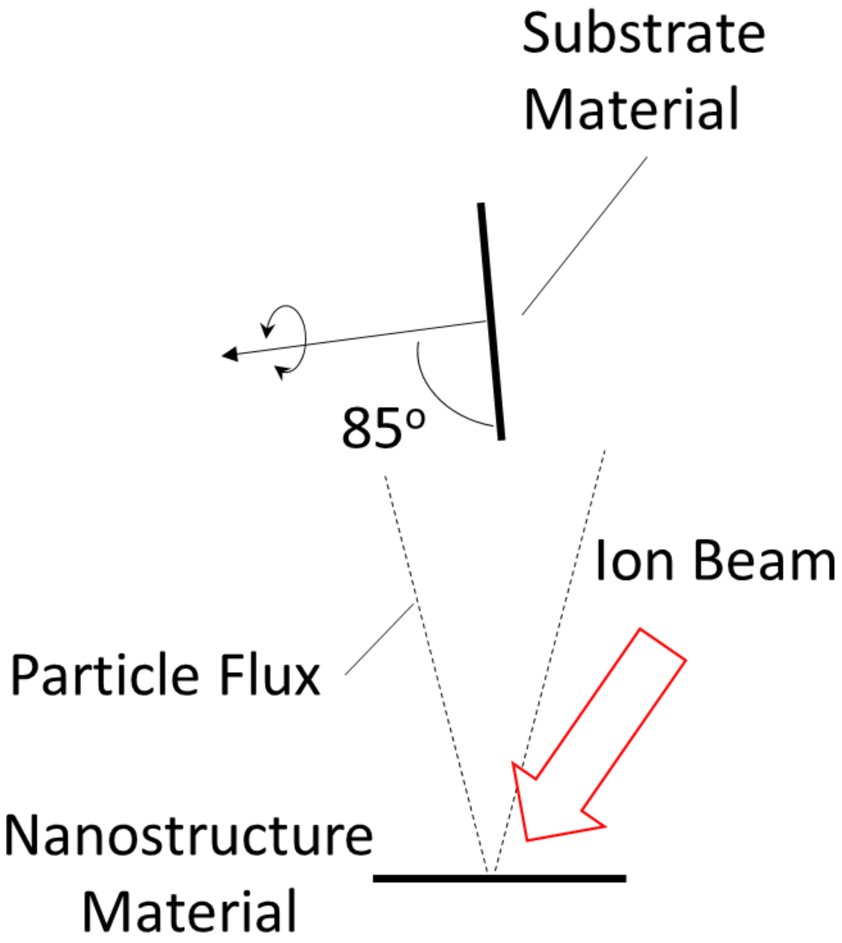

Figure 4.1. Schematic for glancing angle deposition (GLAD) with ion beam assistance. The substrate material can be rotated about the axis normal to its surface. The shape of the nanostructures is determined by the rate and angle of rotation of the substrate.

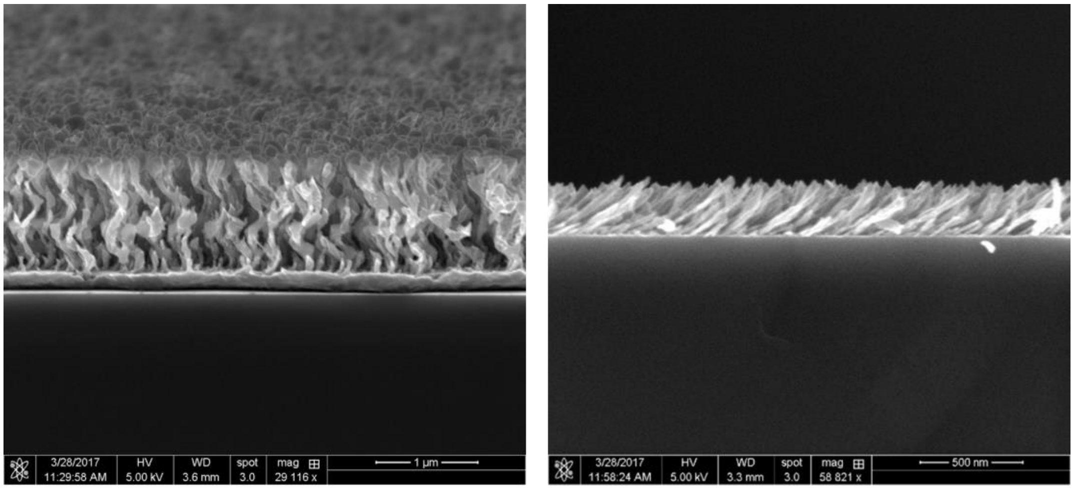

(a) (b)

Figure 4.2. SEM images of the GLAD Ti samples we used. (a) shows titanium stair-step nanostructures on a silicon substrate. Each structure is approximately 1 μm tall and they are very densely packed over the entire substrate with approximately 35 chiral structures per square micron. (b) shows anisotropic titanium columns that are tilted away from the normal of the substrate at an angle of ~50^0 .

evaporating material which allows for better control of the particles as they leave the evaporation area. Using the ion beam indirectly gives better control over the deposited material since ion beam sputtering is able to be performed at lower pressures. This reduces the amount of scattering that the sputtered material has with other particles in the chamber before hitting the substrate. So, any sputtered material that collects on the substrate follows a straight-line path instead of some of it coming from many different angles due to this spurious scattering. A second advantage for ion-beam-assisted deposition is that allows higher melting point materials to be used that are not accessible using the evaporation-deposition technique alone. The ion beam is at a high enough energy to sputter the target material when the ion hits it, so deposition isn't as dependent upon the material's melting point. This means you have the ability to use materials with melting temperatures that would otherwise be prohibitively high for your system.

Two different types of samples were created using this modified GLAD method. The "anisotropic" samples were grown by keeping the sample fixed, i.e. with no rotation throughout the growth, which causes the sample to grow into angled rods (Fig. 4.2b). They are approximately 400 nm long and at roughly a 50^0 angle from the normal. The chiral Ti structures are grown in a similar manner except that after the rods had grown approximately 125 nm, the sample was rotated by 90^0. At equal time intervals, the sample was rotated so that we obtained the stair-step spiral shape (Fig. 4.2a) that had two full turns so that each chiral structure is approximately 1 μm in height. Thus, each full rotation consists of four pieces of angled rod that is 90^0 rotated from the layer below it. From previous measurements taken on GaAs, we know that sharp features emit more electrons, so we chose this stair-step method thinking that it might increase our emission due to each layer having sharp "corners" at every position where we rotated the sample during growth.

4.2. Circular Reflection Dichroism in Chiral Ti Structures

As a preliminary experiment, we wanted to see if there was any sort of optical signature for a surface that could be used to determine if it was chiral. Attempts to study the optical signatures of these structures have been done using generalized ellipsometry and unpolarized scattering intensity measurements (54). To do this, they attempted to find 12 of the 16 elements of a 4 x 4 Mueller matrix that would satisfy $S_{emergent} = MS_{incident}$, where S is the stokes vector for either the incident or emergent light and M is a Mueller matrix associated with the specular reflection of the light. This was an arduous task and led us to attempt to find a simpler optical signature that could give us information about the surface chirality. We first attempted to make ellipsometry measurements using a null ellipsometer from the department's Advanced Instructional Laboratory with a mercury gas discharge lamp for a light source. We quickly realized that for the chiral Ti sample, there was not enough light reflected from the sample to obtain photocurrents significantly different from background on the ellipsometer's photomultiplier tube. For this reason, we switched to a laser-based setup shown in Fig. 4.3. We set up a HeNe CW laser (55), with output power up to 5 mW at 632 nm, that would pass through cleanup linear polarizers and quarter-wave plates in order to get circularly polarized light incident on the sample. The handedness of the circularly-polarized light could be changed by rotating the linear polarizer located between the two quarter-wave plates by 90^0. The sample was mounted on a rotatable mount and the optics post was also mounted on a rotation stage so that we could rotate both the angle of incidence of the laser, θ as shown in Fig. 4.3, as well as rotating by an azimuthal angle Φ about the axis normal to the sample surface.

Any time the angle of incidence was changed, the photodiode would be moved to collect the specularly-reflected light. Due to how we will calculate the dichroism, as explained next, the absolute magnitude of each beam's power is not essential, so we don't need to worry about the position on the detector of the laser when comparing different sets of data. The somewhat unorthodox optical setup is due to our lack of half-wave plates for 632 nm. We had to improvise how to clean up the beam's linear polarization before circularly polarizing the light. The first linear polarizer enables us to adjust the power of the beam while the second keeps

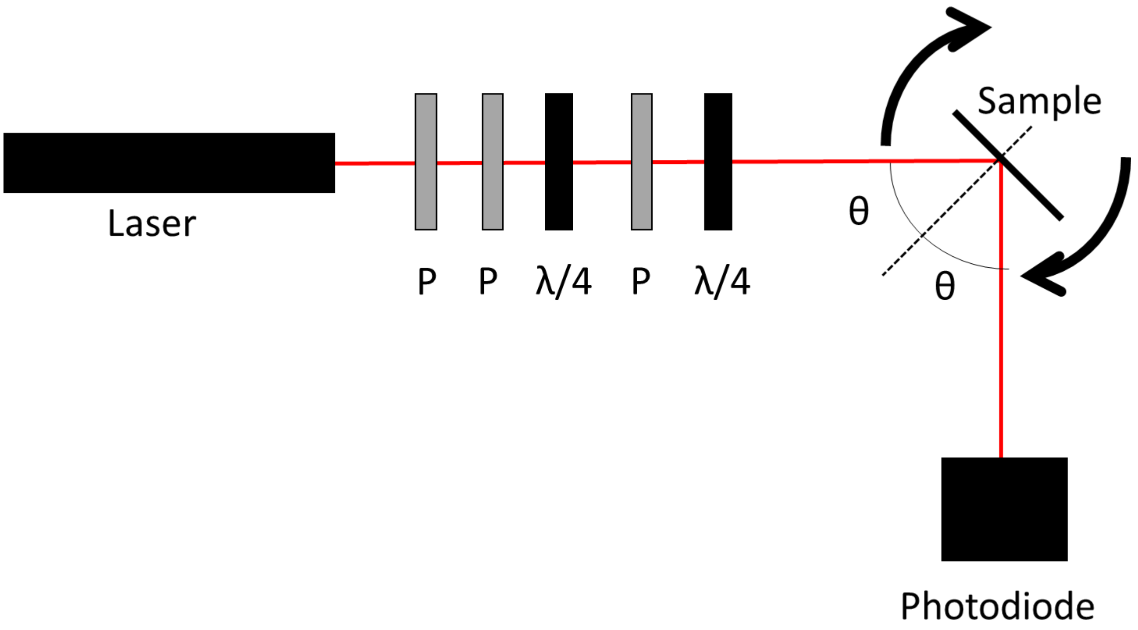

Figure 4.3. Schematic of our setup for measuring the amount of light reflected from a sample. The laser passes through linear polarizers (P) and quarter-wave plates ($\lambda/4$) to make it circularly polarized. The light then hits the sample and reflects into the photodiode. The somewhat unorthodox setup stems from a lack of half-wave plates at 632 nm. The first two polarizers allow us to vary the power of the beam by rotating the first polarizer while the second maintains a constant polarization heading toward the first $\lambda/4$ plate. The $\lambda/4$ plate circularly polarizes the light so the last P can be rotated without changing the power. The last $\lambda/4$ plate circularly polarizes the light. We rotate the last P by 90^0 to change the handedness of the light. The sample is on a rotatable mount so that the angle of incidence of the laser, θ, can be varied.

a constant polarization direction, then a quarter-wave plate circularly polarizes the light so that the position of the last linear polarizer doesn't significantly change the power of the laser. The last quarter-wave plate remained fixed and the linear polarizer before it was rotated by 90^0 to allowed us to switch between the two circular polarizations.

Despite these attempts at beam power control, the LHCP and RHCP light did not have the same power after passing through all the optics, so we first moved the photodiode to a position before the sample, but after the optics, to find the relative power of each beam and then used those measurements to normalize

the reflection data. Photodiode currents were measured for angles of incidence from 10^0 to 75^0. After normalizing the currents, we calculate the dichroism, *D*, of the surface using the equation

$$D = \frac{I_{RHC} - I_{LHC}}{I_{RHC} + I_{LHC}}, \tag{4.1}$$

where $I_{RHC,\,LHC}$ is the normalized current measured for RHCP and LHCP incident light respectively. We measured D at various angles of incidence for the chiral Ti nanostructures (Fig. 4.2a). Then we repeated the experiment with the same angles and same normalization procedure with two anisotropic Ti surfaces (Fig. 4.2b) and an isotropic Ti surface.

As can be seen in Fig. 4.4, the circular dichroism for the chiral structures is

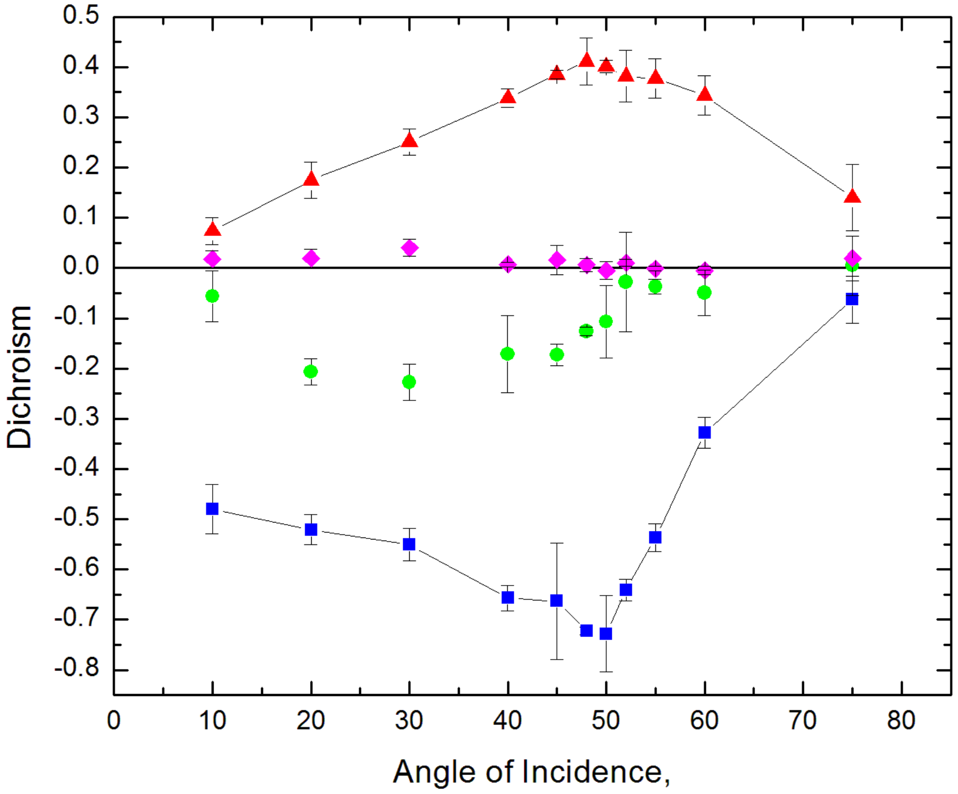

Figure 4.4. Reflection circular dichroism measurements for four samples at various angles of incidence. Purple diamonds correspond to data taken from the isotropic sample. Red triangles and green circles correspond to data from the anisotropic samples. Blue squares correspond to data taken from the chiral samples. Data was taken at Φ = 0. Lines are drawn to guide the eye.

much higher than for both anisotropic samples and the isotropic sample. As could be expected, the isotropic sample resulted in no circular dichroism. It was later found out that even though the anisotropic sample that is shown by the green circles was grown in the same way as the other anisotropic sample, the orientation of the rods was not properly documented, so we refrained from taking more data with that sample than is shown in Fig. 4.4. The direction that anisotropic sample 1 was angled in Φ was known, so we attempted to position the sample so that the ends of the rod were pointing downward, making the plane containing the rods and perpendicular to the substrate to be vertical when $\Phi = 0^0$ (Fig. 4.5a). It is unclear why the anisotropic sample has such a large dichroism. Since the planes of the rods were perpendicular to the plane of incidence/reflection, no large dichroism (or at least a mostly constant one) over the range of angles was expected. One possible explanation is that the rods may not be aligned as well in Φ as we thought, and that this misalignment is causing the changing dichroism. The Ti stair-step sample behaves similarly. Since they are grown in the same way as the anisotropic sample, the last layer of the stair-step spiral would also be at 50^0 and would behave similarly to the anisotropic samples, so seeing the same behavior at 50^0 is not unexpected, but the size of the effect and exactly why it's happening was unclear. Figs. 4.5b, c show this similarity between the anisotropic sample and the last layer of the chiral sample.

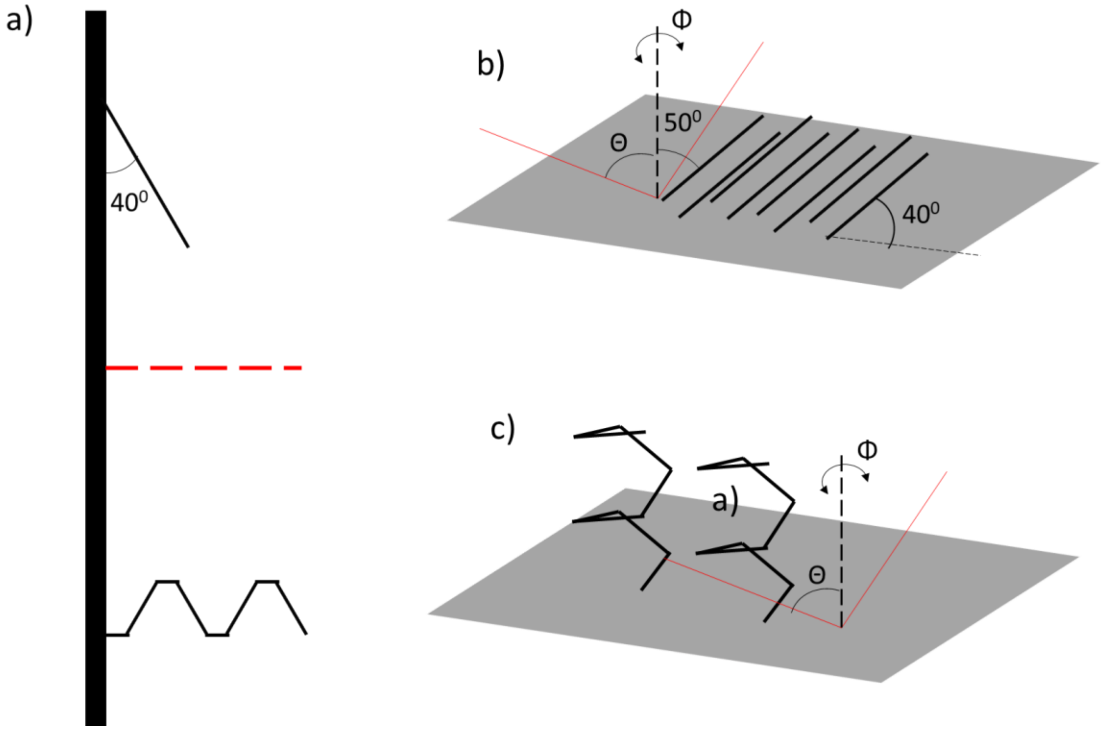

Figure 4.5. Simplified views of Ti anisotropic and chiral samples. This shows a) a side view of the two sample types as well as the plane of the laser (red dashed line) when the angle Φ = 0, as well as isometric views of b) the anisotropic sample and c) the chiral sample.

These results led us to investigate what happens when we keep the angle of incidence constant while we rotated the samples around an axis normal to the surface of the sample in 45^0 steps. It was thought that this experiment would be able to show us if the results were due to not having the sample at the azimuthal angle at which we thought it was. As can be seen (Fig. 4.6), the chiral sample appears to not only have twice the period of the anisotropic sample at larger angles of incidence, but it also reaches significantly higher values of dichroism. The most baffling of all is the anisotropic sample. We see in Fig. 4.6 that for small azimuthal angles at the 50^0 and 75^0 angles of incidence, the dichroism changed signs. We currently have no explanation for this sign change and we didn't see any indicators that would explain why it was happening. Further investigations are currently being done to find the underlying reasons for these differences as well as determining if these measurements would be able to be used on any sample to determine if the surface is chiral.

Despite the fact that we are unsure of the meaning of all the data at this time, there are several interesting features in Fig. 4.6. The first is that we see that at small angles of incidence, there is very little change of the dichroism for the chiral sample. This seems reasonable because when looking down on the spirals, you would see what appears to be an array of squares and it wouldn't change much as you rotate the sample about the normal. We also see that we get a

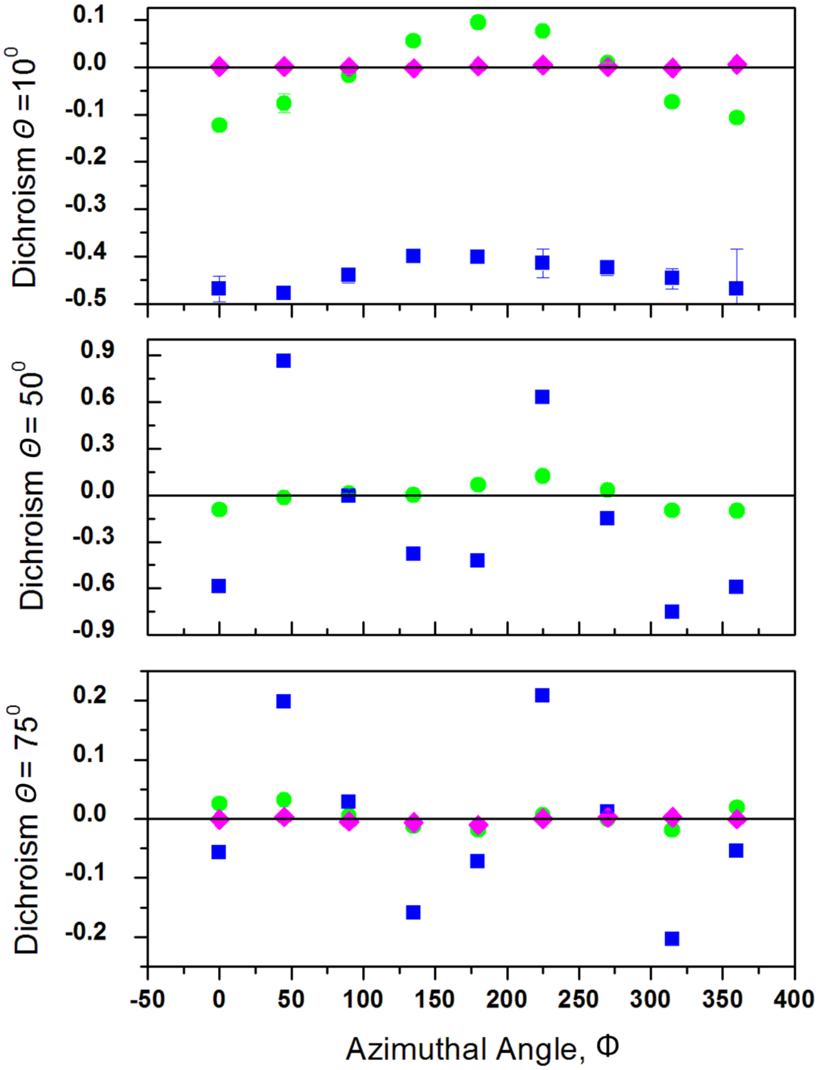

Figure 4.6. Circular dichroism measurements for three different angles of incidence, θ, while rotating the sample about the azimuthal angle, Φ, an axis normal to its surface. The data legend is the same as in Figure 4.4; Φ corresponds to the degree of rotation from the angle at which the ends of the rods are pointing downward.

maximum value of dichroism for the Ti samples at an angle of incidence of 50^0 and approximately at every 90^0 of azimuthal rotation starting at 45^0. This seems counter to what we thought and in the next round of measurements, great care will have to be taken to determine the direction of the samples so that we can for sure know the orientation of the last layer of the Ti stair-steps.

4.3. Emission Dichroism of Ti Chiral Structures

In parallel with the reflection measurements, we investigated if there was dichroism in the emission of electrons from these samples due to Ti: Sapphire oscillator pulses. We characterize the dichroism using the same equations (3.15 and 3.16) we used for the GaAs tips.

We started with the chiral Ti stair-step nanostructures on a silicon substrate. The first discovery was that we didn't obtain any measurable emission when we had the laser at normal incidence to the surface. Two possible explanations for this result are that at normal incidence, the laser was traveling deeper into the material and exciting electrons at a depth that allowed them to be recaptured before they were emitted from the material, or, after looking at later results, it is possible that the laser was RHCP when doing this preliminary emission test, and it was driving electrons further down the steps and not causing enough emission for us to measure. After rotating the sample so that the angle of incidence was 45^0, we obtained measurable emission from the sample. Using the polarization measurement setup described in Chapter 2 and seen in Figs. 2.1 and 2.2, we were able to switch between both directions of circular polarization and two directions of linear polarization where one was completely perpendicular to the axis of the chiral nanostructures while also being parallel to the surface of the substrate and the other was perpendicular to the first so that it had a component of its linear polarization along the axis of the nanostructures as shown in Fig. 4.7. Due to the angle of incidence we were at, we couldn't completely align the polarization with the axis of the nanostructures (this would only happen at 90^0 grazing incidence).

We can use eqn. 3.15 since we established earlier that the small difference in power between the two different linear polarizations doesn't affect the dichroism value. Table 4.1 shows the results of these measurements to be roughly consistent with the results from isotropic Ti and that both are approximately consistent with zero when we calculate the error in the same manner described in Chapter 3.

As was the case with the polarization measurements in Chapter 3 (seen in Fig. 3.16), the dichroism measurements also had a scatter that was larger than could be explained by statistical error. Even in areas where the error bars are small (i.e. small statistical uncertainty), the data is still spread out by more than can be described by purely statistical fluctuations. The cause for this additional

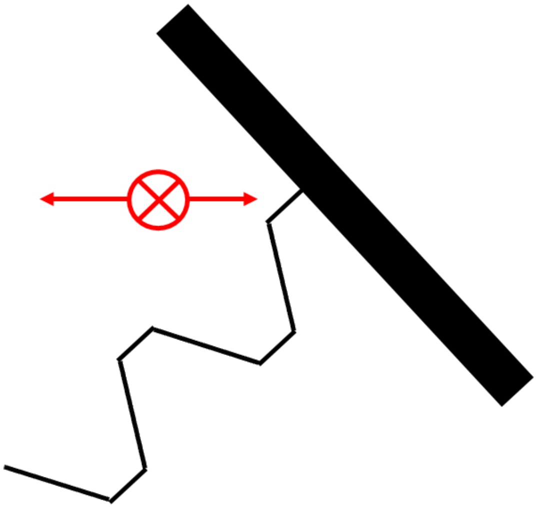

Figure 4.7. Side view of the Ti chiral structures. When taking emission data, the directions of the linear polarization are either perpendicular to the page or horizontal as indicated by the red lines. In this view, the laser will be coming from the bottom of the page when it hits the sample.

Chiral Ti 45^0 Incidence			
		Polarization (%)	Dichroism (%)
	Circular	2.8(2.7)	3.1(0.8)
	Linear	2.7(2.3)	8.4(1.2)
Ti Isotropic substrate 45^0 Incidence			
		Polarization (%)	Dichroism (%)
	Circular	2.0(1.0)	5.3(2.9)
	Linear	1.3(1.1)	13.9(4.8)

Table 4.1. Electron polarization and total emission dichroism for both circularly- and linearly-polarized incident light for chiral Ti nanostructures and an isotropic Ti substrate.

uncertainty is not known, but it is possible that we are getting small movements of the sample which makes the laser hit slightly different positions over time or there are small oscillations in laser power that we aren’t able to measure. It should also be noted that the isotropic Ti could not emit a measurable number of electrons when the laser was focused on the bulk and we ended up taking the data from a sharper area at the edge. This could skew the linear dichroism data for the isotropic material as we may be getting some field emission effects.

For circularly polarized light, we calculate $D \approx 3\%$. This means that the number of emitted electrons appears to not be affected significantly by the direction of circular polarization of the light. However, if we look back to Fig. 4.4, we see that there is a large reflection dichroism for circularly polarized light. While keeping in mind that the reflection data were taken at a different wavelength, this means that the handedness of light that has a higher reflection coefficient is actually able to emit the same number of electrons at a lower intensity since less light is being absorbed by the Ti for that handedness. It is unclear if the fact that the emission dichroism is essentially zero is material dependent or if this would be the case for any material that exhibits the same reflectivity dichroism. Future investigations could attempt to compare these results to see if it is material dependent or if there is some unknown process occurring. The Ti samples are right-handed stair-steps, and the zero value for circular emission dichroism shows that the LHCP light emits the same number of electrons as does the RHCP. This seems to imply that the RHCP drives electrons down the structure causing a smaller percentage of the total electrons to be emitted whereas the LHCP drives them up and out of the structure giving approximately equal amounts of emitted electrons for both directions of circularly-polarized light.

When using linearly polarized light, we measured a linear dichroism of about 8%. As we didn’t investigate the effect on the reflectivity with linearly polarized light, we are unable to compare emission linear dichroism with reflection linear dichroism, but it is worth noting that this value shows us that we emit more electrons when the linear polarization has a component along the axis of the chiral structures (the horizontal polarization in Fig. 4.7) than when the linear polarization is completely perpendicular to that axis (perpendicular to Fig. 4.7). A future investigation could include systematically measuring the linear dichroism at different angles of the sample rotation since the amount of the component parallel to the structures’ axis would change. The difficulty of this is that as you rotate the sample, the relative position of the sample and the laser focus could change which could also cause significant change in the emission rates for the two polarizations.

4.4 Emission from Pd Chiral Nanostructures

Since it has been shown that spin-orbit effects in scattering experiments are proportional to Z^2 (56), we wanted to check if using a higher-Z atom for the material that the nanostructures are made from would possibly give us a larger dichroic effect and possibly have a higher polarization of emitted electrons. Since Ti has Z = 22, we chose the new material to be palladium (Pd) which has Z = 46. The work functions are W = 4.33 eV for Ti and W = 5.22 - 5.60 eV for Pd (57). This means that the work function of Pd corresponds to the energy of an extra photon from our laser as compared to Ti. We had originally wanted to use gold as the material since it has a much higher Z, but when Prof. Schubert's group attempted to create gold nanostructures it tended to form into balls instead of helical coils.

The Pd samples were made using the same procedure as the Ti samples, but the Pd took much longer to deposit. For this reason, the Pd helices had only one full rotation whereas the Ti samples had had four full rotations. We also decided to have these samples made by continuous rotation of the substrate so that the structures were more of a continuous corkscrew shape instead of the cornered stair-step shape of the Ti. Since the Pd deposited so slowly, it ended up being much easier to have it continuously rotate than to do the 90^0 sequential rotations. This means a follow-up experiment could compare the emission characteristics of the same material made in the corkscrew shape against the stair-step shape.

Unexpectedly, when using the Pd samples, we were able to get measurable emission when the laser was at normal incidence. As a result, we took data at both 0^0 and 45^0 to compare the different angles with the same material and to compare the results at 45^0 angles for two different materials.

As can be seen in Table 4.2, no significant electron polarization was measured using either circularly or linearly polarized light. The dichroism data showed some interesting results, however. For the circularly polarized light, we see a non-zero dichroism except for 0^0 incidence on the isotropic sample. In the Ti sample, we saw that even though one handedness of circularly polarized light was reflected more, the circular emission dichroism was approximately zero, with the caveat that the two were taken at different wavelengths. From the results of the Pd emission data, we believe we are seeing the same effect except that since Pd has a higher work function, the emission dichroism effect is no longer zero, so the difference in intensities due to the preferential reflection of LHCP is not compensated by the increased emission for LHCP. There was also a linear dichroism in the emission. Since the linear dichroism was larger when the sample was at 0^0, we believe that this may be due to the orientation of the top of the chiral structure. It appears that the sample emits more if the end of the chiral structure points along the same direction as the linear polarization, but that parameter was not carefully checked, so a more systematic study would need to be developed to see if this is truly the case.

Again, we did the same measurements on an isotropic thin film sample of Pd for comparison with a non-chiral sample. The polarization values are all zero as we had expected except for the chiral structures at 0^0 incidence. It may be that the error bars are not large enough, but there could also be some real polarization. Similarly to the isotropic Ti sample, we were unable to get measurable emission unless we are on a sharper feature and thus we can't separate any linear dichroism

Pd 45^0 Incidence		Polarization (%)	Dichroism (%)
	Circular	0.9(2.2)	21.1(0.5)
	Linear	0.3(0.1)	12.6(0.7)
Pd 0^0 Incidence		Polarization (%)	Dichroism (%)
	Circular	3.3(1.0)	34.4(2.3)
	Linear	1.8(1.3)	45.6(5.1)
Pd Isotropic 0^0 Incidence			
		Polarization (%)	Dichroism (%)
	Circular	0.5(2.5)	2.3(11.5)
	Linear	1.6(3.9)	29.7(5.1)
Pd Isotropic 45^0 Incidence			
		Polarization (%)	Dichroism (%)
	Circular	1.9(2.3)	6.2(5.1)
	Linear	2.2(4.3)	40.8(5.9)

Table 4.2. Results for Pd chiral structures and isotropic Pd for 0^0 and 45^0.

effects from an FET-like effect. The numbers are only included in the table for the sake of completeness. The circular dichroism is also expected to be zero. While the error bars are not encompassing zero, it seems that this may merely be a problem with slightly underestimating the uncertainty still. This seems to be more the result of not including an instrumental uncertainty more so than any actual effect that we saw.

4.5 Chiral Structure Damage

One concern we had was that the laser was causing the chiral structures to melt or sublimate, removing them from the substrate. For this reason, we checked the chiral Pd sample with an SEM after taking data to see if there was any damage that we could see to the structures. Fig. 4.8 shows the area where the laser was incident after we finished taking data. The laser had been on the indicated area for approximately 30 hours, which was the area that had the longest exposure to the laser. We thus believe that at our intensities, there is no danger of destroying or physically altering the nanostructures due to the laser. Using our focused beam spot size along with the parameters of our laser pulse, we calculate the average intensity of our laser to be 32 kW/cm^2 with peak intensities of 4 GW/cm^2. The damaged areas on the left side of Fig. 4.8 (the dark, flat areas) are very near the edge of the crystal and were most likely damaged during the cleaving process. Since the process for cutting the samples was to press a razor blade onto the face of the sample until breakage occurred along the lattice lines, there was the potential for damage to the structures near this fracture. It was for this reason that we never took data near the edge of the chiral samples.

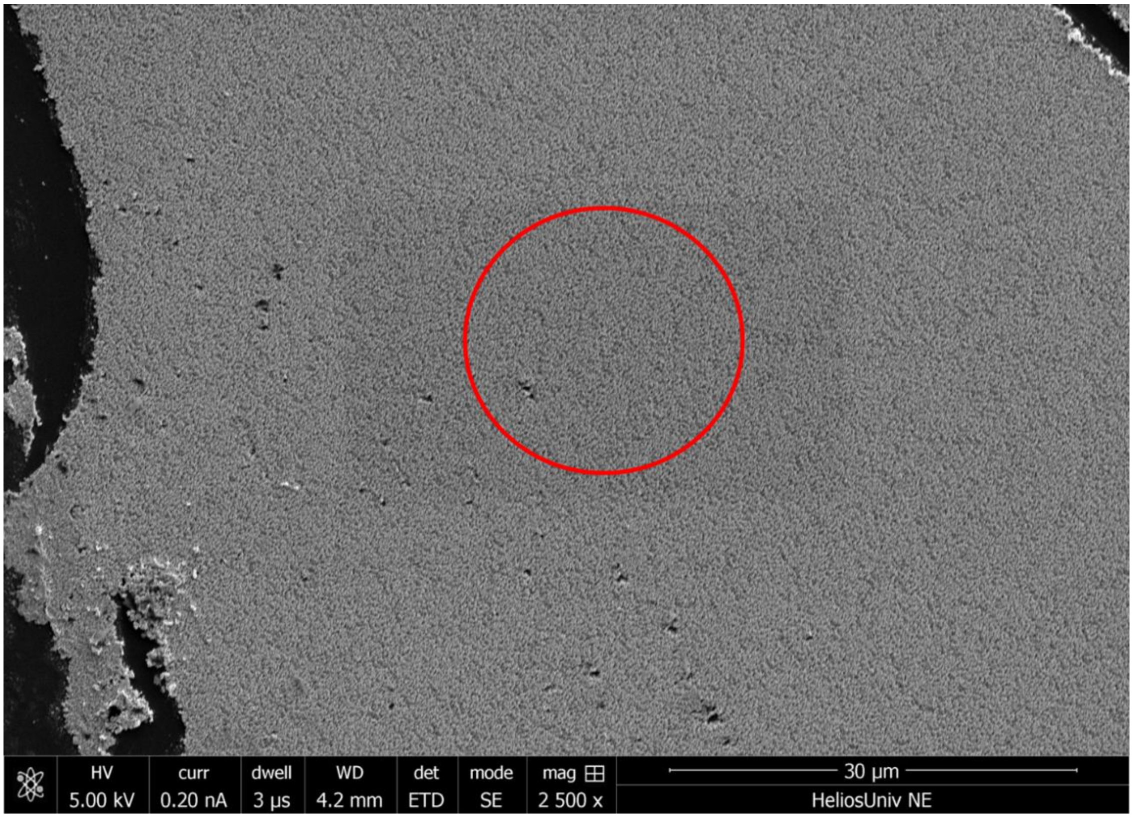

Figure 4.8. SEM image of Pd chiral structures after laser-induced photoemission data were taken. Data acquisition times were regularly > 24 hours in the general area indicated by the red circle. No damage is evident in the region where the laser was incident on the sample.

Chapter 5 GaAs Wedge

5.1 Introduction

The final sample investigated for this dissertation was prepared by electro-etching a shard of GaAs. The process of creating this sample was developed by the Flanders group at Kansas State University and was inspired by the process used to create pyramidal structures on GaAs (58). The setup to create these samples can be seen in Fig. 5.1. An aqueous solution of $10H_3PO_4 + H_2O_2 + H_2O$ and a stir bar were put in a beaker. A shard of freshly cleaved GaAs was mounted to a conducting cantilever and lowered into the solution to serve as the working electrode. A segment of 0.9 mm diameter pencil lead served as the counter electrode. After turning on a stirrer, electro-etching was initiated by biasing the working electrode to +13.0 V and grounding the counter-electrode using a DC power supply. The etching process is most vigorous at the air-solution interface. The sample was etched for 7 minutes, then removed and rinsed with de-ionized water. This process was repeated approximately three more times until the submerged fraction of the shard separated from the upper portion and sank. The upper portion was immediately removed and rinsed (59). The sample we used is shown in Fig. 5.2. As can be seen, the etching procedure causes there to be much less jaggedness as compared to the cut GaAs in Fig 3.17.

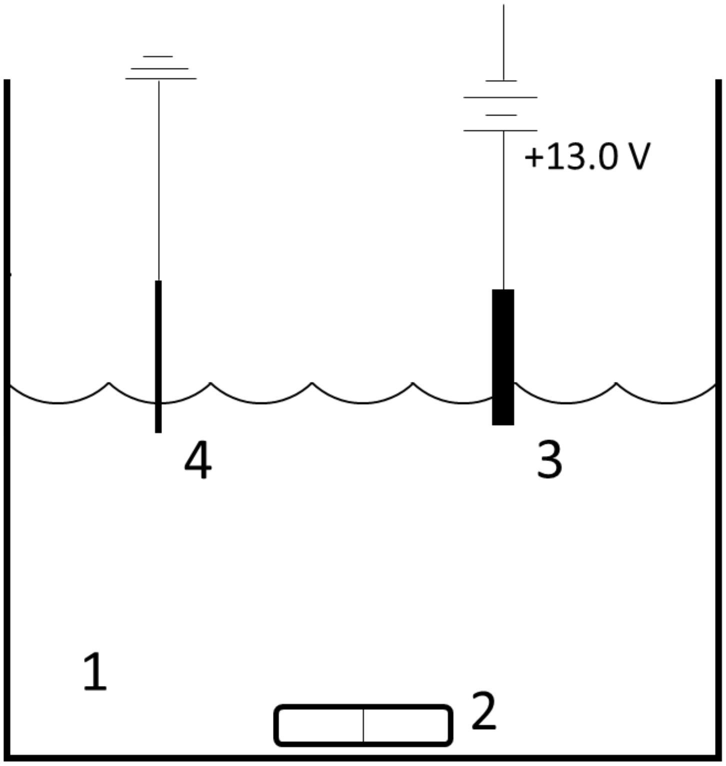

Figure 5.1. The setup for creating a thinned wedge of GaAs (59). A solution as described in the text (1) with a magnetically-coupled stir bar (2) is placed in a beaker. A freshly cleaved piece of GaAs (3) is partially submerged in the solution with a positive bias while a piece of pencil lead (4) serves as the grounded counter electrode.

Figure 5.2. SEM image of the area investigated on a GaAs wedge sample that has been chemically etched using the procedure described in the text. The laser spot size is approximately 20 μm.

5.2 Results

Using the same electron polarimetry procedure we described for the other samples, we calculated the polarization for electrons emitted from the area indicated in Fig. 5.2. The results can be seen in Table 5.1 and they show that we measured zero polarization for linearly-polarized light and nearly zero dichroism when using circularly-polarized light. Even the linear dichroism measurement was nearly zero. The polarization when using circularly-polarized light appears to be non-zero but is lower than any previous measurements using GaAs. This wasn't what we had expected, but further analysis leads us to believe that this is consistent with our previous GaAs measurements.

When looking at the emission in general, the thinned GaAs wedge had similar emission currents as that of the GaAs shard described in Chapter 3. The currents tended to be on the order of nanoamps with a maximum observed value of 5 nA, so it doesn't appear that thinning the sample increases our emission significantly.

GaAs Wedge		Polarization (%)	Dichroism (%)
	Circular	7.4(2.8)	1.1(2.4)
	Linear	6.9(5.6)	3.1(1.9)

Table 5.1. Polarization and dichroism measurements for electrons emitted from a thinned GaAs wedge.

The earlier bulk GaAs measurements were taken from samples that were cut using a razor blade and thus had jagged areas where the crystal broke along the crystalline axes. We saw a difference in polarization that seems to depend upon how sharp or jagged the sample is because the polarization was less for a sample that was smoother. The GaAs wedge seems to follow the same trend because the wedge is much smoother due to the chemical etching and thus has a lower polarization. We think there are two possibilities for this dependence of the polarization on the sharpness of the tip. The first is that due to the sharpness of the tip, the band structure could be changed from that of the bulk and therefore causes differences in emission probabilities from what is expected in bulk GaAs. The second is that when the tip is sharp, we get more emission from the tip, but when the tip is less sharp, more electrons (as a fraction of the total number of emitted electrons) come from farther away from the tip and thus have more collisions with atoms before being emitted, giving the electrons a higher probability of becoming depolarized.

5.3 Next Steps

Since it appears that the polarization depends upon the sharpness of the sample, a next experiment should be to measure the polarization that is emitted from a sample of the thinned GaAs wedge that has been ion milled to have a small, sharp tip. Fig 5.3 shows a sample that has been prepared using ion milling.

If our prediction is correct, this has the potential to have even higher polarizations than our previous measurements with comparable emission currents.

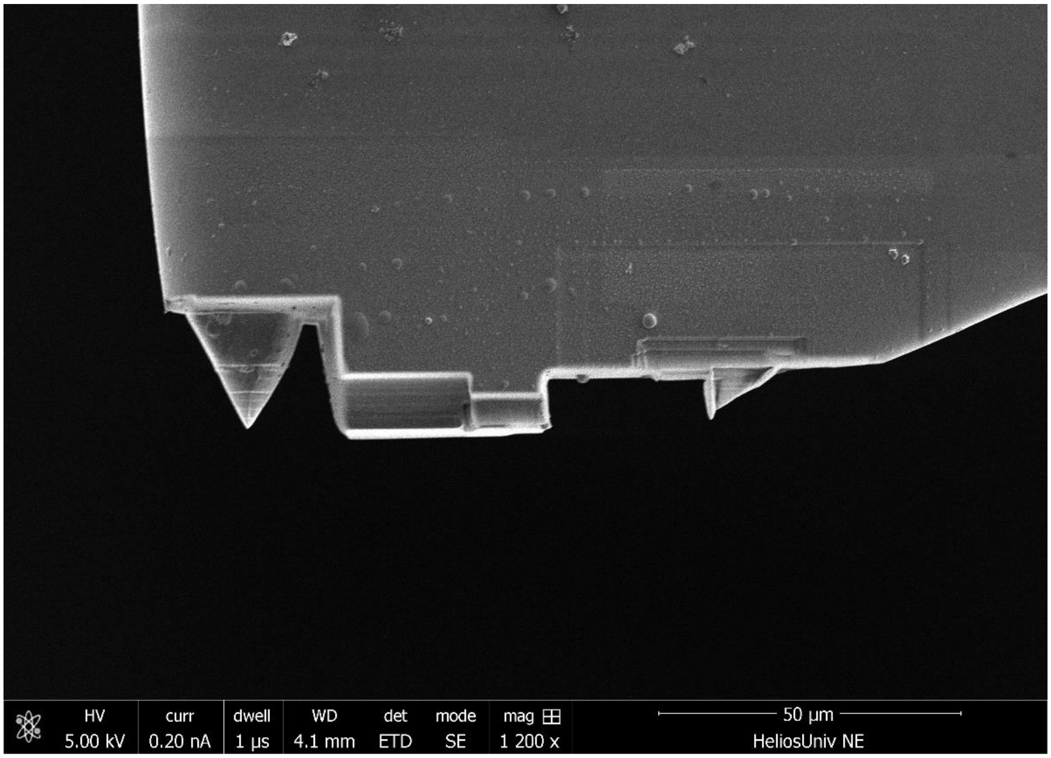

Figure 5.3. A thinned GaAs wedge that has been ion milled to have two sharp points with radii of curvature of approximately 100 nm and 150 nm for the left and right points respectively. Sample prepared by Sam Keramati of the Batelaan group in UNL's Department of Physics and Astronomy.

Chapter 6 Chiral Surface on Silicon

6.1 Introduction

Our work with chiral nanostructures on a substrate led us naturally to be interested in the possibilities of photoemission from a fundamentally chiral surface environment. A long-time colleague of Prof. Gay's, Dr. Elaine Seddon of the Cockroft Institute in Great Britain and her group, had recently started investigating photoemission from a chiral surface reconstruction on Si (60). As it complimented our research with chiral structures, they extended an offer to collaborate with them. These tests were run at the Elettra Sincrotrone Trieste facility outside of Trieste, Italy. All measurements were done on the Advanced Photoelectric Effect- Low Energy (APE-LE) beam line at Elettra (61). Fig. 6.1 shows the entire apparatus for the APE line, the low-energy section consists of the left half of the apparatus when looking at the top view. The main chamber of the low-energy apparatus had the ability to do spin- and angular-resolved photoemission spectroscopy (SARPES) as well as low energy electron diffraction (LEED).

It has been found that for a clean (110) sample of a IV group semiconductor, the most stable form for a diamond structure consists of zig-zag protrusions caused by the surface atoms aligning in equally spaced and alternately raised and lowered stripes (62). This has been seen in Ge (63) and SiGe/Si (64) in

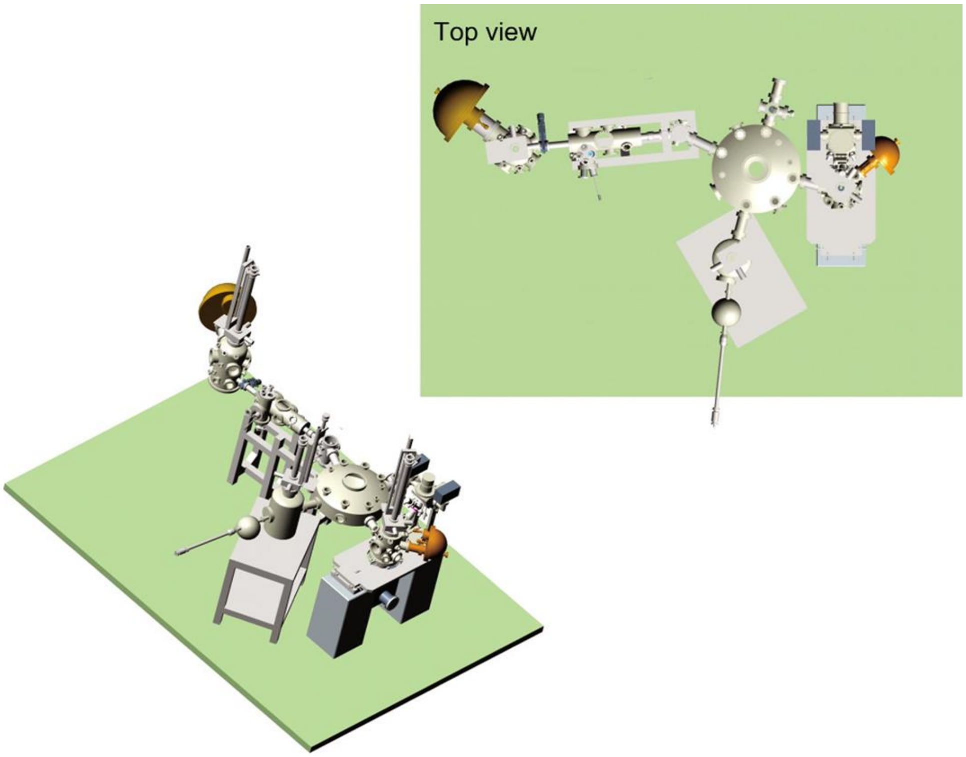

Figure 6.1. Entire APE apparatus. The low energy area consists of all the components to the left of the largest circular chamber in the center of the top view. In the top view, a load-lock is located on the right side of the low-energy section with the long horizontal section to the left being a transport section to move the sample from the load-lock to the emission chamber. The emission chamber is the smaller cylindrical chamber near the left side. The hemispherical chamber on the far left is the SARPES analyzer. The beamline comes down vertically directly into the emission chamber. Reprinted from G. Panaccione et al., Rev. Sci. Instrum. **80**, 043105, with the permission of AIP Publishing.

addition to Si (62). This formation is referred to as the 16 x 2 surface, referring to the dimensions of the unit cell of which the surface is comprised.

For Si, these raised and lowered strips are comprised of Si atoms arranged in pairs of pentagons as seen in Fig. 6.2. These pairs of pentagons can form two different formations: left- or right-handed. The two versions are two-dimensionally chiral which means that they are mirror images of each other through a plane perpendicular to the surface and cannot be superimposed by any combination of translation and rotation in the surface plane.

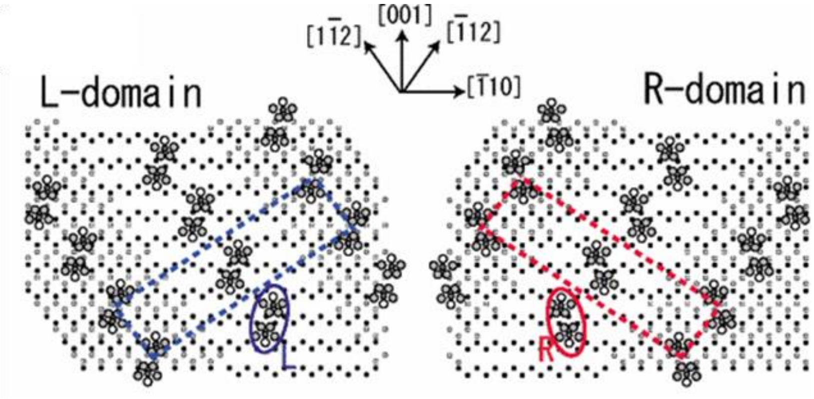

Figure 6.2. The 16 x 2 surface reconstruction for Si in both the left- and right-handed domains. The blue- and red-dashed boxes show the unit cells while the blue and red ovals show the pairs of pentagons that form the strips. Reprinted figure with permission from Y. Yamada, A. Girard, H. Asaoka, H. Yamamoto, and S. Shamoto, Phys. Rev. B **77**, 153305, 2008. Copyright 2008 by the American Physical Society.

In general, both the left- and right-handed domains are present on a 16 x 2 reconstructed surface as in Fig. 6.3, but a procedure has been found to reproducibly form the surface into a single domain (65).

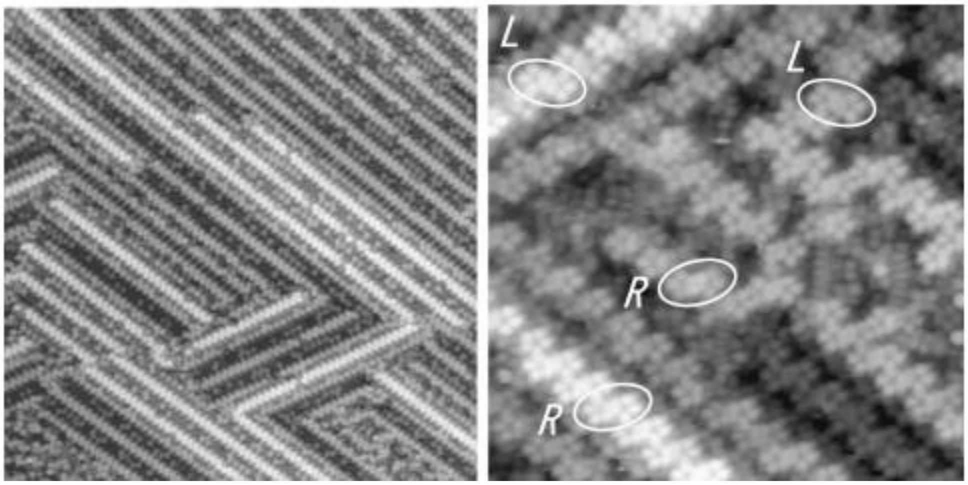

Figure 6.3. STM image of a double domain. Both images show the same double domain surface containing both the left- and right- handed domains. The image on the left shows a 90 nm x 90 nm section whereas the right image shows a 17 nm x 17 nm section. Ovals in the right image indicate the L and R pairs of pentagons for the left- and right- handed domains respectively. Reprinted figure with permission from T. An, M. Yoshimura, I. Ono, and K. Ueda, Phys. Rev. B **61**, 3006, 2000. Copyright 2000 by the American Physical Society.

The samples were made from phosphorus-doped silicon wafers (resistivity of 4-6 Ωcm) made by PI-KEM Ltd. with the surface along (110) with both sides of the sample polished. The wafers were cut into small rectangles with dimensions 12 x 2 x 0.25 mm with the short side along either the $[\bar{1}12]$ or $[1\bar{1}2]$ directions. To create the 16 x 2 surface reconstruction, the samples were resistively heated. The pressure in the chamber was required to be less than 10^{-9} mbar, so the sample needed to be degassed for several hours at a temperature of ~700^{0}C. We could observe the temperature using a pyrometer aimed through a chamber window at the center of the sample in the chamber. After the pressure was low enough while the sample was at temperature, a series of flashings were needed in order to remove surface contaminants such as oxygen and carbon. This involved quickly ramping up the current until the sample reached a temperature of 1200^{0}C and leaving it there for one to two seconds and then lowering the current quickly, so the sample returned to the 700^{0}C range. We would then wait until the pressure fell below 10^{-9} mbar and repeated the flashing until there was little-to-no change in the pressure from one flashing to the next. This usually took about six flashes.

We then left the sample at 715^{0}C to anneal for 15 minutes. After annealing, the current was lowered at a rate of 50 mA/min to obtain the correct surface reconstruction (65) (66). If the current is immediately turned off, the surface will remain in the bulk (1 x 1) state (65) as this is the temperature for the phase transition between the 1 x 1 and the 16 x 2 states. Similarly, if the current is lowered at a slower rate, but still fairly quickly, the surface will be in the double domain state as the adjacent areas cool too quickly to match each other's domains. It is thus crucial not to take the current down too quickly.

When successful, the surface of the sample will be completely in the “16 x 2” formation as seen in Fig. 6.4. The channels can be seen, and the zig-zag shape of the pentagonal structures are evident although it is somewhat difficult to make out the pentagonal shape as at this resolution, they appear more like bright circles.

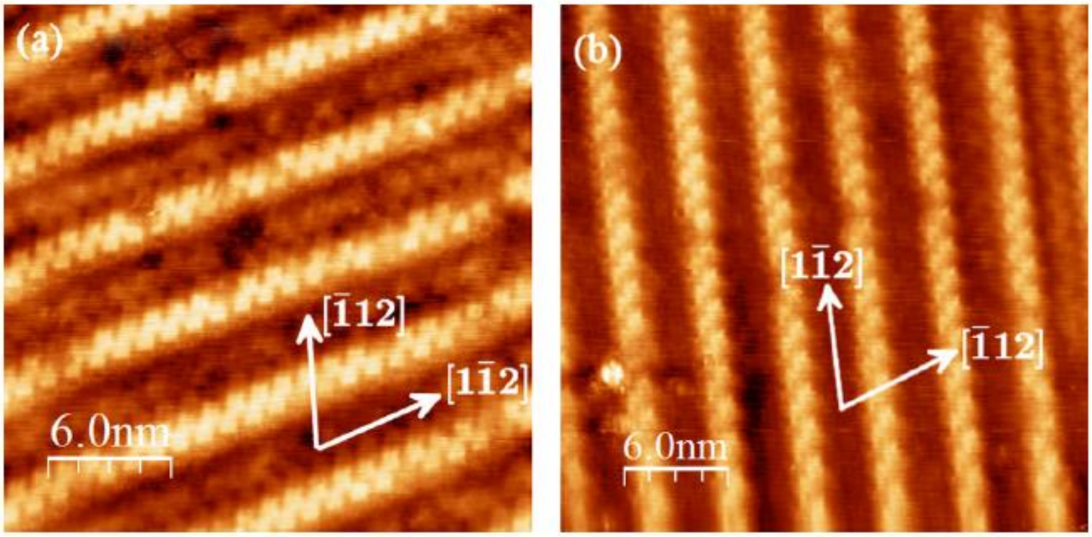

Figure 6.4. STM images of two different samples showing the Si(110) “16 x 2” reconstruction. Both samples show channels in the $[1\bar{1}2]$ direction. Image from (60).

Taking polarization measurements of photoemitted electrons from the 16 x 2 Si was the primary goal of this experiment, but a secondary one was to measure the polarization of the emitted electrons if gold was deposited on the surface. As stated earlier in this work, the spin-orbit effects increase as the Z of the scattering material increases, so we wanted to investigate if putting Au on the surface would enhance any photoemitted electron polarization effect we saw. Since we still wanted the Si to be the dominant feature of the surface, we deposited approximately 0.3 monolayers of Au, so the surface was not completely covered.

6.2 Si Results

In a first experiment at Trieste in May 2016, we obtained data for the 16 x 2 Si that appeared to show a somewhat large (~10%) polarization. It was discovered toward the end of the run that the polarimeters were not calibrated sufficiently to measure polarizations on that scale. Most work on that beamline dealt with polarizations on the order of 80% or more, so until our work, a 10% offset wasn't considered to be a concern for the beamline. We attempted to take some calibration data at the end of the run, but there wasn't time to make enough measurements to be able to definitively say whether or not there was any polarization of the emitted electrons.

We then went back to the facility in September 2017 and attempted to make the measurements again. The polarimeters had been checked and calibrated to be able to measure polarizations as low as 5%. The data we took was consistent with zero, so the best we are able to say is that if there is an effect on the polarization of the electrons by the surface chirality, it causes less than 5% polarization, as that is the error of the polarimeter.

Again, we saw no noticeable change in the measurements when gold was added. One possibility is that because the gold was physisorbed (physically sitting on the surface of the Si with no appreciable chemical bonding present), it wouldn't have an effect. It is possible if it is chemisorbed, i.e., if some of the Si atoms are replaced with gold, that there might be a measurable result. As of now, we have no easy way of chemisorbing the gold, so future setups would need to figure out a way to reliably and reproducibly do this.

References

[1] J. Kessler, Polarized Electrons, 2nd ed., (Springer, Berlin, 1985).

[2] G. D. Fletcher, M. J. Alguard, T. J. Gay, V. W. Huges, P.F. Wainwright, M. S. Lubell, and W. Raith, Phys. Rev. A 31, 2854 (1985).

[3] T.J. Gay, Adv. At. Mol. Phys. **57**, 157 (2009).

[4] See, e.g., C. Y. Prescott et al., Phys. Lett. B **77**, 347 (1978).

[5] See, e.g., D. Androic et al., Phys. Rev. Lett. **111**, 141803 (2013) and references therein.

[6] See, e.g., Polarized Electrons in Surface Physics, edited by R. Feder (World Scientific, Singapore, 1985).

[7] See, e.g., K. von Bergmann, M. Bode, A. Kubetzka, M. Heide, S. Blügel, and R. Wiesendanger, Phys. Rev. Lett. **92**, 046801 (2014).

[8] See, e.g., F. Giebels, H. Gollisch, and R. Feder, Phys. Rev. B **87**, 035124 (2013).

[9] D. T. Pierce, F. Meier, Phys. Rev. B **13**, 5484 (1976).

[10] D. T. Pierce, R. J. Celotta, G.-C. Wang, W. N. Unertl, A. Galejs, C. E. Kuyatt, S. R. Mielczarek, Rev. Sci. Instrum. **51**, 478 (1980).

[11] C. T. Foxon, J. A. Harvey, and B. A. Joyce, J. Phys. Chem. Solids 34, 1693 (1973).

[12] B. Goldstein, D. J. Szostak, and V. S. Ban, Surf. Sci. 57, 733 (1976).

[13] N.B. Clayburn, K.W. Trantham, M. Dunn, T.J.Gay, Rev. Sci. Instrm. **87**, 124903 (2016).

[14] R. Alley *et al.*, Nucl. Instrum. And Meth. A **365**, 1 (1995).

[15] F.-C. Tang, X. Zhang, F.B. Dunning, and G.K. Walters, Rev. Sci. Instrum. **59**, 504 (1988).

[16] P. Hommelhoff, Y. Sortais, A. Aghajani-Talesh, and M. A. Kasevich, Phys. Rev. Lett. **96**, 077401 (2006).

[17] B. Barwick, C. Corder, J. Strohaber, N. Chandler-Smith, C. Uiterwaal, and H. Batelaan, New J. Phys. **9**, 142 (2007).

[18] Griffin 5 Ti: Sapphire laser, KMLabs.

[19] Sprout 12G, Lighthouse Photonics.

[20] Photon Control Spectrometer-SPM-002, Photon Control.

[21] BB1-EO3 Dielectric Mirror, ThorLabs.

[22] Position Sensitive Detector, On-Trak Photonics Inc., OT-301.

[23] GRENOUILLE Model 8-20, Swamp Optics.

[24] SIMION 8.1, Scientific Instrument Services Inc.

[25] N.B. Clayburn, E. Brunkow, S.J. Burtwistle, G.H. Rutherford, T.J. Gay, Rev. Sci. Instrum. **87**, 053302 (2016).

[26] T.J. Gay and F.B. Dunning, Rev. Sci. Instrum. **63**, 1635 (1992).

[27] See, e.g., T.J. Gay, M.A. Khakoo, J.A. Brand, J.E. Furst, W.V. Meyer, W.M.K.P. Wijayaratna, and F.B. Dunning, Rev. Sci. Instrum. **62**, 114 (1992).

[28] L. A. Hodge, F. B. Dunning, and G. K. Walters, Rev. Sci. Instrum. **50**, 1 (1979).

[29] J. L. McCarter, M.L. Stutzman, K.W.Trantham, T.G.Anderson, A.M.Cook, and T.J.Gay. Nucl. Instrum. Meth. A **618**, 30 (2010).

[30] D.D. Neufeld, H. Aliabadi, and F.B. Dunning, Rev. Sci. Instrum. **78**, 025107 (2007).

[31] F.B. Dunning, L.G. Gray, J.M. Ratliff, F.-C. Tang, X. Zhang, and G.K. Walters, Rev. Sci. Instrum. **58**, 1706 (1987).

[32] Model 463, Detector Technology, Inc.

[33] G.C. Burnett, T.J. Monroe, and F.B. Dunning, Rev. Sci. Instrum. **65**, 1893 (1994).

[34] D.P. Pappas, and H. Hopster, Rev. Sci. Instrum. **60**, 3068 (1989).

[35] D.J. Huang, W.P. Wu, J. Chen, C.F. Chang, S.C. Chung, M. Yuri, H.-J. Lin, P.D. Johnson, and C.T. Chen, Rev. Sci. Instrum. **73**, 3778 (2002).

[36] S. Qiao, A. Kimura, A. Harasawa, M. Sawada, J.-G. Chung, and A. Kakizaki, Rev. Sci. Instrum. **68**, 4390 (1997).

[37] V.N. Petrov, M.S. Galaktionov, and A.S. Kamochkin, Rev. Sci. Instrum. **72**, 3728 (2001).

[38] F. Ciccacci, S. De Rossi, and D.M. Campbell, Rev. Sci. Instrum. **66**, 4161 (1995).

[39] U. Fano and J. H. Macek, Rev. Mod. Phys. **45**, 553 (1973).

[40] S. Chin & P. Lambropoulos, Multiphoton Ionization of Atoms, Academic Press, 1984.

[41] J.F. Geisz & D.J. Friedman, Semicond. Sci. Technol. **17** No 8, 769 (2002).

[42] W. Pfeiffer, F. Sattler, S. Vogler, G. Gerber, J.-Y. Grand, R. Möller, Appl. Phys. B **64**, 265 (1997).

[43] Y. Terada, S. Yoshida, O. Takeuchi, H. Shigekawa, J. Phys.: Condens. Matter **22**, 264008 (2010).

[44] J. R. Goldman, J. A. Prybyla, Semicond. Sci. Technol. **9**, 694 (1994).

[45] Tsunami, Spectra-Physics Lasers Inc.

[46] H. C. Casey Jr., F. Stern, J. Appl. Phys. **47**, 631 (1976).

[47] J. Shah, R. F. Leheny, W. Wiegmann, Phys. Rev. B., **16**, 1577 (1977).

[48] G.C. Cho, W. Kütt, H. Kurz, Phys. Rev. Lett., **65**, 764 (1990).

[49] P.R. Bevington, Data Reduction and Error Analysis for the Physical Sciences, McGraw-Hill Book Company, 1969.

[50] C.W. Leemann, D.R. Douglas, and G.A. Krafft, Annu. Rev. Nucl. Part. Sci. 2001, **51**, 413 (2001).

[51] N.B. Clayburn, Ph.D. thesis, University of Nebraska- Lincoln, 2017.

[52] K. Robbie, M.J. Brett, and A. Lakhtakia, J. Vac. Sci. Technol. **13**, 2991 (1995).

[53] E. Schubert, T. Höche, F. Frost, B. Rauschenbach, Appl. Phys. A **81**, 481 (2005).

[54] E. Schubert *et al.*, Adv. in Solid State Phys. **46**, 309 (2008).

[55] HeNe laser, Research Electro-Optics Inc.

[56] N.F. Mott and H.S.W. Massey, The Theory of Atomic Collisions Third Edition Volume 1, p. 235, Oxford Science Publications, 1965.

[57] H.B. Michaelson, J. Appl. Phys. **48**, 4729 (1977).

[58] M. Kuwahara *et al.*, Jpn. J. Appl. Phys. **45**, 6245 (2006).

[59] B. Flanders, Kansas State University, private communication (2018).

[60] N.K. Lewis, N.B. Clayburn, E. Brunkow, T.J. Gay, Y. Lassailly, J. Fujii, I. Vobornik, W.R. Flavell, and E.A. Seddon, Phys. Rev. B **95**, 205306 (2017).

[61] G. Panaccione *et al.*, Rev. Sci. Instrum. **80**, 043105 (2009).

[62] T. An, M. Yoshimura, I. Ono, and K. Ueda, Phys. Rev. B **61**, 3006 (2000).

[63] Y. Ishikawa, Y. Hosokawa, I. Hamaguchi, T. Ichinokawa, Surf. Sci. Lett. **187**, L606 (1987).

[64] R. Butz and H. Lüth, Surf. Sci. **365**, 807 (1996).

[65] Y. Yamada, A. Girard, H. Asaoka, H. Yamamoto, and S. Shamoto, Phys. Rev. B **77**, 153305, 2008.

[66] K. Sakamoto, M. Setvin., K. Mawatari, P.E.J. Eriksson, K. Miki, and R.I.G. Uhrberg, Phys. Rev. B **79**, 045304 (2009).